Dissertation
submitted to the
Combined Faculties for the Natural Sciences and for Mathematics
of the Ruperto-Carola University of Heidelberg, Germany
for the degree of
Doctor of Natural Sciences

Put forward by

Dipl.-Phys. **Tobias Sebastian Schwarz**
Born in: **Heidelberg**

Oral examination: 01. Feb. 2011

COUPLED SHAPE MODELS FOR THE DIAGNOSIS OF ORGAN MOTION RESTRICTION

Referees: **Prof. Dr. Bernd Jähne**
Prof. Dr. Hans-Peter Meinzer

Zusammenfassung

Annähernd 30% der weltweiten Todesfälle sind auf Erkrankungen des Herzens und der Lunge zurückzuführen, wobei die meisten dieser Erkrankungen während ihres Verlaufs die Mobilität des betroffenen Organs verändern. Viele dieser Todesfälle könnten durch eine frühzeitige Erkennung und Behandlung der Erkrankung vermieden werden. Deshalb wurden im Zuge dieser Arbeit Methoden entwickelt, um aus Segmentierungen von dynamischen Magnetresonanztomographie-Daten quantitative Kennzahlen für die funktionale Analyse der Herz- und Lungenbewegung zu generieren. Ein automatisiertes Segmentierungsverfahren basierend auf gekoppelten Formmodellen wurde entwickelt, welches wechselseitige Informationen der Form und Geometrie mehrerer korrelierter Objekte mit einbezieht, und somit 40% bessere Ergebnisse im Vergleich zur Verwendung einzelner Modelle erzielte. Im Fall des Herzens wurde ein Volumenberechnungsfehler von unter 13% erreicht, was in der Größenordnung der Interobserver-Variabilität liegt. Für die Lunge konnte ein Volumenfehler von unter 70ml gezeigt werden. Aus den Segmentierungsergebnissen wurden funktionale Parameter der lokalen Organdynamik abgeleitet und visualisiert, die gegen konventionelle Diagnosemethoden evaluiert wurden und dabei gute Übereinstimmung zeigen, darüber hinaus jedoch eine lokal und regionale Mobilitätscharakterisierung erlauben.

Abstract

Approximately 30% of deaths worldwide originate from diseases of the heart and lungs, whereby most of which alter mobility of the organ during their course. Many of these deaths could be avoided by early detection and treatment of the disease. Therefore, in this thesis, methods have been developed for the analysis of dynamic magnetic resonance imaging data, and the generation of quantitative measures for the functional cardiac and pulmonary analysis from segmentation of these image sequences. An automated coupled shape model segmentation scheme has been developed that incorporates mutual information on shape and geometry of correlated objects to cope with the difficulties found in the image data, showing 40% better results compared to single models. For the heart, a volumetric error of below 13% was achieved, which is in the magnitude of inter-observer variability. For the lungs, a volume calculation error of below 70ml could be shown. From the segmentation results, functional parameters describing the local organ dynamics have been derived and visualized. The quantitative parameters were evaluated against conventional diagnostic techniques and showed good agreement, but with the benefit of a local and regional mobility characterization.

Table of contents

List of figures

List of tables

1 Introduction

1.1 Motivation

According to the World Health Organization, approximately 30% of all deaths worldwide result from diseases of the heart and lungs [1]. Common for most of these diseases is that they alter or restrict the mobility of the organs, and thereby reduce their ability to perform their physiological function: The transport of blood, for the heart, and the transport of air, for the lungs. Generally these diseases can be detected in early stages by functional analysis of the affected organs, and can be treated and cured if detected early enough. Conventional techniques, like Electrocardiography (ECG) for the heart, and spirometry for the lungs, can in general only detect alterations that restrict movement by 20% or more in global, which is not sufficient for the characterization of early disease stages. Therefore, medical imaging plays an increasing role in the early diagnosis of heart and lung function as well as therapy monitoring due to recent technological advancement, as with the help of medical image acquisition like Computed Tomography (CT) and Magnetic Resonance Imaging (MRI), the organ's function can be displayed and analyzed non-invasively from the outside and can also display local conditions.

Anyhow, the quantitative analysis of medical image data exhibits an increasing challenge in the clinical routine. Due to novel acquisition technologies, the spatiotemporal resolution of medical images is steadily increasing, making a manual analysis of the data more and more time consuming. Especially in the examination of anatomical and pathological structures which cover larger parts of the body, this trend becomes more and more noticeable in radiological practice. In thoracic imaging, where spacious scanning regions have to be recorded as well as dynamic aspects have to be considered, this progress offers a potential for improved diagnosis at the cost of more complicated analysis. At least parts of these complications can be strongly reduced with the help of automated computer support.

In both cases, the heart and the lungs, the first step for computer aided diagnosis is the extraction of relevant anatomical structures from the medical image data. This procedure is called *segmentation*, i.e. the division of the image data into objects of interest, and background, thereby splitting it into segments. Segmentation is a very active field of research, but regarding the question of mobility analysis, most existing approaches lack a number of fundamental prerequisites:

- Most existing methods do not consider the three-dimensional context as an integral part of their functionality.
- Most existing methods do not consider the temporal context as an integral part of their functionality.
- The approach needs to be applicable for a wide variety of image situations resulting from anatomically variability, patient condition, image noise, and acquisition artifacts.

The segmentation results can then be further processed to generate physical quantitative measures for diagnostic support. A strong benefit lies here in the high sensitivity in early stage diagnosis that can be achieved via image analysis compared to measurements from the outside. In the scope of this thesis, therefore methods have been developed that allow a local assessment of the heart's and lung's motion characteristics from dynamic MRI image data with the help of a model based segmentation scheme, that provide an intuitive visualization of quantitative functional physical and physiological parameters for the computer aided diagnosis support.

1.2 Objectives

Taking the fact that the spatiotemporal resolution of medical image data is steadily increasing, while the time for assessment stays more or less the same, it becomes apparent that automation of the analysis is indispensible. Anyhow, the attending physician always has to be incorporated in the final diagnostic decision, so a complete autonomy of algorithms is not the intended aim.

The focus of this work therefore was set on the development of a combination of automated image analysis techniques in conjunction with adequate methods for visualization of quantitative results to give computer aided diagnosis support for cardiologists and radiolo-

gists, which furthermore allow the physician to easily control and manipulate the results. Image data from dynamic MRI should preferably be analyzed as automated as possible and deliver exact results in a time that is practicable for clinical routine, i.e. several minutes. Diagnostic support for the physician then should occur in a way that the presentation of results can highlight areas that are found to be problematic for further inspection. Concurrently, quantitative physical measures should be generated from the image data to give additional information aiding diagnosis.

The goals of this work are the conception and implementation of new and improved methods for the diagnosis support of thoracic diseases with focus on diseases that alter mobility of the heart and lung. The aims can be divided into three thematic complexes and are therefore formulated separately.

To provide a basis for the extraction of medical parameters, relevant structures in the image have to be segmented. For this purpose, a segmentation scheme must be provided that

- Can segment dynamic image data automated, with low user interaction, and in short time.
- Provides robust results that are highly reproducible
- Incorporates as much a priori knowledge as possible, not only on single structures, but also on adjacent ones that are coupled to these
- Is flexible to anatomical, pathological, and image condition variations

For the analysis of cardiac function, the main objectives were:

- Development of methods to extract vital volumetric parameters of the heart
- Development of methods for local dynamic parameter generation to characterize regional motion behavior
- Development of meaningful visualizations of these parameters, especially the highlight of potential motion restrictions

For the analysis of respiratory function, the main objectives were:

- Development of methods for individual analysis of both lungs to give more specific predictions than conventional techniques
- Development of methods for the estimation of local parenchymal mobility to characterize regional motion behavior
- Development of methods that are sufficiently temporal resolved to display potential volumetric changes in breathing maneuvers

1.3 Structure of the Thesis

This thesis is organized as follows: Chapter 2 introduces the medical background for cardiac and pulmonary function analysis that is helpful for the understanding of the thesis. In each case, an overview over the relevant anatomy and physiology is given, and common restrictive diseases and diagnostic standards are presented. Chapter 3 lists current research that is done in the fields of multiple organ segmentation, cardiac functional analysis, and pulmonary functional analysis. Chapter 4 is divided into two parts. In the first, new methods for multiple organ segmentation in dynamic MRI images using different techniques of shape and geometrical correlation of objects are presented, as well as a manual correction possibility for shape model based segmentation. The second part shows the generation of diagnostic parameters from the segmentation results for the heart and lung. In chapter 5, several experiments for the validation of the proposed methods are presented, as well as the experimental results. All previously presented methods are evaluated step by step. Chapter 6 discusses the obtained results in detail, and Chapter 7 concludes the thesis with a summary of the treated aspects and an outlook for future work.

2 Background

This chapter gives an overview of the medical background this work is based upon. An understanding of the anatomical and physiological properties of the organs covered in this work as well as insight in clinical routine of their diagnosis is decisive for the understanding of the introduced methods.

First an overview of the function of the human heart, its diseases restricting movement and standard diagnose is enlisted. The second part covers the human respiratory system, its restrictive diseases as well as diagnosis possibilities.

2.1 Anatomy of the Human Heart

The human heart is a hollow, cone-shaped muscle which is located between the two lungs in the mediastinum (Fig. 2.1). It is bordered dorsally by the esophagus and the aorta, ventrally by the back plane of the breast bone and reaches caudally to the diaphragm, with which it is adhered. As a rule of thumb, two third of the heart are located in the left half of the thorax, one third in the right half. A healthy heart of an adult human is approximately as large as his fist and weights approximately 300 grams [2].

The heart is surrounded by a connective tissue like hull called pericardial sac. There are two layers to the pericardial sac: the fibrous pericardium and the serous pericardium. The serous pericardium, in turn, is divided into two layers, the *parietal pericardium*, which is fused to and inseparable from the fibrous pericardium, and the *visceral pericardium*, which is part of the epicardium. The epicardium is the layer immediately outside of the heart muscle proper (the myocardium). In between the parietal and visceral pericardial layers there is a potential space called the pericardial cavity which is lubricated by a film of serous fluid. The lubrication prevents that large friction forces develop between the two layers as the heart muscle contracts and relaxes.

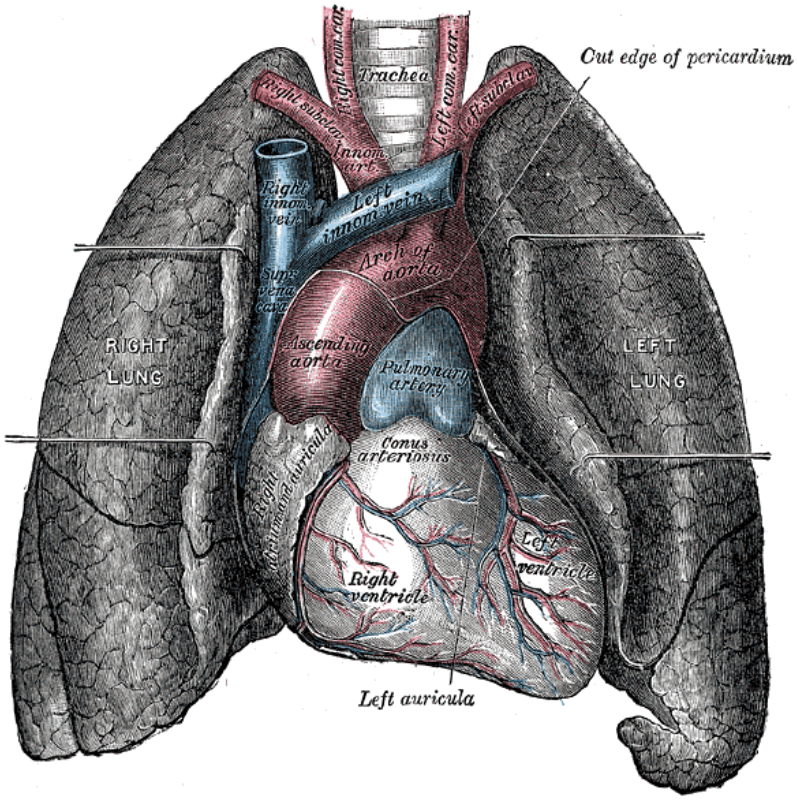

Fig. 2.1 Location of the heart in the mediastinum.

Source: [3].

The inside of the heart is built by the heart muscle (myocardium) and the inner heart wall (endocardium). The endocardium is backing the complete inside of the heart and forms the heart valves. The myocardium is the muscle that does the actual contraction of the heart and forms the largest part of the heart wall. Microscopically, the heart musculature is build of a net of involuntary striated, branched muscle fibers that wrap around the heart cavities in a spiral. Functionally the heart muscle is between smooth and striated musculature, as it possesses the spontaneous activity of smooth musculature, meaning it does not need an impulse from outside to contract, and the speed of striated musculature.

The myocardium is supplied with blood by the coronary arteries and thereby supplied with oxygen. The coronary arteries branch from the ascending aorta immediately after the aortic valve and divide into a left (Arteria coronaria sinistra, LCA) und a right artery (Arteria coronaria dextra, RCA). The left artery further divides into two main

branches, the circumflexus (CX) and the left anterior descending (LAD), which normally supply the heart's front and side walls. The RCA has one main branch called Ramus interventricularis posterior (RIVP) and supplies the back wall (Fig. 2.2).

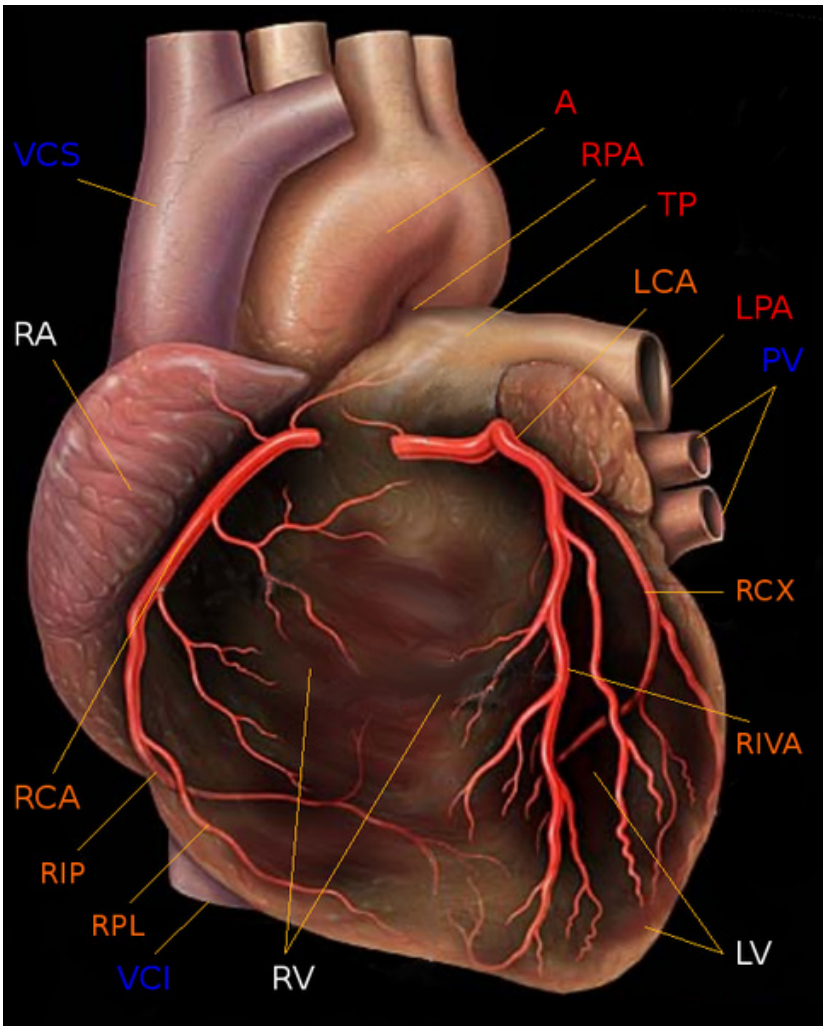

Fig. 2.2 Schematic display of the coronary arteries

Source: Adapted from [4]

Fig. 2.3 shows an overview of the complete heart and its in- and outflow tract. The heart is divided in a left and right part by the interatrioventricular septum, dividing the heart into two functionally separate and anatomically distinct units. Both parts consist of a superior atrium and an inferior chamber (ventricle). On both sides, the

lower ventricles are thicker and stronger than the upper atria. The muscle wall surrounding the left ventricle (LV) is thicker than the wall surrounding the right ventricle due to the higher force needed to pump the blood through the systemic circulation (see next page).

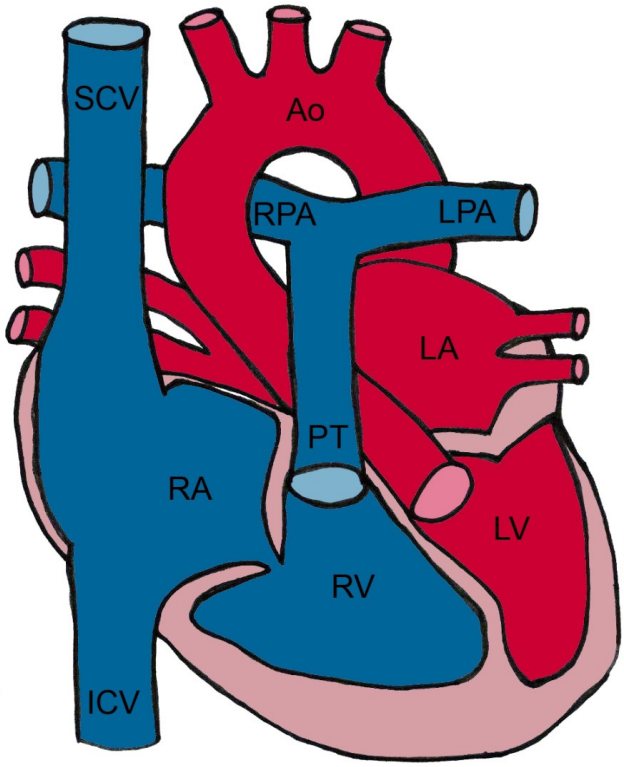

Fig. 2.3 Schematic display of the human heart and the great vessels

Source: [5]

Blood flows through the heart in one direction, from the atria to the ventricles, and out to the great arteries or the aorta for example. Blood is prevented from flowing backwards by the triscupid, mitral, aortic, and pulmonary valves. The mitral and tricuspid valves are classified as the atrioventricular (AV) valves, because they are found between the atria and ventricles. The aortic and pulmonary semi-lunar valves separate the left and right ventricle from the pulmonary artery and the aorta respectively (Fig. 2.4).

Fig. 2.4 The heart valves as seen from above.

Source: [3]

The function of the right side of the heart is to collect de-oxygenated blood, in the right atrium, from the body via superior and inferior vena cavae and pump it, via the right ventricle, into the lungs (pulmonary circulation) so that carbon dioxide can be dropped off and oxygen picked up. The left side collects oxygenated blood from the lungs into the left atrium. From the left atrium the blood moves to the left ventricle which pumps it out to the body (via the aorta).

Starting in the right atrium, the blood flows through the tricuspid valve to the right ventricle. Here, it is pumped out the pulmonary semilunar valve and travels through the pulmonary artery to the lungs. From there, blood flows back through the pulmonary vein to the left atrium. It then travels through the mitral valve to the left ventricle, from where it is pumped through the aortic semilunar valve to the aorta and to the rest of the body. The deoxygenated blood finally returns to the heart through the inferior vena cava and superior vena cava, and enters the right atrium again (Fig. 2.5, Fig. 2.6).

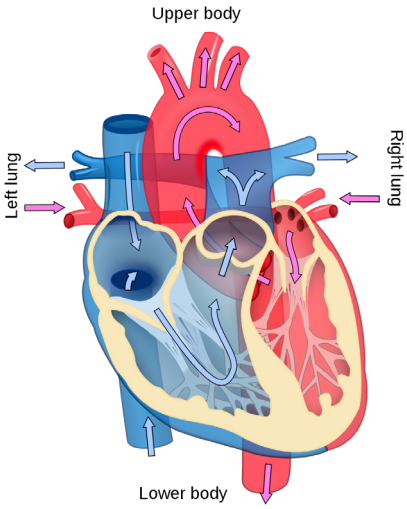

Fig. 2.5 Circulation diagram of the heart

Source: [6]

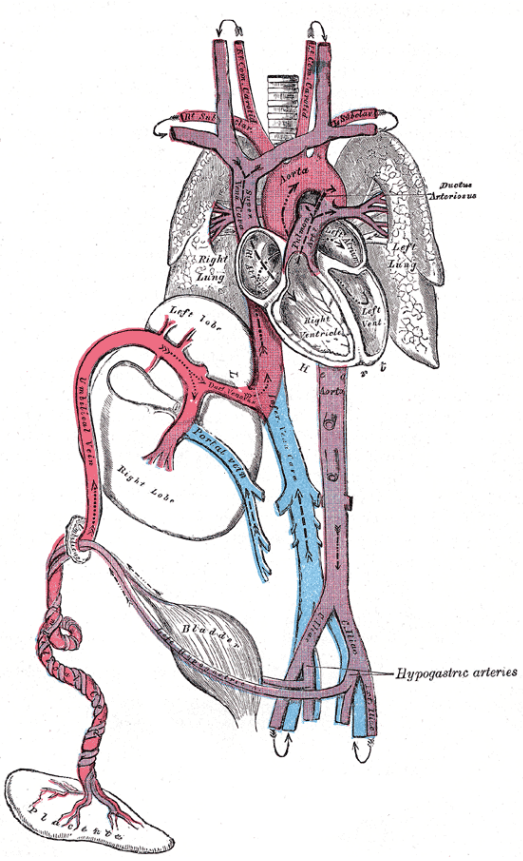

Fig. 2.6 Circulation diagram of the thorax

Source: [3]

Physiologically, the heart cycle is divided into two phases called systole and diastole. These are defined as follows:

- Systole: Contraction of the myocardium after closing of the AV valves and ejection of blood through the semilunar valves. Systole ends with the closing of the semilunar valves.
- Diastole: Relaxation of the heart muscle after closing of the semilunar valves and filling of the ventricles with blood through the opened AV valves. Ends with closing of the AV valves.

2.2 Cardiovascular Diseases

Due to the higher muscle density in the left ventricle, supply shortages with oxygen appear more often on the left side of the heart (e.g. due to coronary heart disease). Also, an infarct causes a relevant heart dysfunction and clinical symptoms much faster on the left ventricle then on the right side. Finally, the left heart chamber has to pump the blood a much longer way then the right side, which only has to supply the surrounding lungs. Therefore, cardiac diagnosis focuses mostly on the left ventricle. This chapter will introduce the most relevant cardiac diseases that affect the left heart function. Congenital heart diseases will be omitted because they are normally corrected after birth or in young ages if they display a vital impairment for the cardiac function.

2.2.1 Carditis

Carditis is a general term for an inflammation of the heart or its surroundings. Two specific incidents are of importance here:

- Myocarditis: The definition of myocarditis varies, but the central feature is an infection of the heart muscle, with an inflammatory infiltrate, and damage to the heart muscle, *without* the blockage of coronary arteries that define a heart attack. It may or may not include necrosis of heart tissue, and may include dilated cardiomyopathy (see below). Necrotic tissue leads to decreased muscle contraction and therefore can cause an undersupply of the body.
- Endocarditis: An inflammation of the inner layer of the heart that usually involves the valves. It can lead to a reduced valve function, heart insufficiency, and is deadly if untreated.

2.2.2 Heart Failure

“The inability of the heart to maintain cardiac output sufficient to meet the body's needs; it most often results from myocardial failure affecting the right or left ventricle” [7].

Left-sided failure

The term *left-sided failure* refers to a contraction insufficiency of the left heart, leading to a backing-up of blood in the pulmonary vessels. Consecutively this can lead to lung edemas and dyspnea (shortness of breath) on extortion, or even at rest in severe cases. Diverse etiologies can lead to a heart failure, such as myocardial infarction, aortic and mitral insufficiency, and coronary disease, which are described below.

2.2.3 Valvular Insufficiency

“A failure of a cardiac valve to close perfectly, causing valvular regurgitation;” [7]. Of importance for the left heart are insufficiencies of the aortic and the mitral valve.

Aortic Insufficiency (AI)

Also known as aortic regurgitation, the AI is the leaking of the aortic valve, leading to blood flow in reverse direction during ventricular diastole, from the aorta into the left ventricle. A common cause can be, if not congenital, a beforehand endocarditis. The stroke volume of the left ventricle is thereby increased by the regurgitation volume, which leads to a ventricular dilation over time. Although the dilation compensates the increased blood pressure in the ventricle, an overexpansion of the heart muscle can irreversibly damage the myocardium, leading to heart failure.

Mitral Regurgitation (MR)

Also known as mitral insufficiency, it is a closing incapability of the mitral valve. It can be caused by coronary disease or cardiomyopathy, among others. Due to the not properly closing valve, a backflow of blood from the left ventricle into the left atrium occurs during ventricular systole (see Fig. 2.7). The blood flowing back, called re-

gurgitation volume, leads in acute cases to a pressure increase in the left atrium as well as in the pulmonary veins, leading to an increased risk of lung edema. It also leads to a decreased ejection volume into the aorta, which can lead to an undersupply of organs with blood (ischemia). An MR occurring for a longer duration (congenital or chronic MR) leads to several anatomical adaptations to compensate the regurgitation. The left atrium and ventricle are dilated to compensate the increased pressure. Through the dilation, stroke volume is increased due to the Frank–Starling mechanism [8]. At the same time, the changed heart geometry due to the enlargement can negatively influence the mitral valve function in addition.

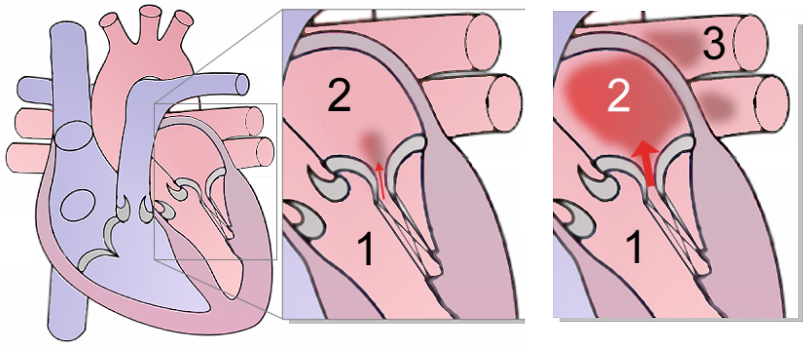

Fig. 2.7 Development of a mitral insufficiency

Middle: Light stage, Right: Severe stage; Red areas mark a regurgitation. Source: Adapted from [9]

2.2.4 Valvular Stenosis

A stenosis is “an abnormal narrowing or contraction of a body passage or opening” [7]. In case of the left heart, again the mitral and aortic valve cases are of importance.

Aortic valve stenosis (AS)

A narrowing of the aortic valve, which can be caused by calcification or an inflammation of the endocardium, among others. It leads to a decreased opening area of the valve, and the pressure gradient towards the ventricle has to be increased to allow the same blood flow for this reason. This results in a hypertrophy over time (thickening of the heart muscle) because the muscle must be able to apply the increased pressure. This is a problem because the supplying coronary arteries do not grow equally in size, so an undersupply of

the muscle can lead to ischemia. Thereby hypertrophy can again support a heart failure.

Mitral stenosis

A narrowing of the mitral valve, which leads to an increased pressure gradient between ventricle and atrium. Outcomes are similar as in aortic stenosis.

2.2.5 Coronary Heart Disease (CHD)

CHD, which is also called ischemic heart disease (IHD) and coronary artery disease (CAD), is a heart disease that causes a narrowing of coronary arteries, leading to inadequate blood supply to the myocardium. In most cases it is caused by atherosclerosis (calcification of the coronary arteries), resulting in a reduction of the vessel cross-sectional area and a reduction of vessel elasticity (Fig. 2.8). Other reasons can be thrombosis, embolism, and infectious or autoimmune inflammations of the coronary vessels. Due to the reduced blood supply of the heart muscle, it is undersupplied with oxygen (ischemia). Because the left ventricle has more muscle mass, it is rather affected than the right.

CHD can manifest in several varieties of severity:

- Asymptomatic CHD
- Symptomatic CHD:
- Angina pectoris: Chest pain because of reversible myocardial ischemia
- Myocardial infarction: Ischemic myocardial necrosis
- Left heart failure due to myocardial necrosis
- Cardiac dysrythmia
- Sudden cardiac death

Most symptoms can rise in varying intensities with angina pectoris as cardinal symptom. CHD is a slow process over many years, which is normally not found before acute symptoms arise (myocardial infarction).

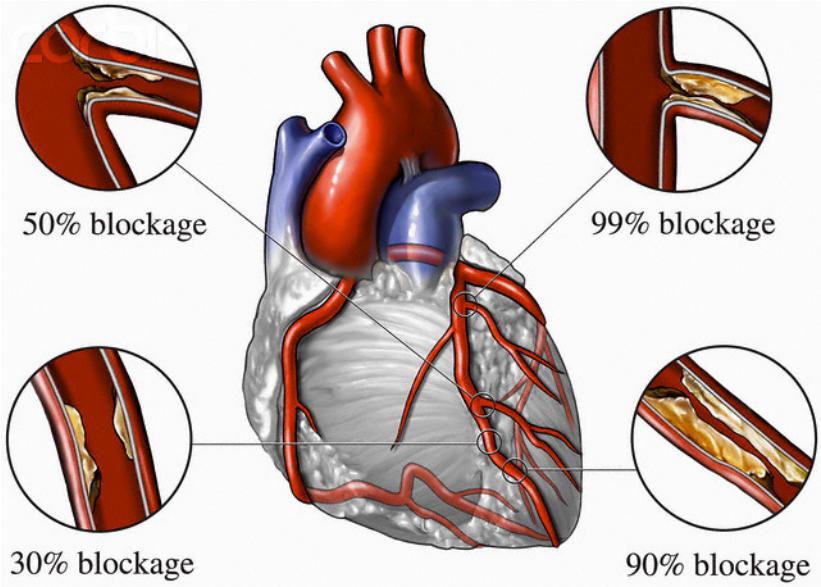

Fig. 2.8 Calcifications of the coronary arteries

These can lead to a coronary heart disease. Source: [9]

2.3 Cardiac Diagnosis

This section gives a short overview over commonly used techniques in the diagnosis of cardiac function which can be used to identify pathological heart conditions. Besides laboratory blood tests, which can be used for a range of diseases, these are:

- Electrocardiography (ECG): A non-invasive, fast and painless measurement method which can be used as first choice of diagnosis when a heart disorder is suspected. It measures the heart's electrical activity by application of electrodes at the skin surface, which allows observation of the heart beat waveform. It is very insensitive to early stages of diseases, but can detect e.g. progressed ventricular enlargements.
- Heart catheter: A catheter can be inserted into the coronary arteries through the blood vessels from the leg, and can directly monitor local blood pressure. Mostly the catheter is guided by fluoroscopic X-ray. An advantage is that in case of e.g. calcifications in the arteries, the therapy can directly be conducted through the catheter.
- Computed tomography angiography (CTA): Via X-ray based computed tomography, cardiac studies with good image resolu-

tion can be obtained in very short time. Drawback is however the radiation exposure of the patient.

- Cardiac Magnetic resonance imaging (MRI): MRI gained increasing importance in cardiology in the last years, due to the fast increases in technology and the lack of radiation exposure for the patient. MRI has a better contrast for soft tissue then CTA, allowing a better differentiation, but is much slower and has in general a lower spatial resolution.

A detailed overview can be found e.g. in [10].

2.4 Physiological Parameters of the Heart

Various parameters are routinely surveyed in cardiology to diagnose the heart function. The cardiovascular diseases listed in the last section regularly lead to a dilation of the ventricle, myocardial hypertrophy or ischemia and end in heart insufficiency if untreated. To aid in the diagnosis and quantification of these pathophysiological alteration, the parameters introduced in this chapter are commonly evaluated.

2.4.1 Volumetry

From volumetry, alterations of the heart in terms of size and pumping capacity can be evaluated. To further determine and quantify these changes, the following parameters are surveyed:

Blood Volume

The volume of the ventricular blood pool, calculated as the endocardial volume. The volumes at end-systole (ESV) and end-diastole (EDV) are hereby the most of interest. It gives an evidence for ventricular dilation and further parameters can be derived from it.

Stroke Volume

The amount of blood that is ejected in one full heart cycle. It is an indicator for infarcts, muscle diseases and heart valve diseases, which increase or decrease it, respectively. It can be calculated from the blood volumes as

$$SV = EDV - ESV \tag{2.1}$$

Ejection Fraction

The percentage of blood ejected over one cycle relative to the full heart volume (end-diastolic volume). It is again an indicator for myocardial infarction, muscle diseases and heart valve diseases and can be calculated as

$$EF = \frac{EDV - ESV}{EDV} = \frac{SV}{EDV} \tag{2.2}$$

Cardiac Output

The volume of blood that is pumped by the heart during one minute. It is a measure of the pump capacity of the heart. Given the heart rate (HR), it can be calculated as

$$Q = SV \times HR \tag{2.3}$$

Cardiac index

The amount of blood ejected in one minute relative to the patient's body surface area (BSA). This is for allowing the examination of the pump capacity for patients with different physical constitution. It can be calculated as

$$CI = \frac{Q}{BSA} \tag{2.4}$$

2.4.2 Wall mass

The weight of the myocardium and the papillary muscles. For a healthy heart, the mass is approximately 300 grams. In case of a hypertrophy of the myocardium as depicted in the last chapter, the muscle is thickened, so its mass increases, which is among others also a symptom for a valve stenosis. Given the density ρ_{ht} of heart muscle tissue, it can be calculated as

$$m_{wall} = \left(\left(V_{epi} - V_{endo} \right) + V_{pap} \right) \cdot \rho_{ht} \tag{2.5}$$

2.4.3 Wall motion

The wall motion describes the temporal change of the myocardial shape between end-systole and end-diastole. Main focus here is the local contraction and atony of the muscle. If immobile regions are observed, i.e. no change is observed for a region, this is mostly due to ischemic tissue, which can, among other things, point to a heart attack taken place previously.

2.4.4 Wall Thickness

The wall thickness is measured to objectively observe thickening and thinning of the heart muscle and to quantify these. Wall thickness is measure at end-systole, as the heart ventricle is then filled with blood and the relaxed muscle has minimal thickness. Several cardiovascular diseases lead to a change of the heart muscle, like ischemia (thinning), hypertrophic cardiomyopathy or valve stenosis (both thickening).

2.4.5 Wall Thickening

Wall thickening describes the change of the wall thickness between end-diastole and end-systole. It can be again used to locally diagnose ischemia of the muscle tissue, as a necrotic tissue does not contract anymore, and so the wall thickness remains unchanged.

2.5 Bull's Eye Diagram

The Bull’s Eye diagram is a cardiological diagnostic diagram used for the display of several local and global heart physiological parameters (see section 2.4). In this case, “local” means normally that distinct areas of the heart are evaluated individually, and a mean value for a parameter, e.g. myocardial movement, is given.

As can be seen in Fig. 2.10, the Bull’s Eye diagram resembles a dart board, subdivided in different sections. Each segment corresponds here to an anatomical area of the heart ventricle. Typically, the Bull’s Eye is used to analyze parameters of the left ventricle, although there also exist approaches for the right one [11], and also in combination with the coronary arteries [12].

In cardiology, different segment arrangements are used. The most established methods are a 20 segment division of the American Society of Nuclear Cardiology (ASNC) [13], which is mostly used in Single Photon Emission Computed Tomography (SPECT), and a 17 segment division standard of the American Heart Association (AHA) [14]. As this thesis focuses on cardiac MRI, only the AHA standard is regarded.

2.6 AHA Standard

The AHA was established 1924 in New York as a national health organization with the mission to prevent people from impairment, handicap, and death from cardiovascular diseases.

In 2002, the AHA published terms of reference for the visualization and subdivision of the Bull's Eye diagram, allowing a standardized analysis of left ventricular function. Background was the diversity of imaging modalities in cardiology and the hence resulting differences in heart orientation in the images. Images from Positron Emission Tomography (PET), e.g., are not oriented along the ventricle axis. To solve this problem, the AHA defined a guideline on how to reorient image data according to the heart axis. Hereby, slices have to be in line orthogonal to the long axis (axis from apex to mitral valve), so the slices then show the short axis view (Fig. 2.9). This alignment supports the visibleness of the two- and four-chamber view and of the arterial blood flow in the coronaries to the myocardium.

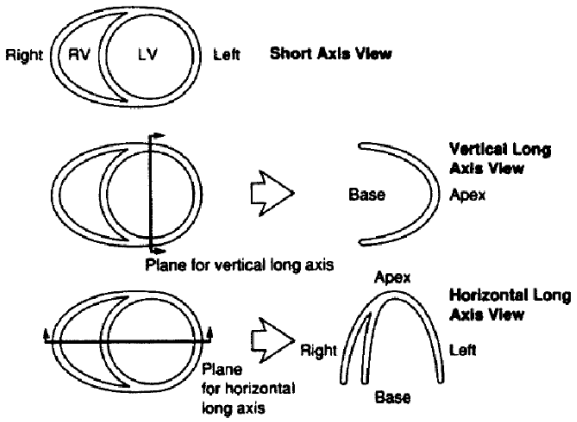

Fig. 2.9 Cardiological definition of the heart planes for the view in tomographic imaging modalities

Source: [14]

In addition, the AHA defines a subdivision of the left ventricular myocardium into 17 reasonable anatomical segments. Here, the ventricle is partitioned into three areas of equal size, plus the apex as individual structure. The three areas are called, from cranial to caudal, *basal, mid-cavity,* and *apical*. Fig. 2.10 shows the further subdivision of these areas into six segments of 60° (basal and mid-cavity), and four segments of 90° (apical). The single circle in the middle depicts the apex.

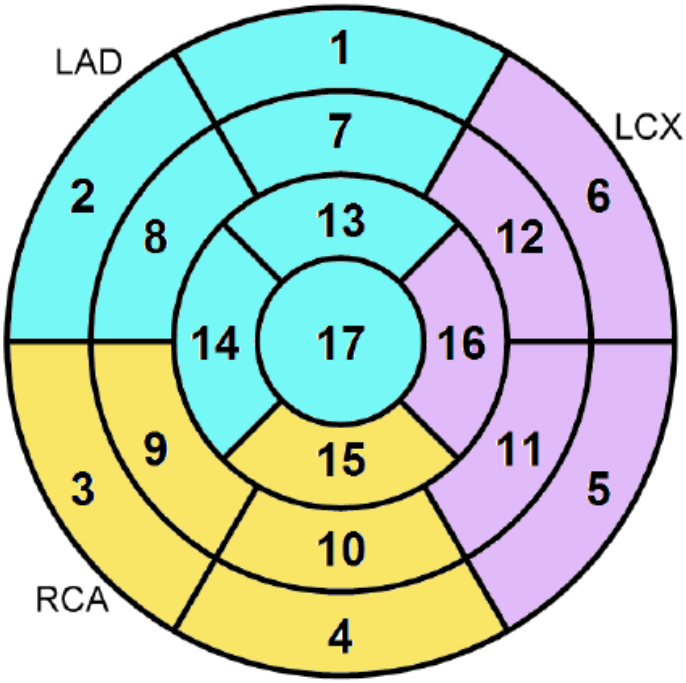

Basal Segments		Mid-cavity Segments		Apical Segments	
1.	basal anterior	7.	mid anterior	13.	apical anterior
2.	basal anteroseptal	8.	mid anteroseptal	14.	apical septal
3.	basal inferoseptal	9.	mid inferoseptal	15.	apical inferior
4.	basal inferior	10.	mid inferior	16.	apical lateral
5.	basal inferolateral	11.	mid inferolateral	17.	apex
6.	basal anterolateral	12.	mid anterolateral		

Fig. 2.10 Bull's Eye diagram according to the AHA standard

Source: [14]

2.7 Respiratory System

This section gives an overview over the human respiratory system and its functioning. A basic understanding of these topics is needed for the concepts presented in the “Methods” chapter. The description follows roughly the one given in [15].

2.7.1 Anatomy of the Respiratory System

The respiratory system is responsible for the exchange of gases between the body and the outside world. Hereby, the lungs have the function to restock the blood with oxygen from breathing air and to drain it of carbon dioxide created during metabolism. Upstream of the lung alveoli, in which the actual gas exchange takes place, are three other parts of the respiratory system: the naso-oropharynx, conducting airways, and respiratory bronchioles. A detailed overview of the complete anatomy can be found in Fig. 2.11. As this work focuses on lung dynamics, a description in more detail will only be given for the lower respiration tract, beginning at the trachea.

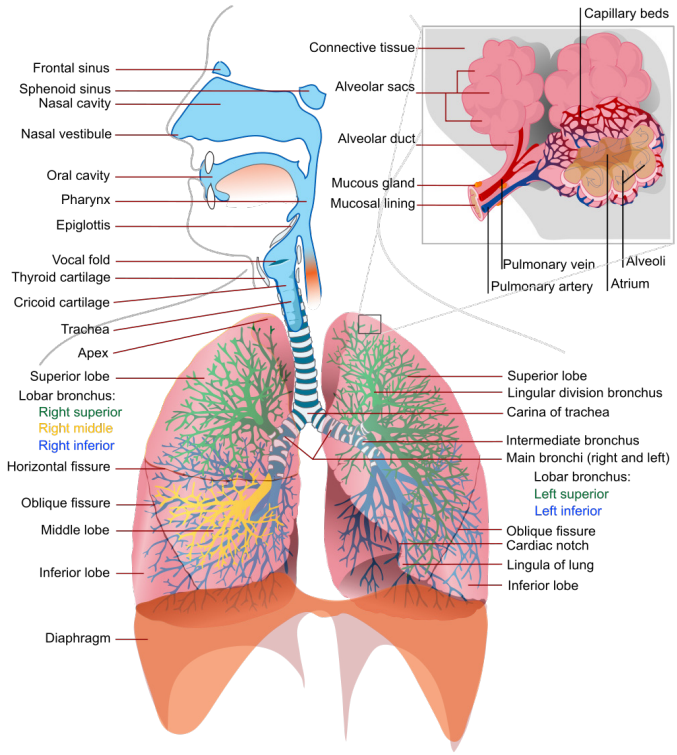

Fig. 2.11 The human respiratory system in detail

Source: [16]

The trachea, a muscular tube formed from C-shaped cartilages, branches repeatedly to form approximately 14 generations of air conduits for reaching the distinct lung segments. The trachea bifurcates at the carina into the right and left main stem bronchi. Because the right main stem has a gentler angle from the trachea, the right side contributes more to total aspiration as the left. After a few centimeters, the right side further subdivides into three smaller so-called lobar bronchi supporting the three lobes of the right lung, the right superior, middle, and inferior lobe. Same anatomy appears on the left side, but only with two lobes, left superior and inferior lobe (Fig. 2.12). On both sides, each lobe is further subdivided into several segments, which each have their own conducting airway. Also, each segment is supplied by an individual branch from the pulmonary artery. Therefore, each segment can be seen as an individual unit of respiration.

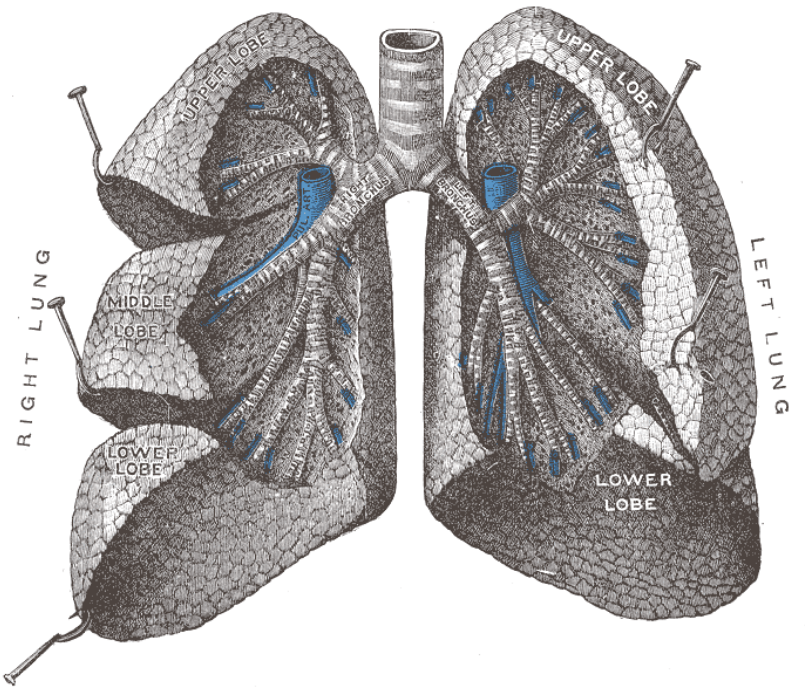

Fig. 2.12 The lung lobes

Source: [3]

As the bronchi get smaller, they get simpler and more thin-walled. In the smallest branches, called bronchioles, they do not consist of cartilages anymore, but of muscular fiber tunnels which actively regulate air flow to the alveoli. Here, epithelial cells allow the oxy-

gen of the air to reach capillary blood vessels, and vice versa for blood carbon dioxide. The millions of alveoli are embedded among capillaries to create an air–blood interface.

Both lungs are surrounded by a two-layered serous membrane called pleura, which has a thin fluid-filled cavity between the layers. The outer pleura is attached to the chest wall, the inner pleura covers the lungs. Lung movement during respiration is possible because of the reduced pressure in the cavity, passing all chest wall movements to the lungs, and the fluid acting as a lubricant so the lungs can slide effortlessly in the thorax.

2.7.2 Physiology of the Respiratory System

To repeatedly support the alveoli with fresh breathing air, the chest has to expand and inflate itself through constant movement. This is done approx. 15 times per minute in adults, and approx. 25 times per minute in children. The chest expansion is called inspiration, and transports air with high oxygen content to the alveoli; the contraction is called expiration and allows the evacuation of air with high carbon dioxide level and low oxygen content.

During inspiration, the diaphragm contracts, thus lowering the diaphragm dome and enlarging the lung lobes (abdominal breathing). Also, the external intercostal muscles running between the ribs contract, resulting in an enlargement of the rib cage in ventral direction, and to a small amount in lateral direction (shallow breathing). The enlargement of the lung cavity leads to a reduced air pressure in it, which creates suction of air into the lungs.

While inspiration is an active process, expiration happens mostly passive through relaxation of the intercostal and diaphragmatic musculature. The lung tissue tightens again and leads to a contraction of the thoracic cavity. In forced exhalation, also the internal intercostal muscles contract, leading to a lowering of the ribs and thus a compression of the chest. Fig. 2.13 gives an overview of the breathing physiology.

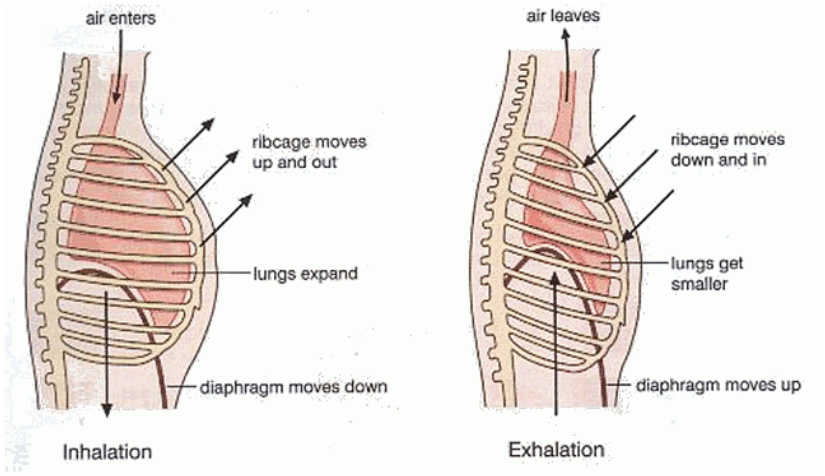

Fig. 2.13 Physiology of the human respiratory system

Source: Adapted from [17].

2.7.3 Lung Volumes and Capacities

During each breathing cycle, about 0.5 liters of air are inhaled and exhaled, depending on body size and build. Only two third of this air reaches the alveoli, one third remains in the trachea and bronchi und thus does not contribute to gas exchange.

With an average of 15 breathing cycles per minute, a healthy male adult thus in- and exhales thus approximately 7.5 liters of air per minute. With strong inspiration, an additional 2-3 liters of air can be inhaled; with strong expiration, an additional approx. 1 liter can be exhaled. These volumes, along with some other and derived measures, can be used for functional analysis of respiration.

The following table lists the most important static and dynamic measures for the diagnosis of respiratory function (adapted from [18]).

Table 2-1 Common static and dynamic measures in respiratory diagnosis

Measurement	Calculation	Description
Tidal volume (V_T)	measured	The amount of air breathed in or out during normal respiration. The volume of air an individual is normally breathing in and out.
Expiratory reserve volume (ERV)	measured	The amount of additional air that can be pushed out after the end expiratory level of normal breathing. (At the end of a normal breath, the lungs contain the residual volume plus the expiratory reserve volume).
Inspiratory reserve volume (IRV)	measured	The additional air that can be inhaled after a normal tidal breath in. The maximum volume of air that can be inspired in addition to the tidal volume.
Vital capacity (VC)	$VC = IRV + V_T + ERV$	The amount of air that can be forced out of the lungs after a maximal inspiration. Emphasis on completeness of expiration. The maximum volume of air that can be voluntarily moved in and out of the respiratory system.
Inspiratory capacity (IC)	$IC = V_T + IRV$	The maximal volume that can be inspired following a normal expiration.
Residual volume (RV)	measured	The amount of air left in the lungs after maximal exhalation. The amount of air that is al-

		ways in the lungs and can never be expired.
Total lung capacity (TLC)	TLC = IRV + V_T + ERV + RV	The volume of air contained in the lung at the end of maximal inspiration. The total volume of the lung.
Forced vital capacity (FVC)	measured	The amount of air that can be maximally forced out of the lungs after a maximal inspiration. Emphasis on speed.
Forced expiratory volume 1 sec (FEV1)	measured	The maximal amount of air that can be exhaled in one second after full inspiration.
Forced expiratory volume 1 sec in % (FEV1%)	measured	The maximal amount of air that can be exhaled in one second after full inspiration relative to (forced) vital capacity. For healthy persons approx. 80%.
Functional residual capacity (FRC)	FRC = ERV + RV	The amount of air left in the lungs after a tidal breath out. The amount of air that stays in the lungs during normal breathing.
Anatomical dead space	measured	The volume of the conducting airways. Measured with Fowler method [18].
Physiologic dead volume	$V_T \frac{P_{A(CO_2)} - P_{E(CO_2)}}{P_{A(CO_2)}}$	The anatomic dead space plus the alveolar dead space. P_A, P_E: Partial pressure of carbon dioxide in arterial blood and expired air.

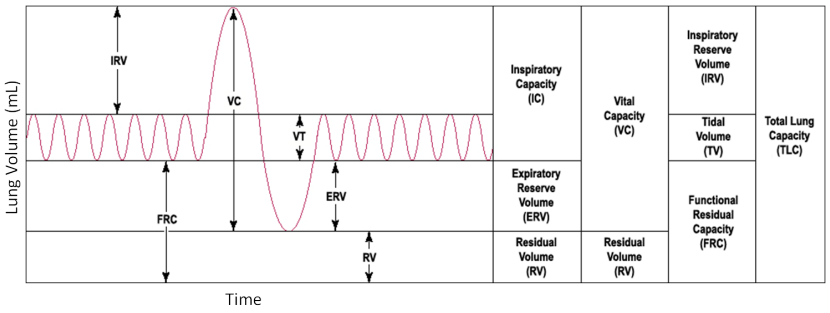

Fig. 2.14 Static lung volumes and capacities

Source: Adapted from [19]

2.8 Restrictive Respiratory Diseases

From a physiological side of view, respiratory diseases are subdivided into obstructive and restrictive diseases. Obstructive diseases originate from a total or partial narrowing or blockage of airways and a resulting increased airways resistance. Restrictive diseases decrease the elasticity of the lung tissue. An overview of the changes in breathing behavior can be seen in Fig. 2.16: Obstructive lung diseases (OLD) push the position of the flow-volume curve to the left due to hyperinflation. The curve displays different patterns with various forms of upper airway obstructions (UAO), with reduction in respiratory flow if the obstruction is outside the thoracic cavity and reduction in expiratory flow if the obstruction is caused by a fixed deformity. In restrictive lung diseases (RLD), volumes are reduced, but flow for any point in volume is mostly normal.

As the methods developed in this work mainly focus on movement restriction, obstructive diseases will not be covered in detail. Anyhow, the developed methods for computer aided diagnosis could also be used for obstructive diseases just as well by showing up changes in breathing behavior.

Common for all restrictive diseases is the increase of airways resistance due to a reduced elasticity of the lung tissue. Symptomatic is a drop of the most lung volumes and capacities as listed in the last chapter (Fig. 2.14). Several etiological diseases will be specified in this chapter.

2.8.1 Pleural effusion

A pleural effusion is an accumulation of a fluid in the pleura. Due to the rigidity of the outer surroundings of the pleura (bones, muscles, and ligaments), it leads to a compression of the soft and elastic lung tissue. If enough fluid is accumulated, the amount of air that can be in- and exhaled is reduced. Four types of fluid can lead to a pleural effusion: Blood, serous fluid, chyle (lymph fluid), and pus. There are many possible causes for a pleural effusion, e.g. a lung tumor, cardiac diseases, infections (like tuberculosis), and traumatic (like a rib fracture). Typical symptoms are shortage of breath and insufficient supply with oxygen, among others.

2.8.2 Adhesive pleurisy

Also called dry pleurisy, an adhesive pleurisy is an inflammation of the pleura without effusion of serum, resulting in adhesion of the opposing layers of the pleura. This prevents proper movement of the layers against each other, thus decreasing lung motility. There can be many different causes for pleurisy, with viral infections being the most common. Typical symptoms are strong chest pain resulting from the friction of the pleural layers, shortage of breath, fever, and coughing.

2.8.3 Pulmonary Fibrosis

Due to chronically inflammations of the lung, fibrous connective tissue is developed out of the lung parenchyma, which means a scarring of the lung tissue. The connective tissue stiffens the lung, from which a decrease of compliance results. Also, it does not contribute to gas exchange, thus further reduces the functional capacity of the lung. As a result the patient develops breathing irregularities, shortage of breath, chronic dry cough, and often fever. Most commonly known example is the asbestosis, caused by continuing inhalation of asbestos fibers. A fibrosis is irreversible, as the scarred tissue does not restore itself to its former healthy condition.

2.8.4 Pulmonary Edema

A pulmonary edema is an accumulation of fluid, typically blood, in the lungs. It can be caused by heart diseases, leading to a failure of the heart to remove blood from the lungs, like left heart failure, or a

direct injury of the lung. It leads to a reduced oxygen intake in the blood (hypoxia) and can even lead to respiratory failure resulting in death when untreated. Therapy focuses on removing the cause of the edema and maximizing respiratory function.

2.8.5 Lung Cancer

Cancer is an uncontrolled division and proliferation of cells that eventually forms a mass known as a tumor. Malignant tumors grow aggressively and can invade other tissues of the body, called metastasis. Depending on the stage of the disease, a lung tumor can have distinct influence on respiration, as it occupies space in the lungs and stiffens the tissue. Symptoms are coughing, difficulties in breathing, chest pain, and paralysis. According to the World Health Organization (WHO), several types of lung cancer are distinguished [20].

Adenocarcinoma

A tumor originated in epithelial cells in glandular tissue. Adenocarcinomas account for approximately 40% of lung cancers. [21]

Squamous cell lung carcinoma (SCC)

A malignant tumor originated in squamous epithelial cells, which are backing the bronchi. It is one of the most common types of lung cancer, identified in 25-35% of lung cancer occurrences.

Small cell carcinoma (SCLC)

A very aggressive tumor. Most cases arise from the primary and secondary bronchi and show rapid growth. It also tends to quickly develop metastasis. It has a frequency of approx. 15%.

Large cell lung carcinoma (LCLC)

A general term for epithelial tumors that can’t be classified in the former three sections. Common for all subclasses is a larger tumor cell size than in SCLC. They comprise to about 5-10% of all lung cancers.

Other

There are also some rather uncommon cases of tumors arising from non-epithelial cells, like sarcoma (from connective tissue), or mesothelioma (from mesothelium, like pleura).

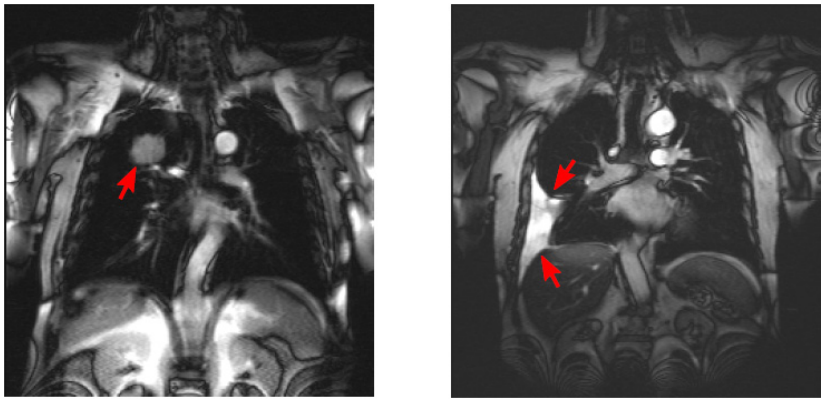

Fig. 2.15 Typical appearance of lung tumors in MRI

a) Bronchial carcinoma; b) Mesothelioma with pleural effusion; Source: [22]

2.9 Respiratory Diagnosis

Besides of the importance as differential diagnosis, lung functional analysis can be very useful for getting an objective diagnosis of a dysfunction, the reversibility of a bronchial obstruction or therapy side effects, like in radiation therapy. It can also be seen as a screening possibility for epidemiological questions. The most important and most commonly used methods include according to[23]:

- Spirometry
- Bronchospasmolytic test
- Body plethysmography
- Arterial Blood Gas Test

2.9.1 Spirometry

Spirometry is the most commonly performed measurement for lung functional analysis. It is based on measuring the air current while inspiring and expiring with an air flux sensor. It is used at basal respiration and while performing defined breathing maneuvers. From the flow values measured this way, some medical parameters given in

the last chapter can be deviated. Also some additional parameters like the maximal expiratory flow (Peak Flow, PEF) can directly be gained.

For clinical diagnostics, especially the expiratory values are of interest. In particular in case of chronically diseases, the FEV1% value is an important indicator of condition progress.

Results of spirometry are often displayed graphically in a flow-volume diagram. Here, the flow value is printed on the y-axis against the expiratory volume on the x-axis. Pathological respiratory patterns can be identified in this diagram the easiest way, as well as the cooperation of the patient, who might not be willing or able to perform the test (e.g. children), but is essential for correct results. Fig. 2.16 shows the alteration of the flow-volume curve under several pathological conditions.

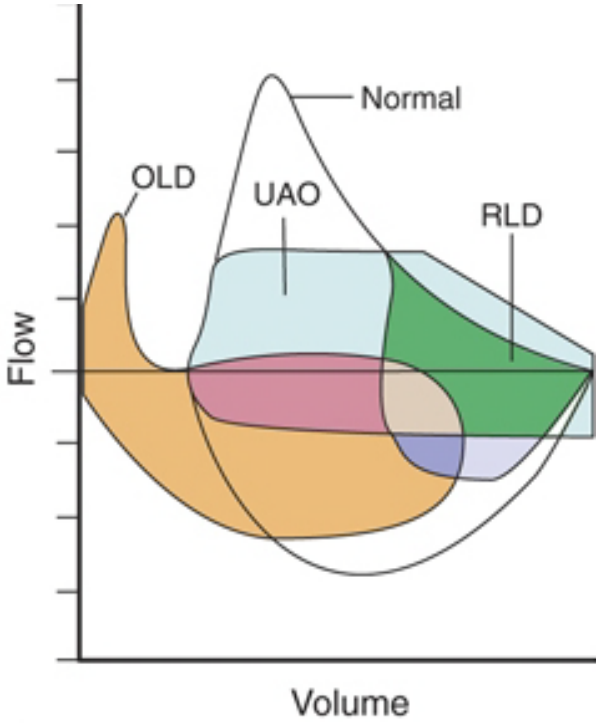

Fig. 2.16 Flow-volume curves under several conditions

Alteration of flow-volume curves under several conditions: OLD: obstructive lung diseases; RLD: Restrictive lung diseases; UAO: Upper airway obstruction. Source: Adapted from [24]

2.9.2 Bronchospasmolytic Test

A bronchospasmolytic test is performed by undertaking a pulmonary function test before and after an aerosol bronchodilator is given to the patient. Normally a Beta-2 selective sympathomimetic is used because it causes bronchodilation but does not stimulate the heart. This way the amount of bronchoconstriction that was present can be measured, as well as how responsive the patient was to a bronchodilator medication. The test assesses the degree of airway obstruction that is reversible. It can be used to differentiate between asthma, which is normally indicated with a reversible obstruction under bronchodilator medication, and other diseases.

2.9.3 Body Plethysmography

Also called “Body box” for short, a body plethysmography is a very sensitive test of lung function which is mostly performed in the clinical sector. During the measurement, the patient is sitting enclosed in an airtight chamber in which the pressure p_C changes due to inspiration and expiration. The patient is breathing through a pneumotachometer, from which airflow can be measured, while a mouth pressure transducer measures alveolar pressure p_A. Additional to the parameters from the flow measurement (like with a spirometer), the thoracic gas volume (VTG), compliance C (strain resistance of lung tissue) and airway resistance R_{AW} can be measured or calculated.

$$VTG = \frac{V_C \cdot \Delta p_C}{\Delta p_A}$$
$$C = \frac{\Delta V_A}{\Delta p_A} \qquad (2.6)$$
$$R_{AW} = \frac{p_{mouth} - p_A}{\dot{V}}$$

Here, V_A and V_C denote the volume of the lung and chamber, respectively, $\dot{V}$ denotes the airflow (temporal volume change). With these measures it is possible to distinguish between restrictive and obstructive diseases, examine the resistance to airflow and determine the respiratory response to medication.

2.9.4 Arterial Blood Gas

An arterial blood gas test (ABG) is an indirect method to monitor the function of the lung. Standard procedure is to extract and analyze arterial blood from peripheral capillaries, e.g. from the earlobe. With the method, the constellation of blood gases, namely carbon dioxide and oxygen, and the pH value are displayed, which eventually represents the final result of the different lung tasks. With the help of it, the degree of efficiency of the lung as organ for gas exchange between body and outside world can be evaluated. A drawback is that the gas values can also be altered by non-pulmonary factors and diseases.

3 State of the Art

3.1 Medical Image Segmentation

Knowledge of the individual morphology of a patient is an important constituent for a patient specific model and prerequisite for many model based therapy approaches. The extraction of morphological information from image data is called segmentation.

A manual segmentation of image data is an alternative in the clinical routine only in special cases because of the high time effort. But, a reliable automatic segmentation is usually a complicated problem. For this reason, segmentation is often the limiting factor for the application of further computer assisted methods in diagnosis, therapy planning and monitoring.

In the last two decades, model-based approaches have been established as one of the most successful methods for image segmentation. The central assumption of these approaches is that structures of interest have a repetitive form of geometry and a distinct gray value distribution at their border, so the methods are based on matching a model which contains information about the expected shape and appearance of the structure of interest to new images. Due to the inherent a-priori information, model based approaches are more stable against local image artifacts and perturbations than conventional low-level algorithms. Because biological objects show a considerable natural variability, it is helpful to include information about common variations in the model. An overview in detail about common techniques for single organ segmentation can be found in [25].

3.1.1 Multiple Organ Segmentation

In cases of problematic image data, it can be beneficial to not only use a single trained model, but to incorporate knowledge from multiple objects and their interrelations. This is especially helpful when

the objects to be segmented only show diffuse borders, image artifacts, or a high noise level. The segmentation of multiple objects by utilization of additional mutual information is a relatively new and active field of research. This section gives an overview over recent achievements and methods developed in the field.

The first type of methods to find correlations between objects which can be found is based on geometrical information. Yao *et al.* for example describe a statistical location model of multiple organs used for initialization of a segmentation search [26]. They train a statistic location model of several organs in relation to the spine by calculating the mean relative location and its variances among the training data. Their organ models can then be fitted to unseen image data using an a posteriori maximization of the model inside the variability range.

Another approach by Shen *et al.* uses two distance-based cost functions to generate spatial constraints between multiple interacting surfaces during segmentation [27]. The cost functions penalize deviations from trained mean surface to surface distances using a Gaussian mixture model. These costs are applied as additional force term for active volume models.

An approach by Kainmueller et al. [28] calculates correspondences between vertices of adjacent objects. They then define line segments between corresponding vertices which are used as shared displacement direction and as shared intensity profiles. With the help of this, an overlap of the adjacent structures can be excluded.

Another method is to find a correlation between objects by using shape information. Frangi *et al.* describe a way to distribute corresponding landmarks on multiple object by nonrigidly registering these objects, and use these landmarks to train a shape model of the joint objects [29].

Tsai *et al.* present a parametric multi-shape model by applying principal component analysis on multiple signed distance functions as implicit representation of multiple shape classes in an image and derive a parametric model [30, 31]. They thereby calculate a coupling between multiple shapes in the image, and can then use the co-dependencies to support the segmentation. They apply such models

to the segmentation of subcortical brain structures and lower abdominal structures (prostate gland, rectum, and obturator muscles).

Babalola et al. [32] build a composite active appearance model on the basis of explicit surface-mesh representations of multiple brain structures. They apply this model to obtain a good initialization of brain structure models to accurately segment the caudate in a single object segmentation framework. Composite statistical shape models yield a tight coupling of the deformations of multiple objects. Ideally, no overlap between adjacent objects should be possible in model space. Anyway, the approach does not allow for a free form multi-object segmentation, as model deformation is bound to the respective shape space.

Okada *et al.* train and apply statistical atlases of the liver and its neighbors in CT images, and use these for an initial region extraction. Afterwards, segmentation is refined using shape models of multiple organs on different levels of detail in a hierarchical order [33].

Lu *et al.* presented the training of statistical shape models of multi-object complexes based on medial representations [34], while Cates *et al.* train a landmark based model of a multi-object shape complex by optimizing landmark correspondences in joint shape space [35].

3.2 Cardiac Diagnosis

This chapter introduces different solutions available for the functional analysis of the heart. The main focus is on approaches from current research, as for commercially available solutions often not sufficient information is available for an adequate comparison. Common for all approaches in computer aided cardiac diagnosis is that functional parameters of the heart are generated from an initial segmentation of the left ventricle from dynamic MRI or CT images. Also some segmentation approaches which do not focus on a fully functional analysis are presented for comparison.

3.2.1 Commercially Available Products

Leading manufacturers of CT and MRI imaging modalities like Siemens, Philips, and GE often offer specialized image processing and analysis modules alongside their imaging products. These modules

are typically integrated in the fundamental systems of image administration and can usually not be bought as a separate product. This allows for an efficient workflow for the user, as he does not have to change work place for post processing of images. Due to the strong integration, however, it is nearly impossible to obtain information over the used algorithms and methods in these modules. Also, not all features are listed and documented in detail or are not publicly available. There exist a couple of further, mostly smaller companies that produce and sell heart diagnosis applications as well, like Pie Medical, Visage Imaging, and Vital Images, but the restrictions in public access to their methodology are the same as with the large manufacturers. Although some of the applications generate similar analysis options as presented in this thesis, the information accessible via the manufacturers' web pages is in general not enough to allow a reasonable delineation and comparison of the used methods, therefore the next section will list recently published research projects in the field of cardiac motion analysis.

3.2.2 LV Segmentation and Functional Analysis

Manual segmentation of the left ventricle from 3D+t MRI data is highly time consuming, as the endocardium and epicardium has to be delineated in each slice in each time step, and is therefore not applicable in clinical routine. Further there is a large inter-observer variability when segmenting manually. Therefore research is done to automate this step, and thereby to increase reproducibility and to lower time effort and variability. In this section some existing approaches are presented. The section focuses on methods in which cardiac parameters are extracted from the segmentation results, but also describes some interesting segmentation approaches.

A semi-automatic method is presented by Relan et al. [36], which they declare to greatly reduce the time effort for ventricular segmentation. In this method, each a long and short axis slice of the left ventricle are combined. These 2D slices are transferred in a 3D coordinate system according to their DICOM headers positional information. The user then has to mark the mitral valve plane, apex point and the contours of epicardium and endocardium. Afterwards planes are generated parallel to the mitral valve plane at a distance of a millimeter each, which each define four intersection points with the drawn contours. These points are then interpolated by Bezier

curves in the intersection plane, which together with the user drawn contours are used to generate a 3D surface. A drawback is that this procedure has to be repeated for each time step to be analyzed.

A method based on a combination of low-level segmentation techniques is shown by [11]. Interesting here is the extension of functional analysis to the right ventricle and the combination of dynamic parameters with a quantification of scar tissue which can help to determine correlations between mobility and heart disease progression.

Another method presented by Säring et al. [37] uses demon-based registration according to Thirion [38] to register a manual segmentation of the epicardium and endocardium in end-systole and end-diastole to other time steps. Registration is done slice-wise, but a 3D surface is generated again afterwards for each time step. In contrast to the previous method, this approach is able to segment a complete time series at once, but with the 25-30 minutes of the initial manual segmentation necessary still not really applicable for clinical routine.

The methods of Relan and Säring are integrated into the Heart Analysis Tool (HeAT) [39], which is designed for the analysis of spatiotemporal MRI sequences and pathological studies of infracted tissue.

A method based on level sets is demonstrated by Corsi et al. in [40]. It first combines the acquired 2D slices of the short heart axis in a 3D volume. Afterwards, four to six slices lying between apex and mitral valve are selected in end diastole as well as in end systole. The user has to define a couple of points in each of these slices which define an initial contour of the endocardium and epicardium. These points are connected to a polygon giving an initialization of the level set function. This function defines a partial differential equation which iteratively alters the initial contour under the effect of two integrated force terms: A regulatory force penalizing high surface curvature, and an image driven force which locally pulls the surface to high gray value gradients. In an evolutionary process, the surface is translated and deformed until the force terms reach equilibrium. The method shows a low inter- and intra-observer variability, but still needs a distinct manual input for preparation of the initial contours.

Spreeuwers et al. [41] presented an approach based on active contour segmentation. The active contour method can be seen as a "rubber band" trying to attach itself to the strongest nearby gray value gradient by simultaneously trying to prevent its shape. As this can lead to problems with borders lying close together, as it is the case for the myocardial wall, they combined two active contours to a common system able to preserve its topology. This leads to a robust segmentation with low intra-observer variability. The processing is done in single 2D slices, however, thus not regarding depth information of the data set.

Besides the above described methods, also statistical shape models have been successfully used for ventricular segmentation. An interesting method for analysis of end-systolic and end-diastolic volumes is presented by Fritz et al. [42]. They use a temporally correlated model of both end heart phases which are simultaneously segmented to compensate for image acquisition artifacts in one time step with the help of the other. The so-called bi-temporal model is used to segment the endocardium of the left and right ventricle and the epicardium of the left ventricle in high-resolution CT data sets.

Lorentz and van Berg [43] describe the generation of a comprehensive shape model of the cardiac chambers and connected vessels as well as the coronary arteries. They use a global registration of the model to patient data on multi-slice CT images and acquire segmentation accuracy of below 5mm for all structures.

A 3D Active Appearance Model (AAM) of the heart is used for gaining an initial segmentation of the left ventricle in MRI by Andreopoulos and Tsotsos [44]. They compare several search routines which do not rely on global similarity transformations. The initial result is then refined by 2D+t Active Shape Models to gain better local contour results.

Especially designed for sparse image data with arbitrarily oriented slice orientation is an active shape model based method presented by van Asses et al. [45], called SPASM. Sparse here means images with largely undersampled regions. Because the approach does not rely on a trained appearance model, it is also applicable for different imaging modalities.

3.3 Pulmonary Diagnosis

Most pulmonary diseases alter pulmonary mechanics by changes in tissue elasticity, airflow resistance or a combination of both. The most frequently applied test to assess such changes is spirometry (see section 2.9.1), with which static and dynamic volumes as well as parameters as resistance and compliance can be determined. A common spirometric parameter is the volume expired in the first second of forced expiration (FEV1). It is used e.g. for grading of chronic obstructive pulmonary disease (COPD) (Global Initiative for Chronic Obstructive Lung Disease (GOLD) classification) [46], for monitoring of Asthma [47] or for follow up after lung transplantation [48].

Since spirometry is an inherently global measurement, it can only measure the combined air flow from both lungs. In disease with regional inhomogeneous distribution favoring a single lung, pathological changes of lung function might pass unnoticed due to averaging with the less affected lung. A spirometric test for single lungs would be able to detect such changes and would thus improve functional pulmonary assessments. An example where this would be relevant is single lung transplantation. Here alteration in FEV1% is taken as indication of organ rejection induced bronchiolitis obliterans syndrome but changes in the transplanted lung can be covered up by the remaining contra lateral lung [49]. Better sensitivity of regional functional changes might also improve treatment in COPD. The Global Initiative for Chronic Obstructive Lung Disease (GOLD) provides a severity classification of COPD divided into stages depending on the deviation of dynamic volumes from the index value. They recently dropped the GOLD stage 0 (chronic cough, but no changes in spirometry) because there was no clear evidence that these patients progress to stage 1 (minor ventilation obstruction) [46]. Yet, a subpopulation of the patients with clinical symptoms but normal lung function does progress to stage 1 and might profit from preventive treatment. A spirometric test for single lungs might be able to identify some of these patients and help to improve long term outcome.

Topics of recent research for individual and regional assessment of lung function include methods for the determination of diaphragm movement as a surrogate for breathing motion, for determination of

local motility of the parenchyma, and methods for tumor motion tracking for the preparation of radiation therapy [50]. Common for all research is the necessity of dynamic imaging.

This first approaches to regional lung function through imaging used radiography, fluoroscopy, and ultrasound, initially to measure the movement of the diaphragm [51-55]. Modern multi-detector CT scanners allow the acquisition of up to ten volume data sets over a breathing cycle with only slightly reduced image quality compared to static CT [56]. Still, the radiation exposure of the patient is high in these procedures [57], which is why 4D CT scan are mostly limited to radiation oncology.

Presently, MRI has more or less substituted other modalities for this purpose. Advantages are the lack of radiation and the better reproducibility of MRI because of its operator and projection independence. Further, with dynamic MRI, respiratory motion can be imaged with a temporal resolution in three dimensions with up to two images per second and in two dimensions with up to 10 images per second. It has been shown, that functional parameters as forced vital capacity (FVC) and forced expiratory volume in the first second (FEV1) can be derived accurately from dynamic MRI and the individual contribution of single lungs can be differentiated [58-60]. More recently, it was shown that the changes of thoracic diameters measured on dynamic 2D MRI of single lungs in sagittal orientation are well correlated to spirometric lung volume changes measured simultaneously. These measurements allowed to compute meaningful volume-time and flow-volume curves for single lungs [61].

Local motion estimation: Although the previously stated methods make an important advancement in functional respiratory analysis, they are in general not able to predict local movement impairments that become little noticeable globally and can therefore not be predicted. For the calculation of local parenchymal mobility, two promising approaches can be found in literature.

- Grid-Tagging: In this technique, which originates from motion analysis of the heart, a grid is impressed on the lung tissue in the image, which intersection points are tracked, usually in dynamic 2D image sequences [62, 63]. Recently, also dynamic 3D image sequences have been reported successfully analyzed with the help of this method under em-

ployment of a contrast agent gas like Helium-3 [64, 65]. Problematic in this approach is the low signal-to-noise ratio in dynamic MRI images, as well as the short impression times, which make it difficult to monitor a complete breathing cycle. In the 3D case, also the necessity of a contrast agent is a drawback.

- Deformable registration: An alternative approach for the calculation of deformation fields and thereby analysis of local mobility is by deformable registration, which stands for the mapping of different time steps onto each other [66-69].

3.3.1 MRI Lung Segmentation

Despite the above mentioned techniques for assessment of lung function and local mobility, another method to calculate this information is from segmentation of the lung surface over the breathing cycle. As dynamic imaging of the lung with the help of 3D+t MRI sequences is a relatively new field of research, not many publications exist on this topic.

A workflow for regional lung perfusion assessment based on slice-wise semi-automatic region growing was presented by [70], which was later enhanced by the use of deformable simplex meshes [71]. Here, a user can define attracting points in the original image data. The mesh deformation algorithm guarantees that the surface model will pass through these interactively set points. Thereby, the user can influence the evolution of the deformable model and gets direct feedback during the segmentation process.

With the help of contrast agent and 2D imaging or during breath-hold, it is sometimes possible to simply segment the lung tissue by the application of a threshold [72-74], or by region growing guided by confidence-connectedness and fuzzy-connectedness filters [75].

A more sophisticated approach merges active contours to capture lung border contours in contrast agent enhanced 3D MRI images [76]. These contours are applied on 2D slices of the image and are afterwards merged to a 3D surface by a guiding force based on the Navier-Stokes equation of fluid dynamics.

Another work based on 2D active contours is presented by [77]. They add an additional region force to the standard gray value gra-

dient force that is driving the snake to incorporate global boundary information, thus helping to detect fuzzy boundaries.

Drawback for all of these methods is that they are 2D-based, depend on contrast agent enhanced image acquisition, or require an extensive user interaction.

3.4 Interactive Model Correction

The segmentation of relevant structures in medical images is nowadays, due to the steadily increasing computational power, a task which can increasingly be done automated. But still segmentation is a complicated and error-prone task even to human specialists, and is especially on low-resolution volumes or data showing strong anatomical variations a challenge for automated computer applications. Many segmentation frameworks tend to allow user interaction only at the beginning to initialize the algorithm, and do not offer a possibility to subsequently correct the segmentation result. Therefore, to ensure the validity of segmentation, the user must be given a possibility to interact with the computer system during or after the segmentation. Many types of interaction are possible, as e.g. summarized in [78] or, more recently, [79]. These methods include interventional methods used during the segmentation process, like the response to feedback data or continuously steering of the process. And methods working on the final result, like changing parameters and repeating the segmentation process [79]. Often found examples for model based segmentation are to force landmarks to user set positions (see e.g. [80]), or the introduction of a force according to a user interaction, working on the model during the segmentation process in a predefined pattern (see e.g. [81]).

4 Methods

In this chapter, the developed methods for segmentation of moving organs as well as the generation of diagnostic parameters from the results are described. Firstly, an overview of the deformable shape model is given, which is basis for the coupled shape model segmentation used in this thesis. Secondly, the calculation of medical relevant parameters for restrictive diseases of the heart (section 2.2) and the lung (section 2.8) are explained in detail.

4.1 Deformable Shape Model

This section gives details on the theory of statistical shape modeling and on the deformable model [82] that was used as basis of multiple organ segmentation.

4.1.1 Shape

Per definition, the shape of an object located in some space is the part of that space occupied by the object, as determined by its external boundary. It is the abstraction from other properties such as color, content, and material composition, and, for the means of statistical shape modeling of especial importance, the object's other spatial properties: position, orientation in space, and scale.

There are different methods to describe a shape in space. While in 2D it is often possible to describe a shape by basic geometry, like with lines, curves, planes and so on, this gets impossible in most instances in 3D, especially for complex objects like organs, as they appear in medical problems. Therefore, several methods have been established to describe the 3D shape of an object approximately. Examples are moment based descriptors, spherical harmonics, graph based descriptors like M-reps or a landmark based description. Each method targets different aspects of shape and can be used for a specific application. As in this thesis the focus is on capturing intra-object variabilities and inter-object correlations, a land-

mark-based description was applied as it best captures the features of interest (see section 4.1.3).

4.1.2 Statistical Variability of Shape

Since their introduction by Cootes et al. [83], several fundamental extensions and improvements on the construction of statistical shape models have been presented. The underlying key concept of modeling the shape variability of a certain object class subject to statistical variability is still the same, however. Consider a shape $\sigma \in \mathbb{R}^d, d \in \mathbb{N}$ showing distinct shape characteristics of the particular object of interest, thus constituting an instance of the object class. Given a set of $n_t \in \mathbb{N}$ of such shapes, $\{\sigma_i \mid i = 1,...,n_t\}$, they can be seen as a data basis to differentiate shape features of the object class that appear more likely than others. An approach to capture the entirety of these differences is therefore to construct a model that is capable of representing the statistical variability of the object's shape which can be observed across the set of shapes σ_i. This model is called statistical shape model (SSM), the set of shapes are named training samples, since they have been used to "train" the model in such as integrating a priori knowledge into it. The next two sections provide the fundamentals necessary for the construction of a SSM. First, an appropriate mathematical description of shape representation is given. Then, the shapes have to be embedded in a common coordinate frame to allow capturing the observed shape variability into the model.

4.1.3 Shape Representation

Training data in most cases consists of segmented volumetric images in the medical field, given as an overlay of binary voxel data. From the voxel data, the contour of the objects of interest can be extracted, e.g. by the Marching Cubes algorithm [84], and an intuitive representation of this contour is a distribution of points across it. Given a set of training samples $\{\sigma_i\}$, each of them is sampled along its boundary (=contour in 2D, surface in 3D) using $n_l \in \mathbb{N}$ points $x_{i(j)} \in \sigma_i, j = 1,...,n_l$. These points are often referred to as *landmarks*, as they usually represent prominent features of the shape. Landmark representation provides the simplest and at the

same time the most generic method used to represent shapes, which makes it easy to deal with multiple models simultaneously. Any point can be represented by a tuple of Cartesian coordinates $\left(x_{i(j)}^{1},...,x_{i(j)}^{d}\right) \in \mathbb{R}^{d}$. Therefore, each shape σ_i can be represented by means of its associated shape vector x_i:

$$\sigma_i \Rightarrow x_i = (x_{i(1)}^{1},...,x_{i(1)}^{d},...,x_{i(n_l)}^{1},...,x_{i(n_l)}^{d}) \in \mathbb{R}^{dn_l} \qquad (4.1)$$

As in this thesis the models will be restricted to shapes embedded in three-dimensional space, the j-th sample point of the i-th shape $\sigma_i \subset \mathbb{R}^3$ can be represented by the tuple $\left(x_{i(j)}, y_{i(j)}, z_{i(j)}\right)$, thus the shape vector (4.1) simplifies to

$$x_i = (x_{i(1)}, y_{i(1)}, z_{i(1)},...,x_{i(n_l)}, y_{i(n_l)}, z_{i(n_l)}) \in \mathbb{R}^{3n_l} \qquad (4.2)$$

This representation of a shape by surface landmarks is commonly referred to as point distribution model (PDM) [83, 85]. Additionally, the connectivity information between the landmarks can be stored in form of a triangle mesh, which allows the reconstruction of a surface during and after segmentation.

4.1.4 Shape Space

The set of shape vectors $\{x_i \mid i = 1,...,n_t\}$ spans a dn_l-dimensional space $\Sigma \subset \mathbb{R}^{dn_l}$. Accordingly, any shape σ_i is represented by a single dn_l-dimensional point $x_i \in \Sigma$. Anyhow, not every point $x \in \Sigma$ is a valid instance for representation of the object class.

The space that integrates the set of all feasible shapes is the so-called shape space [86]. Following the definition of shape given previously this space does contain the Procrustes aligned shapes. According to this, the shape space is a hypersphere Ω^{dn_l} on the surface of which the size normalized landmark representations $\{x_i\}$ are located. An important aspect is that the submanifold Ω^{dn_l} of Σ is curved, which may result in considerable non-linearities of the shape variation.

The tangent space alignment [86] (Fig. 4.1) removes this non-linearity and thus allows for modeling the shape variability using a linear model. Given the mean shape

$$\bar{x} = \frac{1}{n_s}\sum_{i=1}^{n_s} x_i \tag{4.3}$$

the tangent space of $\bar{x}$ is the hyperplane that contains all vectors normal to $\bar{x}$ passing through $\bar{x}$ [87]. The shapes are projected into the tangent space by scaling them with the inverse of the length of x_i when projected onto $\bar{x}$, thus $x_i = x_i / \langle x_i, \bar{x} \rangle$. Here, $\langle .,. \rangle$ denotes the inner product.

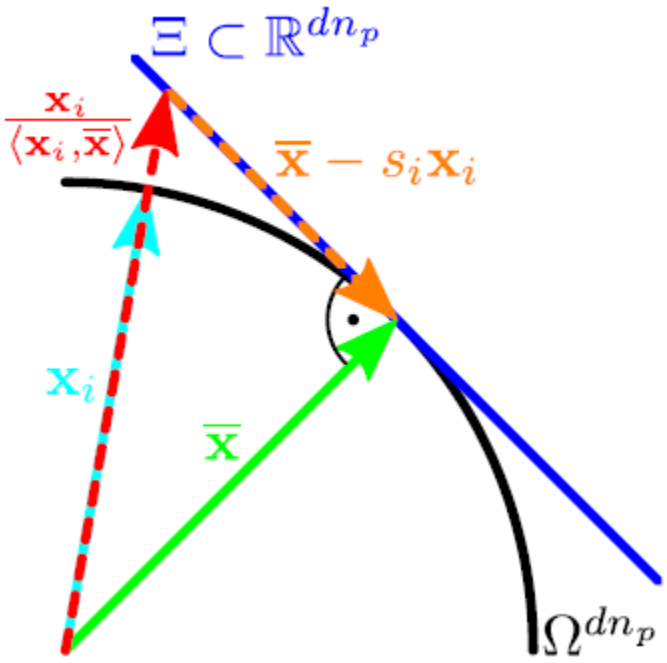

Fig. 4.1 Tangent space construction

Scaling projects the normalized shape vector x_i into the tangent space of the mean shape $\bar{x}$, where $(\bar{x} - s_i x_i) \cdot \bar{x} = 0$

4.1.5 Shape Model Construction

As shape is per definition invariant to similarity transformations, these transformations have to be removed from the training data first to capture the shape space. This is done by aligning all training data in a common coordinate frame. A standard procedure for doing this is the generalized Procrustes alignment (GPA) which minimizes the mean squared distance between two shapes and can be calculated analytically [88, 89]. The algorithm iteratively aligns a group of shapes to their unknown mean.

Anyhow, the landmarks the training data consists of still do not correspond to each other. To make a statistical analysis of variation, landmarks on all training samples have to be on corresponding anatomical positions. Due to the large number of landmarks and the fact that correspondences have to be found in three-dimensional space, only automatic methods are of practical relevance. Therefore, a landmark correspondence optimization as described in [90] is utilized here.

After alignment and correspondence generation, assuming the training samples represent a unimodal, multivariate Gaussian distribution in shape space, the next step is to reduce dimensionality of the training set. Aim is to determine a small set of modes that best describe the major directions and respective intervals of valid movement (i.e. the observed variations). This can be done by means of *principal component analysis* (PCA) [91]. Given the mean shape as from equation (4.3), the corresponding covariance matrix C is given by

$$C = \frac{1}{n_t - 1} \sum_{i=1}^{n_t} (x_i - \bar{x})^T (x_i - \bar{x}) \qquad (4.4)$$

An eigenvalue decomposition of C now results in its modes of variation p_m and their variances λ_m.

As PCA is known to be numerically susceptible to ill-posed problems, a more stable and therefore mostly preferred way to obtain variances is singular value decomposition (SVD) [92] on the aligned landmark matrix L:

$$L = \begin{bmatrix} x_1 - \overline{x} \\ \dots \\ x_{n_t} - \overline{x} \end{bmatrix} \tag{4.5}$$

$$\frac{1}{\sqrt{n_t - 1}} L = U \Sigma V^* \tag{4.6}$$

Here, Σ is a $n_t \times n_l$ dimensional matrix holding the singular values $\{\sigma_m\}$ of L in its main diagonal, which are equal to the square root of variances $\{\lambda_m\}$. The right singular vectors $\{v_m\}$ of V equal the principal components of the covariance matrix $C = L^T L$.

With the knowledge of the principal components and their variances, any valid shape can be represented as a linear combination of principal components

$$\begin{aligned} & x = \overline{x} + \sum_{m=1}^{n_t - 1} y_m p_m \\ & with \left\{ y_m \in \mathbb{R}, -\lambda_m \le y_m \le \lambda_m \,\middle|\, m = 1 \dots M \right\} \end{aligned} \tag{4.7}$$

Normally, to reduce dimensionality, only the strongest modes of variation are really used. Using the SVD generated eigenvalues ordered by their weighting, taking the strongest n_m modes into account leads to:

$$x \cong \overline{x} + \sum_{m=1}^{n_m} y_m p_m \tag{4.8}$$

Thereby, any valid shape of an object of the same type as the training data can be approximated by a mean shape $\overline{x}$ and its statistical modes of shape variation p_m and is described by a number of n_m parameters y_m. It is important to choose n_m in a way that a large percentage of variation is captured, but dimensionality is reduced sufficiently to keep calculation time low.

4.2 Model Search

This chapter describes how the trained model of shape can be used to detect valid shapes in new image data. First the idea of how to train the appearance of an object in image data is explained, and then the algorithm to detect objects iteratively driven by internal model forces and external image forces is depicted.

4.2.1 Local Appearance Model

To redetect the modeled shape in unseen image data, an additional model of the local gray-value appearance around the boundary is necessary. This model of appearance can be extracted from the training data as well. Similar to the shape training, an appearance model should describe the mean appearance (e.g. gray value or gradient) for each landmark and its surroundings as well as their variations. It is called a local appearance model, as it does not describe the global appearance of the shape, but the regional gray value distribution around the single landmarks. A commonly used method in segmentation with deformable models is to sample profiles g_{it} perpendicular to the surface at each landmark i in all training images t. Mean profiles $\overline{g}_i$ and the modes of variation for each landmark can then be determined as described above via PCA or SVD, independent of the feature which is used to describe appearance.

Two different approaches of appearance models are used for the tasks given in this thesis. For the segmentation of the lungs, as their borders are relatively obvious in bigger parts of the images, a normalized gradient profile can be used to sample appearance. The a priori knowledge incorporated hereby is simply that the highest local gray value gradient is at the position of the object border. As the heart ventricles border is much more diffuse, an alternative approach based on kNN classifiers [93] is used. Hereby, in addition to the profiles g_{it}, a number of shifted profiles (i.e. translated towards the inside and outside of the object) are sampled. The set of training data thereby consists of three classes, inside, outside, and boundary. The probability $p(b \mid g)$ of a profile lying on the object boundary can therefore be estimated by querying the k nearest neighbors to g and calculating the ratio of true profiles b_{true} among

them. A moderated kNN-classifier [94] is used to prevent zero possibilities, giving:

$$p(b \mid g) = \frac{b_{true} + 2}{k + 1} \tag{4.9}$$

With a limited number of training images available, for both methods a landmark clustering can increase the amount of training data. A k-Means clustering is used to group appearance profiles of similar landmarks together [95].

4.2.2 Search Algorithm

Once a rough initial transform for the SSM is determined by manual or automatic placement, a local optimization algorithm adapts the model further to the data and delivers the final segmentation. Basis is a deformable surface model defined as a triangulated mesh M = (V, E) with vertices $p, q \in V$ and edges $[p, q] \in E$. M has the same topology as the associated statistical shape model, where for each vertex p in the mesh, there is a corresponding vertex p' in the SSM. The evolution of the deformable model is controlled in a Lagrangian equation of motion fashion: at every vertex p_i, a regularizing internal force $F_{\text{int}}(p_i)$ and an image data driven external force $F_{ext}(p_i)$ are applied iteratively. Details on the used force terms in particular can be found in [96].

In discrete form, this can be written as:

$$p_i^{t+1} = p_i^t + F_{\text{int}}(p_i^t) + F_{ext}(p_i^t) \tag{4.10}$$

This way, the default segmentation pipeline of a SSM works as follows: in each iteration, the appearance model generates the momentary possible best adjustment for each landmark from the image data. For these adjustments, the closest possible valid representation in shape space is determined by solving equation (4.8) for the parameter vector y_m and used as restriction for landmark displacement (Fig. 4.2). In this case, the result mesh is not stringently constricted to valid shape representations, but is allowed a confined free deformation regulated by internal tension and rigidity forces, keeping the mesh similar to the underlying model. Also, an addi-

tional optimal surface detection step is applied to determine globally optimal displacements in matters of surface smoothness [96]. To increase both segmentation speed and accuracy, the model search is applied hierarchically on four resolutions of a beforehand calculated Gaussian image pyramid, from coarse to fine resolution, until a convergence criteria for the particular resolution is met, which can be the maximal average landmark movement falling below a defined value, or a fixed number of steps. Therefore, in problematic image areas, a shape model performs an “educated guess” of the local shape from the landmark distribution outside of this area due to the shape restriction term.

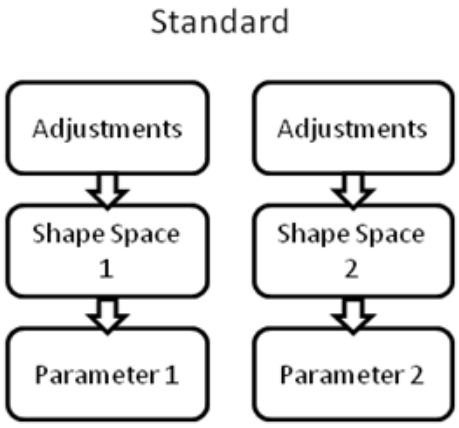

Fig. 4.2 Segmentation scheme for two objects using single deformable models.

4.3 Coupled Models

In the observed cases of self-moving organs, namely the epicardium and endocardium of the left ventricle and the both lungs, the objects of interest to be segmented are highly correlated in their temporal movement behavior. This correlation can be exploited to gain multiple additional information which can be used to greatly increase segmentation quality in difficult image areas, by using correlation information of other objects to increase local information of the problematic ones.

This section describes the methods developed to use coupling information to initialize models from others, and to facilitate correlation information during the shape model search.

4.3.1 Model Initialization

A common problem in shape based segmentation is that an initial model is needed which is located at least nearby the structure of interest and should only differ from it in size and orientation in a reasonable magnitude. This initial model geometry has to be determined either by automatic methods based on image features (e.g. [97],[98],[99]), or by user interaction.

An additional difficulty when analyzing 3D+t MRI images is on the one hand that the acquisition field of view (FOV) is freely selectable based on the experience of the physician. For the heart, normally it is centered on the heart and oriented along the short heart axis. For the lungs, it is normally oriented parallel to the standard transversal, coronal, and sagittal views, but not necessarily centered in the lungs center of mass. Sometimes it is not even possible to fit both lungs in inhaled state completely inside the scanner's FOV. The resulting greatly varying image geometries make it difficult to automatically find starting points.

On the other hand, the low image resolution and signal-to-noise ratio in time resolved MRI make it very difficult to find landmark based features for model initialization.

Because of these difficulties, a semi-automatic approach based on statistical geometry has been chosen for this work. The idea behind the method is that in a multi-object complex, if the position, size and orientation of one object are given, these transformations can directly be estimated for all other objects in the complex based on inter-object geometrical statistics. As training data is necessary for the construction of the model anyway, geometrical inter-object relationships can be extracted directly from the training data.

So after a first model is placed by a short user interaction, all other models can be automatically by:

$$\begin{aligned} &\vec{x}_n = \overline{A} \cdot \vec{x}_1 + \overline{(\vec{x}_1, \vec{x}_n)}, with \\ &\overline{(\vec{x}_1, \vec{x}_n)} = \frac{1}{n_T} \sum_{i=0}^{n_T-1} \vec{t}(\vec{x}_{1,i}) - \vec{t}(\vec{x}_{n,i}) \\ &\overline{A} = \frac{1}{n_T} \sum_{i=0}^{n_T-1} \overline{\measuredangle(A_{1,i}, A_{n,i})} \cdot \frac{s_{1,i}}{s_{n,i}} \end{aligned} \qquad (4.11)$$

Here, $\vec{t}(\vec{x})$ refers to the translation of model $\vec{x}$, $\overline{A}$ refers to the rotation matrix including scale s, and the index n to the number of model to be initialized from model 1. The index i refers to the training samples, which have to correspond, for sure (all objects have to be delineated in the same original image). The term $\overline{\measuredangle(A_{1,i}, A_{n,i})}$ denotes the normalized Euler angle between orientation of x_1 and x_n.

For the application on the epi- and endocardium as well as both lungs the rotation term is not used, as in both cases both objects are assumed to have very similar orientations, so the matrix $\overline{A}$ is orthogonal and simply does a rescaling.

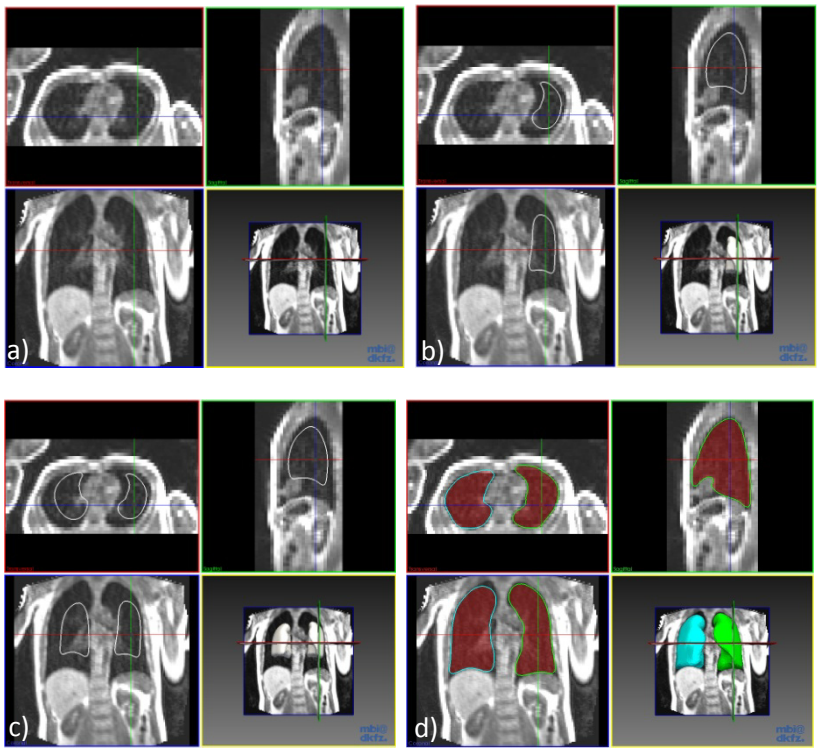

Fig. 4.3 Example of automatic model initialization

a) Original image. b) The first model is roughly placed manually from a starting position. c) The second model is placed automatically based on statistical geometrical correlation to the first model. d) Segmentation result.

4.3.2 Shape Space Coupling

Simultaneous multi-object segmentation is an important direction of research, since in many applications the objects to be segmented are often highly correlated. This information can be used to impose further constraints on the boundary estimation problem.

So, when examining multiple objects of interest in image data, additional information beyond the shape and appearance of the single entities can be taken into account. Of great interest hereby are correlations in inter-object shape variability. These correlations can originate from a couple of causes:

- Common physiology, e.g. the left and right lung
- Mutual physical linkage, e.g. the endocardium and epicardium of the left ventricle
- Neighborhood relations, e.g. organs that are adjoining or close to each other
- Common pathology, e.g. alteration in related brain structures in certain diseases

This section presents two methods to further increase local information of models by taking mutual shape information into account, and two different ways to apply this information as an additionally force term in the shape model search equation.

4.3.3 Joint Shape Space

Having multiple objects of interest present in the same training data sets, these can be treated as one complex. A prerequisite is that they have corresponding landmarks over all training data in each case.

Given these correspondences, for the first method, called joint shape space, corresponding landmarks of multiple objects in each training data are joined together and are treated as a single entity of a multi-object complex. For e.g. two objects k and l, this can be represented as

$$\begin{aligned} x_{k,l} = (&x_{k(1)}, y_{k(1)}, z_{k(1)}, \ldots, x_{k(n_l(k))}, y_{k(n_l(k))}, z_{k(n_l(k))}, \\ &x_{l(1)}, y_{l(1)}, z_{l(1)}, \ldots, x_{l(n_l(l))}, y_{l(n_l(l))}, z_{l(n_l(l))}) \end{aligned} \tag{4.12}$$

With the help of singular value decomposition as described in section 4.1.5, the mean shape and shape variability of the multi-object complex can be trained. A joint shape space $\Sigma_{k,l} \subseteq \mathbb{R}^{n_t-1}$ can be derived from these, which also describes inter-object shape variation dependencies. Here, n_t denotes the number of training samples.

4.3.4 Unified Shape Space

The other idea to incorporate inter-object shape information is based on the calculation of a unified shape space after training of the single models. This does not implicitly generate inter-object shape dependencies, but can be helpful if objects are assumed to have strongly correlated modes of variation, e.g. the endocardium and epicardium of the heart over the heart cycle. Having two models with positively correlated modes of shape variation, i.e. their strongest variation eigenvectors don't differ too much in direction, determination of optimal shape parameters can be done in a common shape space to direct the models towards a similar state of shape during search. The unified shape space can be calculated as:

$$\begin{aligned}\Sigma^*_{k,l} &= [span(u_1,...,u_k,v_1,...,v_l) | u_i \in \Sigma_k, v_i \in \Sigma_l] \\ &\subset (\Sigma_k \times \Sigma_l) \subseteq \mathbb{R}^{nTS-1}\end{aligned} \tag{4.13}$$

Here, Σ^k denotes the shape space of the first shape model with dimensionality k, Σ^l the second shape space with dimensionality l. Please note that $(u_1,...,u_k,v_1,...,v_l)$ does not form a basis of $\Sigma^{k,l}$ in general, but can easily be reduced to one. $\Sigma^*_{k,l}$ is called unified shape space here to distinguish it from joint shape space, although the meanings are synonym.

To obtain common shape parameters then, an adjusted version of equation (4.7) has to be solved:

$$\begin{aligned}\vec{b}_{k,l} &= \begin{bmatrix}(\vec{x}_k - \overline{x}_k) \\ (\vec{x}_l - \overline{x}_l)\end{bmatrix} = \vec{y}_m \, \Sigma^*_{k,l} \\ \Rightarrow \vec{y}_m &= (\Sigma^{*\mathbf{T}}_{k,l} \, \Sigma^*_{k,l})^{-1} \, \Sigma^{*\mathbf{T}}_{k,l} \, \vec{b}_{k,l}\end{aligned} \tag{4.14}$$

4.3.5 Shape Parameter application

For both above methods, the additional mutual information can be seen as a supplementary regulatory force steering each model by means of the shape of the others. The coupling force term tries to optimize shape parameters regarding the current shape of all models. Therefore the coupling forces compete with the internal forces of the single models which try to generate optimal shape of the single entity.

For the common shape space method, only one set of common shape parameters is obtained for all single models. For the joint shape space method, each model receives an individual set of parameters. But, in both cases, the landmark distribution generated by these parameters does not have to be a valid representation inside of the shape space of the particular object.

Therefore, two possibilities to attribute common shape parameters back to the single models have been evaluated:

- Strict: Directly set the calculated shape parameters to all models, regardless of the single models shape space (Fig. 4.4).
- Relaxed: Calculate the target landmark coordinates that would result from the common parameters for each of the models, and then find the closest valid representation in the model's individual shape spaces for these adjustments (see Fig. 4.5).

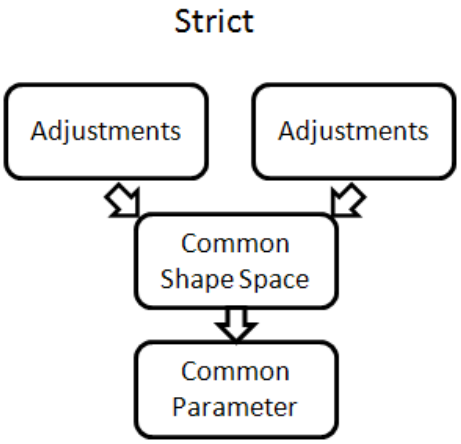

Fig. 4.4 Segmentation workflow for strict parameter application

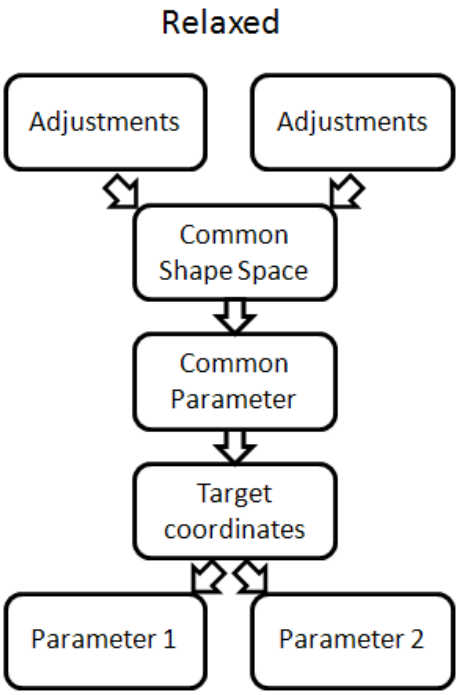

Fig. 4.5 Segmentation workflow for relaxed parameter application

The segmentation framework depicted in Fig. 4.4 and Fig. 4.5 is displayed for two models, but can also be applied to any number of correlated models.

These additional gained coupling parameters can be interpreted as an additional internal force term in the shape model search equation (4.10), extending it to

$$p_i^{t+1} = p_i^t + (\alpha F_{\text{int}}(p_i^t) + \beta F_{coupl}(p_i^t)) + \gamma F_{ext}(p_i^t) \qquad (4.15)$$

where F_{coupl} is the force term originating from the common strict or relaxed shape parameters, α and β are parameters to set the weighting between the influence of single model shape forces and forces derived from coupling.

In all cases, the evolution of the models is started from a manually indicated position in a multi-resolution fashion on a three times down-sampled version of the image. After a previously fixed average landmark displacement is under-run, resolution is changed to a finer version of the image. In case of the newly proposed methods, segmentation is done simultaneously, in case of the standard approach subsequently.

4.3.6 Geometrical Coupling

Besides the mutual knowledge of shape information, also geometrical information can be used to obtain better segmentation results in difficult image regions. Neighboring objects usually exhibit strong mutual spatial dependencies. In segmentation with statistical shape models, a lack of precision due to the restriction on trained shapes is generally a problem, as previously unknown patient anatomy cannot be contained in the model. While this lack is overcome by the above describe admission of an image driven free deformation, this can lead to inaccuracies due to the loss of shape knowledge, especially when objects to be segmented cannot clearly be distinguished from adjacent structures. When objects of interest lie close together or adjoin each other, this may especially lead to overlapping segmentation results.

A basic idea for further improving segmentation results and simultaneously solving the overlap problem is to segment multiple adjacent structures at the same time and apply some a priori knowledge about their spatial relationship.

When spatial constraints between multiple objects are available, such information can be used to set up an additional force term in the shape model search equation which penalizes invalid spatial relationships. The relative arrangements among these neighbors can

be modeled by obtaining statistical information on the objects geometry from training sets again.

To deform multiple models with adaptive special constraints simultaneously, a cost function has been constructed to modulate external forces at each vertex. For each vertex v of the k-th model, the mean Euclidian distance to all other models can be calculated as

$$\begin{aligned} &\bar{d}_k = \frac{1}{n_{TS}} \sum_{i=0}^{n_{TS}-1} d_v, \\ &with\ d_v = \left\{ \min(\left| \Phi_{M_j} \right|), \forall j \neq k \right\} \end{aligned} \tag{4.16}$$

where Φ_{M_j} is the signed distance transform of the j-th model M_j, and n_{TS} is the number of training samples. With this, a cost function that modulates external forces at each vertex v can be defined as

$$\begin{aligned} &c_D(d_v) = \frac{2}{\pi} \cdot \left| \arctan(\frac{d_v - \bar{d}_k}{2 * \sigma(d_v, \bar{d}_k)}) \right|, \\ &with\ \sigma(d_v, \bar{d}_k) = \sqrt{\frac{1}{n_{TS} - 1} \sum_{i=0}^{n_{TS}-1} (d_v - \bar{d}_k)^2} \end{aligned} \tag{4.17}$$

The resulting function is shown in Fig. 4.6. The function is designed to be normalized to a $[0,1]$ interval, and rises to 0.5 at two standard deviation $\sigma(d_v, \bar{d}_k)$ difference from the mean. A function with a steep slope around zero was chosen to deal with overlapping of adjacent objects, as these show low deviations (they should be close to zero in all training data), but should be penalized still for small deviations from zero.

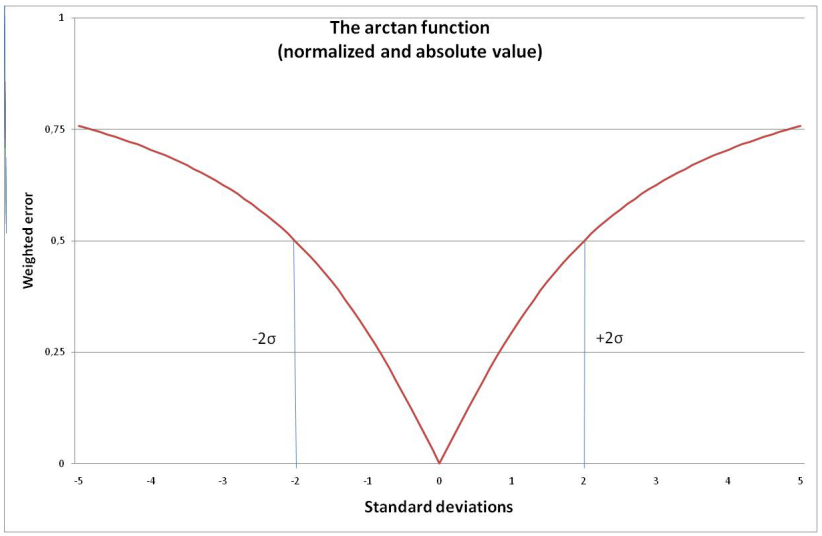

Fig. 4.6 Cost function for geometrical coupling

Shown is $\frac{2}{\pi}\left|\arctan(\frac{x}{2\sigma})\right|$, where x is a distance error in size of standard deviations σ.

With the help of this cost function, at each vertex of a mesh a force term can be defined as

$$F_{geo}(d_v) = c_D(d_v) \cdot (\overrightarrow{v_j(d_v), v_k(d_v)}) \cdot sign(d_v - \overline{d}_k) \qquad (4.18)$$

This force term drives each vertex v_j away or ahead to its nearest neighbor on the other model v_k depending on the direction of the error $sign(d_v - \overline{d}_k)$, leading to a total force equation of

$$p_i^{t+1} = p_i^t + \alpha F_{\text{int}}(p_i^t) + \beta F_{coupl}(p_i^t) + \gamma F_{ext}(p_i^t) + \delta F_{geo}(p_i^t) \quad (4.19)$$

4.4 Summary of Model Search

To give a short overview over the complete segmentation process, the following list presents the steps done for segmentation in summary.

- Manually initialize first model
- Automatically initialize all other models
- Initialize common shape and geometrical information

- Evaluate appearance profiles, calculate external forces, calculate landmark adjustments
- Restrict adjustments to trained shapes by internal forces (degree of restriction (stiffness) is decreased over process)
- Apply optimal landmark detection (ensures surface smoothness)
- Apply common shape information
- Apply geometrical restrictions
- Repeat steps 4-8 until a convergence criteria $\sum_i \left| p_i^{t+1} - p_i^t \right| < \delta$ is met, or until a maximal number of steps

4.5 Interactive Correction

The above described model approach used for automated segmentation showed very good results in almost all cases of segmentation. In the proposed diagnostic applications of the left ventricle and the lung, anyhow, in some cases the segmentation differed significantly from the provided ground truths.

- For the left ventricle, the segmentation sometimes leaked into the atrium or the aorta, as the mitral and aortic valves separating them from the LV are not visible in MR images.
- For the lung lobes, the model generally had problems to completely segment the lower tips of the lung over the diaphragm.

Therefore, an interaction possibility has been integrated into the segmentation framework to allow the user to quickly and efficiently correct erroneous segmentations. A manual correction using a Gaussian pattern was chosen, working on the result of the automated segmentation. The resulting mesh is deformed directly, and the underlying model is used to keep the mesh consistent after the deformation. The tool allows the user to pick a center landmark μ (at position $\vec{\mu}$) on the resulting mesh, and drag it with the mouse to a new position $\vec{\mu}'$. The user is not required to accurately hit a mesh point; the point on the mesh closest to the mouse click position is automatically selected. Landmarks r in the surrounding of $\vec{\mu}$ with distance $d(\vec{r}) = \left| \vec{r} - \vec{\mu} \right|$ up to a maximal distance $d_{\max}$ are moved along in form of a Gaussian normal distribution. The maximal distance (i.e. radius of interaction around the point) can be interactive-

ly set by the user through the GUI. For speed reasons, all points affected by the interaction, i.e. $d(\vec{r}) \leq d_{\max}$, are stored in a list via breadth-first search when an interaction point is picked, so they are available until the interaction is finished for that point. This is useful for live display of the mesh deformation, and also if the user wants to move the point several times or undo his changes. Additionally, as it has shown convenient in radiological practice, the standard deviation σ of the normal distribution is depending on the interaction radius $d_{\max}$ exponentially:

$$\sigma(d_{\max}) = \alpha^{d_{\max}} \tag{4.20}$$

This exponential dependence means in practice that the normal distribution gets very steep for small interaction radii, allowing the user to draw "spikes" out of the surface (small σ), and flattens quite fast for increasing radii (big σ). The parameter α determines how fast the steepness decreases with $d_{\max}$ and was chosen 1.25.

Putting all together, this leads to a displacement of the form:

$$v(d) = v_0 \cdot e^{-\frac{1}{2}\left(\frac{d}{\sigma(d_{\max})}\right)^2} \tag{4.21}$$

where $v_0 = \vec{\mu}' - \vec{\mu}$ describes the vector the picked point is moved (Fig. 1 and 2). Therefore, each single point within the interaction radius is moved to a new position $\vec{r}'$:

$$\vec{r}' = \vec{r} + v(d(\vec{r})) \tag{4.22}$$

After the interaction is finished, the model is updated once more on the lowest level of detail to adjust the shape parameters and smoothness conditions to the new shape as good as possible. Because of this additional update the user only has to approximate the surface deformation to the desired image area, and usually the algorithm will then find the correct position.

The framework for multiple coupled organ segmentation and interactive correction has been integrated into a segmentation routine of the medical imaging interaction toolkit MITK [100], which again can be integrated as a Plug-in for the teleradiological reporting worksta-

tion Chili® [101]. An example of the graphical user interface (GUI) is shown in Fig. 4.9.

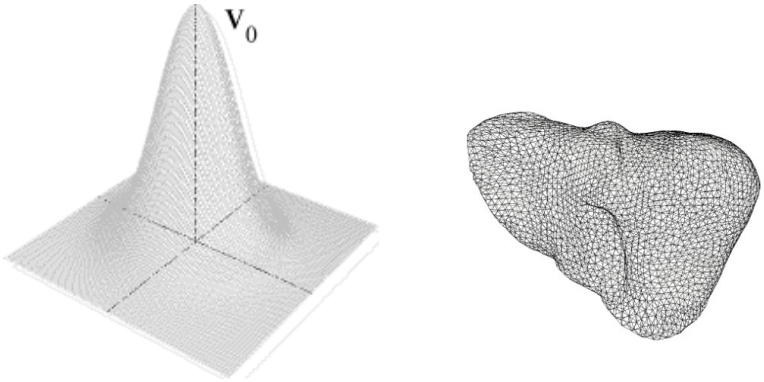

Fig. 4.7 Deformation basics

Left: Gaussian normal distribution in 3D. Right: An exemplary mesh grid model of a human liver.

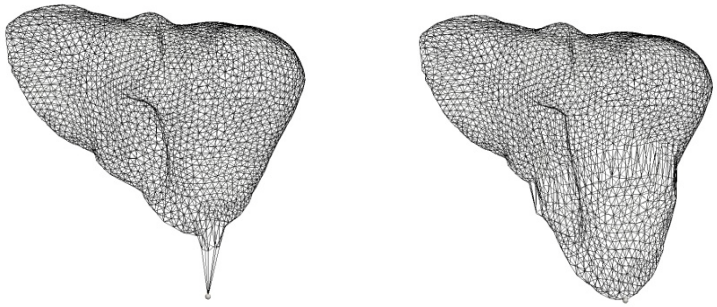

Fig. 4.8 Deformation possibilities

Left: The model from Fig. 4.7 (right), deformed only in a single point. Right: The same model, deformed in a large area. The small grey sphere marks the interaction point.

Fig. 4.9 The segmentation and interaction GUI, integrated in the teleradiological reporting workstation Chili®.

4.6 Quantitative Analysis of Cardiac Motion

The result of the segmentation of the epi- and endocardium can inherently display wall motion by color encoded landmark displacement visualization (Fig. 4.10). Although this display can be viewed as a video of cardiac motion over the complete heart cycle and gives a good overview of global 3D+t movement and restrictions, it not clearly represented enough to provide a quantitative analysis of cardiac diagnostic parameters. It is also not very suited for the display of parameters like local wall thickness or thickening. There exist several standardized methods to visualize these parameters quantitatively, most common in a so-called Bull's Eye diagram.

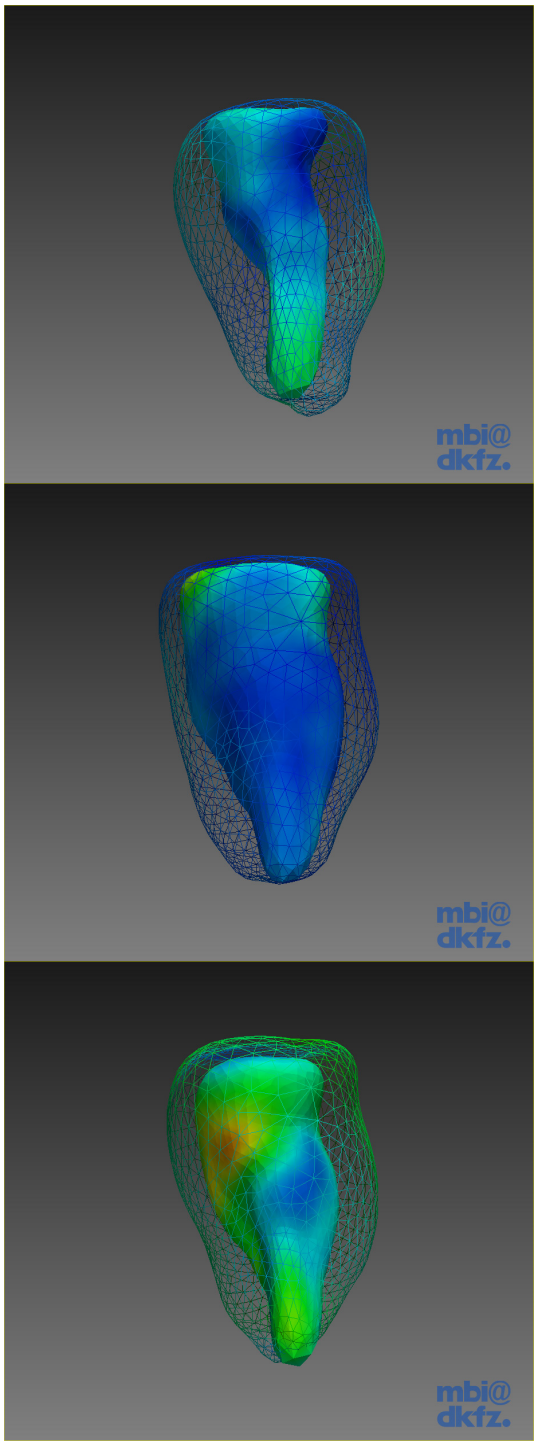

Fig. 4.10 Exemplary result of cardiac motion

The outer, wireframe mesh represents the epicardium, the inner, solid surface the endocardium. Local motion is color coded from red (high motion) to blue (low motion)

Therefore, details on how to extract heart physiological parameters from deformable model based segmentation are given in this section. The following subsections explain the structure of the Bull's Eye diagram, the projection from the segmentation result to the diagram and the visualization of the results.

4.7 Cardiac Diagnosis

4.7.1 Implementation of the Bull's Eye Diagram

The Bull's Eye diagram (see section 2.5 and 2.6) is implemented as 17 independent segments, each of which represented as a polygonal triangle mesh (Fig. 4.11). Each segment is defined by the parameters starting angle, end angle, upper radius, width, and resolution. The first four parameters define the geometrical properties of the segment, from which it is constructed according to the AHA standard (see section 2.6). Resolution regulates the number of vertices and thereby number of cells per segment.

Each vertex can be assigned an individual color value; the segment can then be colored according to a global lookup table. In addition, each segment is time resolved, i.e. allowing saving different color values per vertex for each time step.

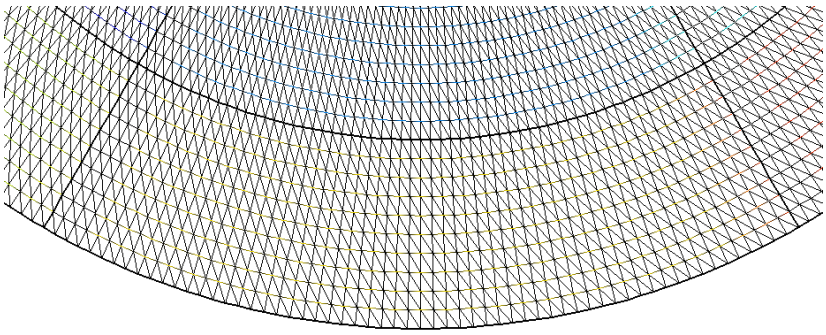

Fig. 4.11 Structure of a Bull's Eye segment

4.7.2 Projection

For the display of calculation results of the dynamic cardiac parameters wall motion, wall thickness, and wall thickening in the Bull's Eye diagram, a projection $\mathbb{R}^3 \rightarrow \mathbb{R}^2$ is necessary, in this case, from a three-dimensional surface resembling an undulated paraboloid to a

circular area (Fig. 4.12). As the heart's shape changes over the cardiac cycle, an analytical solution of this problem via a transformation equation is not easily possible. Also, as the surface is concave-convex, overlaps can occur, so two points of the surface could be projected to the same point in the diagram via a transformation. Another general problem is the relatively low number of anatomical landmarks of the 3D surface, whose movement information is needed for motion calculation.

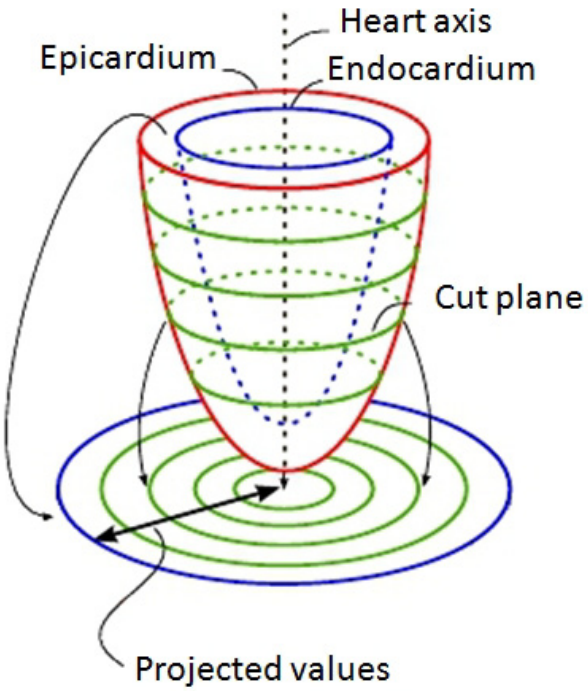

Fig. 4.12 Projection from heart ventricle to a 2D Bull's Eye diagram

Source: Adapted from [12]

Due to these problems, a strategy to reduce the 3D information into 2D was chosen, followed by interpolation. The reduction is conducted by a cutting of the 3D surface in a defined number of cut planes with normal vectors in direction of the longitudinal heart axis. The idea is shown schematically in Fig. 4.13, an example in Fig. 4.14. Result of each cutting is a circle-like polygon, whose vertices can be assigned to the Bull's Eye according to their angle to the zero line and to the height of the cut. Because the vertex density in the Bull's Eye is very much higher than the one from the cut planes, the closest point in the diagram can be chosen in the projection without

introducing significant errors. Afterwards, the remaining unfilled points in the diagram are linearly interpolated from their nearest neighbors to assure a continuous color gradient over the Bull's Eye.

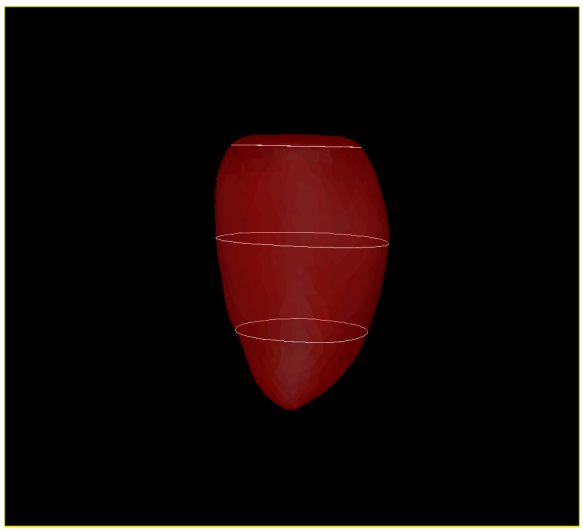

Fig. 4.13 Cut planes – schematic

First cut plae of the basal, mid, and apical segment.

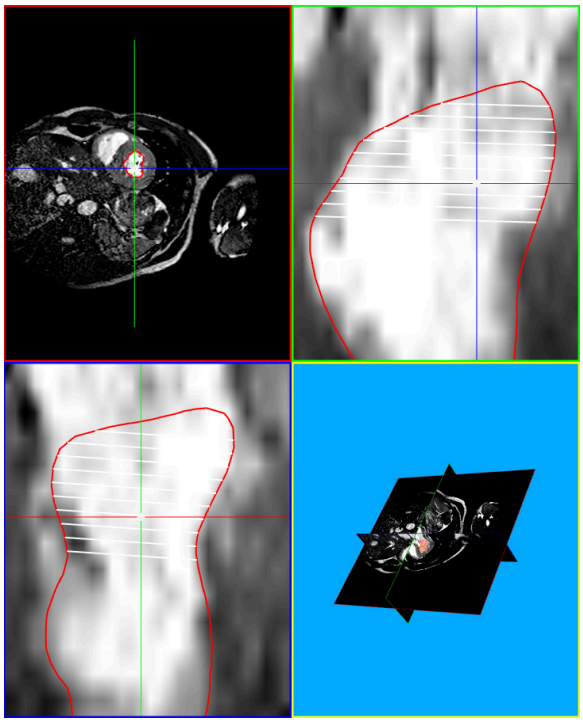

Fig. 4.14 Cut planes – example

Only basal segment cut planes are displayed

Necessary for the positioning of the cut planes is the longitudinal ventricle axis, which has to be calculated first. A first approach for its calculation is to create a binary image from the segmentation result, and do a principal component analysis (PCA) on it. The resulting first eigenvector is always near the long heart axis, besides cases of very strong heart deformations, where the method doesn't make sense anyways. This is because of the shape of the ventricle, resembling an undulated paraboloid. Anyhow, the found axis is in general not in agreement with the anatomical definition of the long heart axis, as the heart is no solid of revolution, so the axis does not run through the apex point. Thus, the deepest point of the mesh in caudal direction relative to the central point of the first eigenvector is located and considered as apex, according to the anatomical definition. It is assumed that there is always a mesh point at the apex due to landmark optimization (see section 4.1.5), as it shows high curvature. The upper point of the axis is considered the mesh vertex closest to the intersection point of the segmentation border and the first eigenvector. The longitudinal axis is then defined as the line connecting these two points. An example is shown in Fig. 4.15.

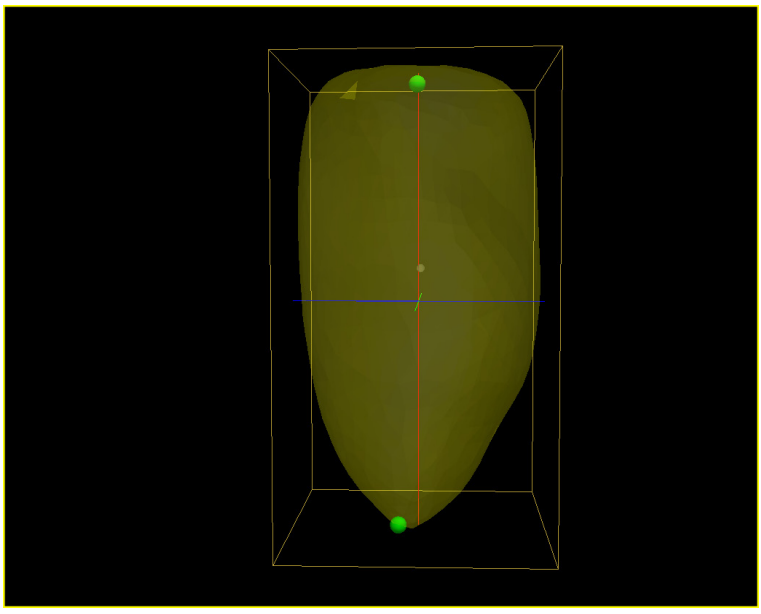

Fig. 4.15 Calculation of the longitudinal heart axis based on ventricular segmentation

The yellow box denotes the coordinate framework for the first eigenvectors of the surface; these are shown as red (first), blue (second), and green line (third eigenvector). The green dots show the calculated starting and ending points of the heart axis.

In the next step, the longitudinal heart axis is subdivided into three regions of equal size. Each region is further subdivided into n_R equidistant regions, which define the resolution of the Bull's Eye diagram. In this work, n_R was chosen 11. According to this division, the segmentation result mesh is cut by a plane with normal vector in direction of the longitudinal heart axis in each region. An example of this cutting is shown in Fig. 4.14 and Fig. 4.13. In the 3D display, one can see that the cuts of the planes with the surface result in circle-like polygonals.

In a further step, the single points of the polygonals are picked and their angle against the zero line is calculated. The zero line is defined as the vector from the center of the left ventricle towards the center of the right ventricle, which has to be manually set by placing a point in the myocardium between left and right ventricle. According to the calculated angle and the height of the cut plane against the apex, the color value of the polygonal point is transferred to the 2D diagram. Note that the apex point itself is not considered here, as the apex is defined as immobile.

Finally, after each value is transferred to the 2D diagram, the vertices of the diagram which do not already contain information are linearly interpolated over the values of their nearest neighbors. This concludes the projection from 3D to 2D space. To create a time resolved analysis, the above described procedure is repeated between each two consecutive time steps.

4.7.3 Parameter calculation

This section describes the realization of the extraction of quantitative cardiac diagnostic parameters as listed in section 2.4 from the segmentation results. The calculation of the volumetric parameters stroke volume, ejection fraction, cardiac output, cardiac index, and wall mass can directly calculated from the segmentation results of end-diastole and end-systole according to the formulas given in section 2.4. The dynamic parameters wall motion, wall thickness, and wall thickening are calculated as described below and are visualized in a Bull's Eye diagram as described in the last section.

Wall motion

Wall motion is defined as the endocardial movement over time. As segmentation is performed with the same endocardial model for all time steps over the heart cycle, landmark positions of the result directly correspond to anatomical positions in each time step. With this, wall motion can be calculated as the deformation vector field of the result landmarks between two time steps: For each landmark i at position p_{i,t_1} in time step t_1, the wall motion relative to a time step t_2 can be calculated as

$$WM_{i,t_1} = \left|(\overrightarrow{p_{i,t_2} - p_{i,t_1}})\right| \qquad (4.23)$$

This calculation is done between end-systolic and end-diastolic phase, which results in the total wall motion over the heart cycle, and for each consecutive time step, showing the temporally resolved local motion over the complete heart cycle. Both are displayed in a Bull's Eye diagram, in the second case, the diagram is temporally resolved, which means each time step has an independent diagram, besides the first, where no previous time step is given.

Wall Thickness

Wall thickness is defined as the distance between endocardium and epicardium at a given time. There exists a medical standard how this distance can be manually delineated in two perpendicular 2D planes [102]. Anyhow, as the segmentation result is present in 3D, the calculation was performed as closest distances between surface landmarks. For a landmark i at position p_i in time step t, this distance to another surface M_j can be calculated as

$$d_i = \min(\left|\Phi_{M_j}\right|) \qquad (4.24)$$

where Φ_{M_j} is the signed distance transform of M_j. This is not the mathematically closest distance between surfaces, where the distance vector should be normal to one surface and passing through a landmark of the other, but is much faster to calculate, and given a

sufficient landmark density, should only induce a small error. This will be further investigated in section 5.5.

Wall Thickening

Wall thickening can directly be calculated as the difference of local wall thicknesses between two time steps. Calculation can directly be done between the wall thickness Bull's Eye diagrams of two time steps to leave out the projection and interpolation steps. The error of wall thickening calculation is thereby directly dependent on the wall thickness calculation error. Again, the calculation can be done between end-systole and end-diastole to display the complete thickening over the heart cycle, or between all consecutive time steps to show temporally resolved thickening behavior.

4.8 Quantitative Analysis of Pulmonary Motion

4.8.1 Virtual Spirometry

Using up to date MRI sequences like FLASH-3D or TREAT, it is possible to acquire images of the complete thorax of the patient in one acquisition step, without radiation exposure of the patient. With this, a documentation of the breathing cycle with a temporal resolution of down to 0.5 seconds is possible, from which not only static parameters like vital capacity can be extracted, but even some of the dynamic respiratory parameters. Greatest advantage hereby is that parameters can be extracted separately for left and right lung. As most lung diseases only occur one-sided, techniques that measure air flow at the mouth like spirometry are not able to detect early stage diseases. As the air flow measured at the mouth always is the sum signal of both lungs, small changes in respiratory are difficult to monitor. A further aspect is that the not affected lung tends to compensate the missing respiratory volume of the diseased lung. Here, MRI gives the potential to quantify lung specific respiratory volumes and thereby help especially in early stage diagnosis and therapy monitoring.

To extract volumetric information from dynamic 3D+t image data, as workflow based on deformable shape model image segmentation was developed, with the help of which lung volumetry can be done

almost fully automatic. The process of MRI based lung volumetry is called *virtual spirometry*.

4.8.2 Extraction of quantitative Measures

The superior goal in the analysis of medical image data is the generation of new insights in on symptoms or diagnostic aspects. In case of virtual spirometry, the calculation of the separate lung volumes is of greatest importance for the determination of the extent of a disease or the monitoring of its process during therapy. As the result of virtual spirometry is a separated segmentation of both lungs, the volumes, and thereby as well static as dynamic parameters, can be calculated individually by classic voxel based volumetry. Given a 3D+t image and spatial resolution dx, dy, dz of the image I_t at time step t, the volume of each time step V_t can be calculated as

$$V_t = (\sum_{v \in S_t} g(I_t, v) \cdot dxdydz) \cdot 10^{-3} ml$$
$$g(I_t, v) = \begin{cases} 1, v \in S_t \\ 0, v \notin S_t \end{cases} \quad (4.25)$$

where v is iterated over all voxels of I_t, and S_t means the segmentation of the left and right lung, respectively. The time series can then be graphically represented over the total acquisition time (Fig. 4.16). The static lung volumes and capacities described in section 2.7.3 can then directly be calculated from these results, both individually for both lungs, and for the complete lung as sum of the single values. In general, the temporal resolution of the image time series will not be high enough to accurately evaluate dynamic parameters from volumetry of 3D+t images. This problem will be further addressed in section 4.9.

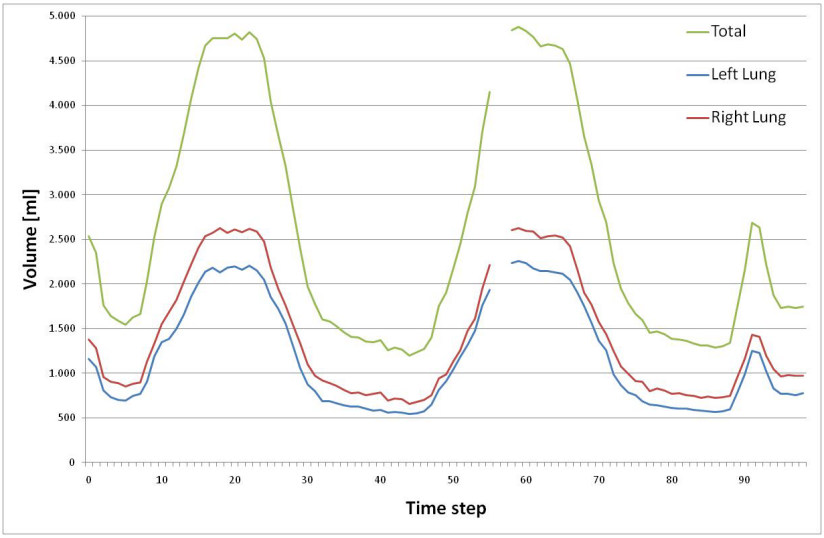

Fig. 4.16 Virtual spirometry during a breathing maneuver

Displayed are the individual signals for left and right lung, and the sum signal of both. The proband was asked to maximally inhale and exhale two times consecutively. Three time steps (Nr. 55-57) could not be segmented due to an image acquisition error.

One must note that the volumes calculated here do not only contain air, but also lung tissue and blood circulating inside the lung. Although the tissue can be seen as a constant offset over the breathing cycle, the blood volume changes depending on the heart phase. This will be further evaluated in the results part (section 5.6.1) and addressed in the discussion.

4.8.3 Motion field calculation

Due to the low image resolution and the absence of clearly visible lung structures as the bronchial tree in time resolved MRI images, a grey value based registration of the inner lung is nearly impossible, or has to be strongly restricted in mobility by regularization parameters. But, given the segmentation result of the deformable shape model as a triangle mesh with inherent landmark correspondences to the training data set and the model, an alternative approach is suggested. As for the complete time series a multitude of corresponding landmarks are present at the lung surface, the local movement of the inner lung can be interpolated from the movement of the surface landmarks. Here, Elastic-Body-Splines (EBS) developed by Davis et al. [103] are used. The basis of EBS is a physical model of

three-dimensional deformable objects based on a solution of the Navier-Stokes equation.

So under consideration that the lung is a homogeneous deformable body, local deformation of it can be approximated using EBS interpolation, allowing it to calculate N-1 deformation vector images for N time steps. For each voxel, the movement from time step t to time step t+1 is calculated. Hereby, the transformation $EBS_{t+1}^{t}(g)$ is initialized with the surface landmarks of two consecutive time steps, then for each voxel g the vector field is calculated as

$$v_t(g) = EBS_{t+1}^{t}(g) - g \tag{4.26}$$

As the approximation only is a valid solution for the inside of the lung (outside the assumption of a homogeneous deformable body is not given), for the lung deformation analysis the image is cropped to the lung parenchyma via the segmentation result. For convenience and easier diagnosis, the local movement is also shown in 2D view as color coded voxels, with colors assigned according to the voxels movement vector's magnitude via a lookup table.

As N-1 vector fields of local movement are still a huge amount of data to analyze for large N, and local movement between two time steps is often not too informative because it strongly depends on the breathing maneuver a patient is undergoing, it is also possible to show the sum of all local movements in a color map. Here, the value assigned to a voxel is given by

$$w(g) = \sum_{i=0}^{N-2} \left| v_i(g) \right| \tag{4.27}$$

Summation ends at N-2 as for the last image no movement information can be calculated. The values calculated this way directly show local movement restrictions, as they are directly proportional to the tissue elasticity or stiffness, respectively.

An example of deformation vector fields and a local movement color map can be seen in Fig. 4.17.

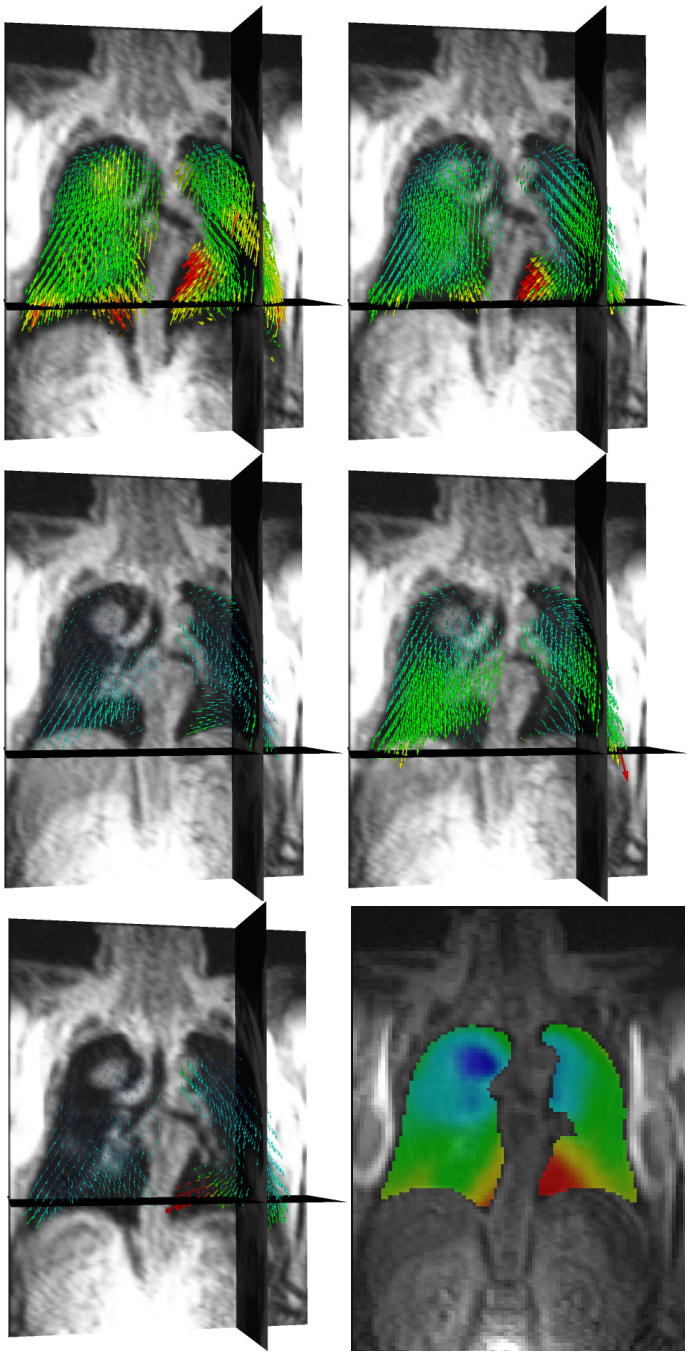

Fig. 4.17 Local lung motion estimation

Example images of a local lung motion estimation by vector field calculation of 3D+t lung images on a patient with a tumor in the upper right lung. The last image shows a color map pf the integrated motion for each voxel over all time steps (compliance map). Adapted from [22].

4.9 2D+t Pulmonary Function Analysis

Although 3D+t imaging using MRI is under constant development and has achieved considerable increases in terms of tempo-spatial resolution, acquisition time is still in the field of 0.5 seconds, which is still too slow to thoroughly diagnose a quantitative movement restriction or e.g. predict a precise tumor movement path for radiation therapy. Also, although the temporal resolution of 3D+t imaging is high enough to calculate static diagnostic parameters precisely, the temporal resolution is not sufficient to generate dynamic parameters from the images.

A proposed diagnostic method to gain increased temporal information is to apply highly time resolved 2D+t MR imaging on the patient after 3D+t image acquisition. Modern 2D+t imaging sequences have a temporal resolution of up to 10 images per second, which is sufficient to also analyze dynamic processes in the lung.

A natural drawback in 2D imaging is that only areas of the lung are imaged, which makes it harder to correlate changes in area with true volumetric parameters. To analyze the effect of plane orientation on the correlation of areas and volumes, 3D+t image time series have been segmented with the above described methods. Because it would be enormously time consuming to really acquire 2D+t images in a sufficient number of different angles, the image acquisition has been simulated. At each time step of these series, acquisition planes have been simulated by inserting cut planes at given angles θ and ϕ against the sagittal plane, and going through the center of mass of the left or right lung, respectively (Fig. 4.18). These planes therefore show an area of the lung as a so oriented 2D plane would. These areas at the particular angles have been normalized to the acquired volumes and been compared with the acquired volumes, and the mean difference over the whole time series has been calculated. The calculations and results in detail are presented in section 5.7.

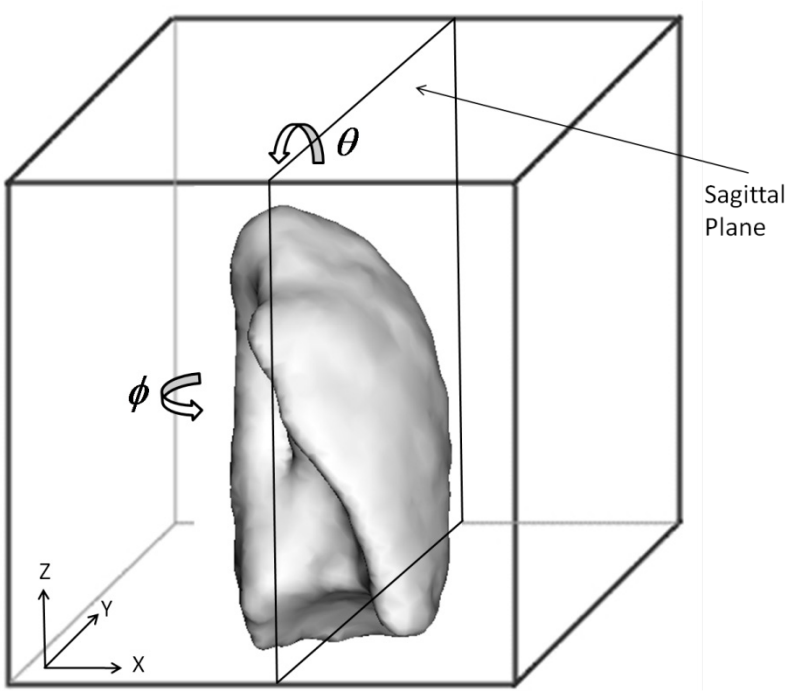

Fig. 4.18 Simulated 2D image acquisition.

A 2D image acquisition is simulated by clipping with a cut plane at different angles in a 3D segmentation result. Example of the left lung.

4.10 2D+t image analysis

Although it would be possible to apply a deformable model based approach again for the segmentation and lung area calculation of the image time steps, it would be very time consuming to do this slice-wise with an iterative approach, due to the sheer number of time steps that are generally acquired in dynamic 2D MRI. Also the images offer a much higher contrast and spatial resolution than the dynamic 3D images due to the reduced dimensionality and field of view. Therefore an approach was developed to segment all time steps simultaneously in a semi-automatic workflow.

Segmentation of lung area was done for each image stack with a semiautomatic application (Fig. 4.19) based on a Graph Cut algorithm [104, 105] that was implemented in the Medical Imaging Interaction Toolkit MITK [100]. For segmentation, the time resolved 2D images were considered as a three-dimensional image stack with time as the third dimension. On this three-dimensional image, the algorithm had to be initialized by first adapting a bounding box as

Region of Interest (ROI) to the size of the measurement area and then manually marking both the inside and the outside of the lung with a rough scribble spanning all time steps. The lung area for each time step was then segmented automatically. In about half of the segmented lungs, the segmentation leaked into the thoracic wall. In these cases, for correction, an additional scribble had to be drawn at the point of leakage. For the coronal images, the segmentation was performed for each side separately.

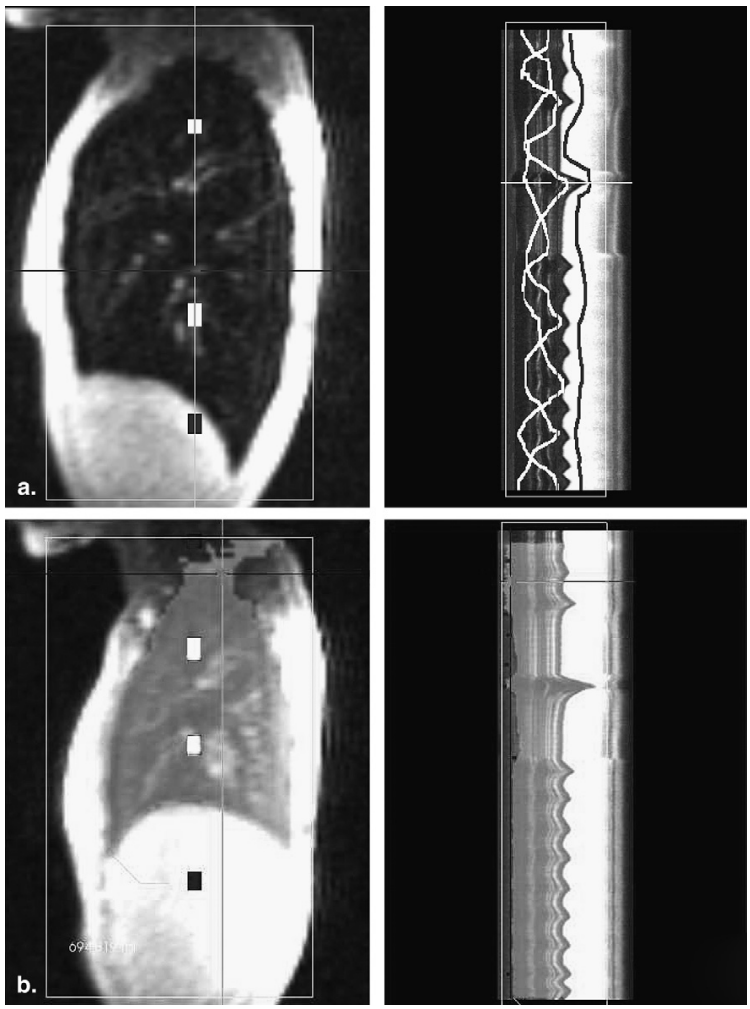

Fig. 4.19 Segmentation scheme for 2D+t image analysis

(a) Two-dimensional (2D) time series visualized as 2D plus time volume with the sagittal image of a single time step on the left and a cut through the time series on the right. The scribbles marking the inside (white) and outside (gray) of the lung are the initialization of the segmentation algorithm. (b) Automatic segmentation of the lung seen in lighter gray with a segmentation leakage at the apex, which had to be corrected by manually drawing the lung boundary in this area.

5 Results

In this chapter, the experimental setups as well as evaluation results of the methods developed in the scope of this thesis are listed in detail. The first part covers the segmentation basis, evaluating deformable model and multi-organ segmentation as well as manual correction (section 5.1 to 0). The second and third part deal with the usability of the segmentation results for computer aided diagnosis of cardiac motion restriction (section 5.5) and pulmonary motion restriction (section 5.6 to 5.8), respectively.

5.1 Evaluation of Segmentation Quality

This chapter gives an overview over the result quality of the proposed methods compared to a manually segmented gold standard. In the first part, it is shown that the segmentation with deformable shape models gives sufficient results to conduct medical diagnostics with their help. The second part states the improvements in quality gained by the incorporation of multi-organ knowledge. The third part evaluates the usefulness of a post-segmentation manual correction.

5.1.1 Evaluation Metrics

As quality measures for the segmentation results, the average symmetric point-to-surface distance, symmetric RMS point-to-surface distance, and the Dice coefficient were used for comparison against a gold standard from medical experts. These are defined as follows: The distance from a point x to a surface Y is given by

$$d(x,Y) = \underbrace{\min}_{y \in Y} \left\| x - y \right\|, \tag{5.1}$$

where $\left\| . \right\|$ denotes the Euclidian distance. When defining surface distances, we have to make sure to respect symmetry, a precondi-

tion for every metric. Thus, the average surface distance is defined as:

$$D_{avg}(X,Y) = \frac{1}{\left|X\right| + \left|Y\right|}\left(\int_{x \in X} d(x,Y)dx + \int_{y \in Y} d(y,X)dy\right)' \quad (5.2)$$

where $\left|.\right|$ denotes the area of a surface. In a similar fashion, the root mean squared surface distance (equivalent to the RMS error) is defined as

$$D_{RMS}(X,Y) = \sqrt{\frac{1}{\left|X\right| + \left|Y\right|}\left(\int_{x \in X} d^2(x,Y)dx + \int_{y \in Y} d^2(y,X)dy\right)} \quad (5.3)$$

The last used metric, the Dice coefficient, is a measure to quantify the similarity between two regions A and B, based on the volumetric overlap:

$$C_D = \frac{2\left|A \cap B\right|}{\left|A\right| + \left|B\right|}, \quad (5.4)$$

where $\left|.\right|$ denotes the volume of a region. The Dice coefficient yields 1 if both shapes are identical and 0 for no overlap at all. To transform the measure into an error metric, the obvious way is to negate it. Thus, the volumetric error based on the dice coefficient is defined as:

$$V_D = 1 - C_D \quad (5.5)$$

5.2 Segmentation of the Left Ventricle

5.2.1 Experimental setup

To evaluate the segmentation quality of the deformable model for the use of left ventricular volumetry, several 3D images of the end-diastolic and end-systolic left ventricular (LV) endocardium have been segmented and compared with a manually obtained gold standard.

End-diastolic LV

The dataset used for evaluation of the segmentation quality consists of 22 MRI images of the upper torso, in which the left ventricle has been manually pre-segmented by medical experts. The images have resolutions of 256x256x160 (19 images), 128x128x88 (1 image) and 128x128x80 (2 images), respectively. As multiple gold standard segmentations per image were available, but were varying distinctly in some cases, these where averaged for each single image using a STAPLE ground truth image filter, as described in [106].

Because not enough data was provided to separate the dataset in training and evaluation parts, leave-one-out tests were performed. Thus, 22 shape models were built, and in each case evaluated on the single volume not included in the build process.

End-systolic LV

This dataset consists of only 21 MRI images and the corresponding pre-segmentations. The images have resolutions of 256x256x160 (18 images), 128x128x88 (1 image) and 128x128x80 (2 images), respectively. All other properties are equal to the diastolic LVs. So this time, 21 models were trained and leave-one-out tests were performed.

Volumetry

The heart stroke volume (SV) is calculated as the difference between the segmented end-diastolic and end-systolic ventricle volumes, respectively. The results were compared with the differences of the given gold standard segmentations. In 13 cases, also direct mea-

surements of the stroke volume via velocity-encoded cine MR imaging (VEC MRI, see e.g. [107]) were available and used for comparison.

5.2.2 Results

The segmentation results for the left heart ventricle in systolic and diastolic phase are shown in Table 5-1 and Table 5-2. Additionally, graphs of the average surface distance results are given in Fig. 5.1 and Fig. 5.4.

An example of end-diastolic LV segmentation images is shown in Fig. 5.2. An example of a 3D view can be seen in Fig. 5.3.

Table 5-1 Segmentation results for the end-diastolic LVs.

Results are given as mean ± standard deviation (μ±σ).

Method	D_{avg}[mm]	D_{RMS}[mm]	V_{Dice}[%]
Deformable model	0.95±0.21	1.58±0.42	6.4±1.2
Lötjönen et al. [108]	2.01±0.31	n.a.	n.a.
Kaus et al. [109]	2.28±0.93	n.a.	n.a.
van Assen et al. [110]	1.97±0.54[1]	n.a.	n.a.

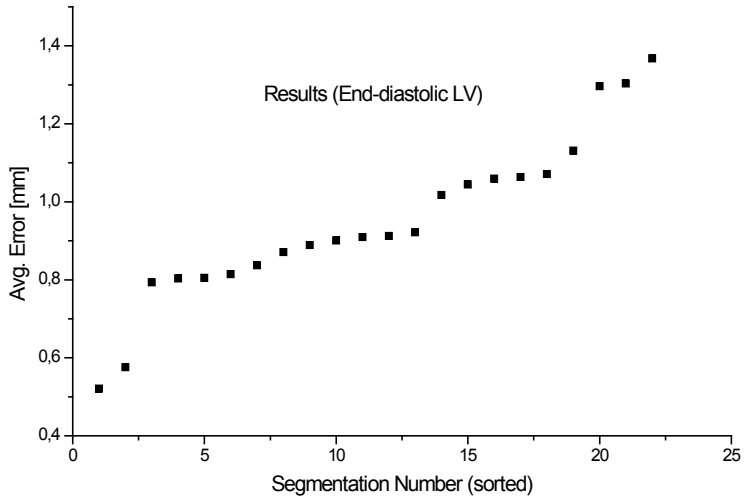

Fig. 5.1 Distribution of the segmentation error for the end-diastolic LV

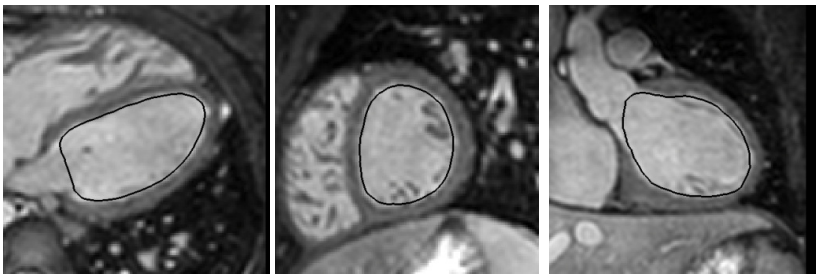

Fig. 5.2 Example of sagittal, transversal and coronal view of the median end-diastolic LV segmentation

The resulting surface is shown as a black line.

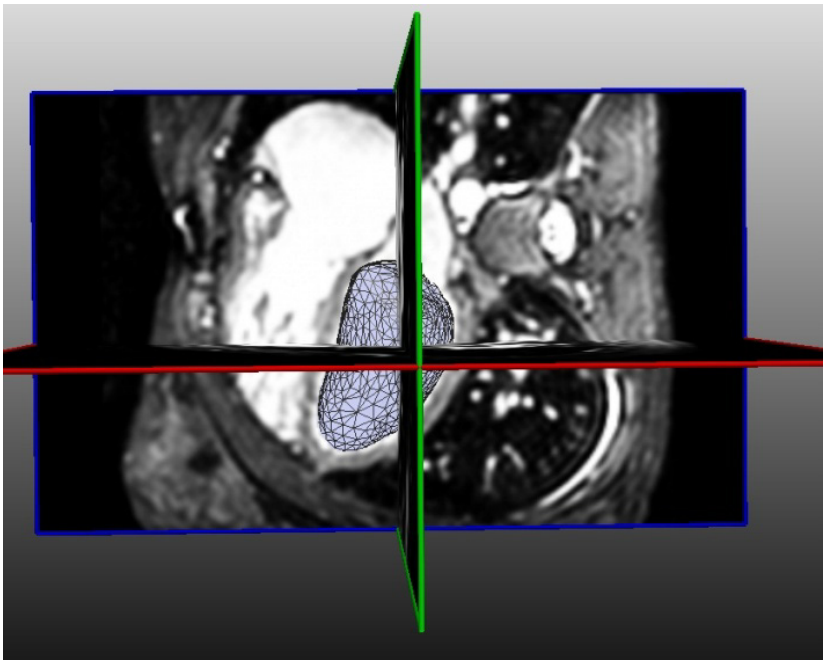

Fig. 5.3 3D view of the segmentation result as a wireframe mesh

Also, the cut planes from Fig. 5.2 can be seen.

Table 5-2 Segmentation results for the end-systolic LVs.

Results are given as mean ± standard deviation (μ±σ).

Method	D_{avg}[mm]	D_{RMS}[mm]	V_{Dice}[%]
Deformable model	1.69±0.68	2.48±1.01	16.2±5.3
Kaus et al. [109]	2.76±1.02	n.a.	n.a.
van Assen et al. [110]	1.97±0.54[1]	n.a.	n.a.

[1] van Assen et al. do not state the cardiac cycle stage they used their segmentation on.

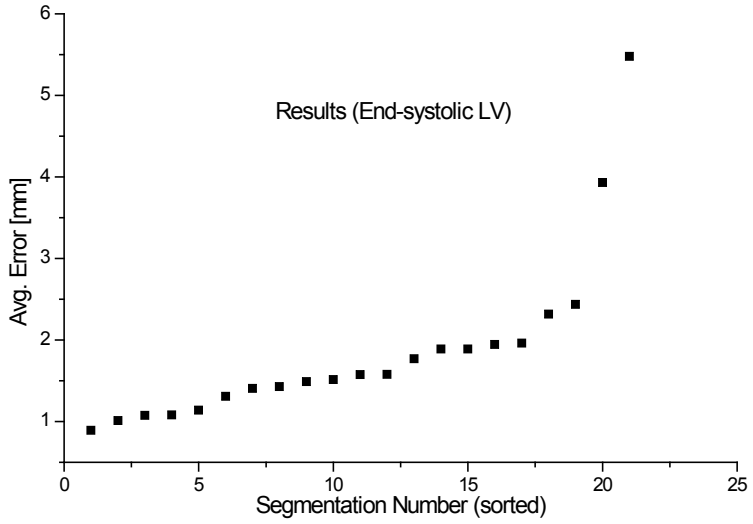

Fig. 5.4 Distribution of the segmentation error for the end-systolic LV

Volumetry

In Table 5-3, the heart stroke volume results, compared with the direct measurement and with the calculated gold standard are given, showing the result of the computation in terms of the mean relative error (The relative error of the single results compared to the appropriate gold standard, averaged over all results). Also, the Pearson product-moment correlation coefficient is stated, giving a dimensionless measure of the linear correlation between two random variables.

Table 5-3 Results of stroke volume (SV) computation

Comparison against two different methods for SV calculation. In both cases, only the 13 images for which the direct measurement was given are evaluated.

SV compared to:	Direct Measurement	Difference of gold standard segmentations
Mean rel. error [%]	12.4	8.4
Pearson's correlation coefficient	0.89	0.97

5.3 Coupled Model Segmentation

In this section, the segmentation quality of the different proposed methods for model correlations is evaluated on the epicardium and endocardium of the left heart ventricle. The usability of the methods for diagnostic purposes is evaluated later on in section 5.5 and 5.6.

5.3.1 Experimental setup

Training data for the statistical models consisted of dynamic ECG-triggered short axis MR images of 32 patient's hearts. Each image was a time series featuring 25 time steps over the complete heart cycle. In each image, the epi- and endocardium in systolic and diastolic phases were manually delineated by medical experts. Additionally, from two other patients, complete time series were included. Each of these had the epi- and endocardium manually delineated in 25 time steps, covering one complete heart cycle. The images had a resolution of 128 x 128 x 18 voxel with a [1.6, 1.6, 5.0] mm image spacing.

Test data sets were nine images from the same type, covering three patients. The images had pairwise different time steps, i.e. points in heart phase, except for two.

These images were chosen because they on the one hand are common in cardiac diagnosis and on the other hand show low image quality in the spatial domain because of the high temporal resolution, making segmentation very challenging compared to the 3D data set evaluated in section 5.2. Imaging artifacts appear very often as well as shifts of single planes in x-y direction due to the ECG triggering.

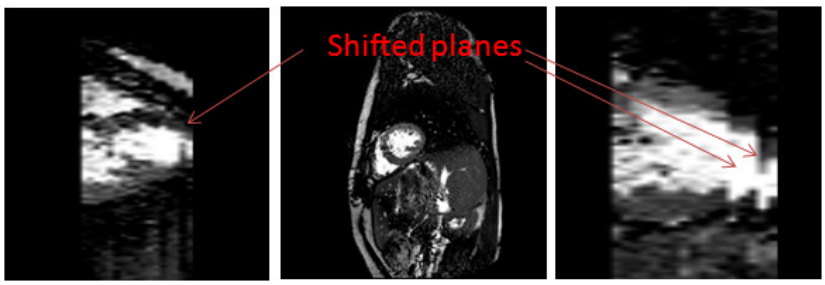

Fig. 5.5 Example data set of left ventricular data

Transversal (left), sagittal (middle) and coronal (right) view. Typical image acquisition artifacts are highlighted

The shape models built for validation were relatively compact and allowed a good representation of the heart wall. For segmentation, each model was restricted to its first 10 modes of variation, constituting more than 90% of the overall variation encountered in the training sets. The single models and their three strongest modes of variation are shown in Fig. 5.6 and Fig. 5.7.

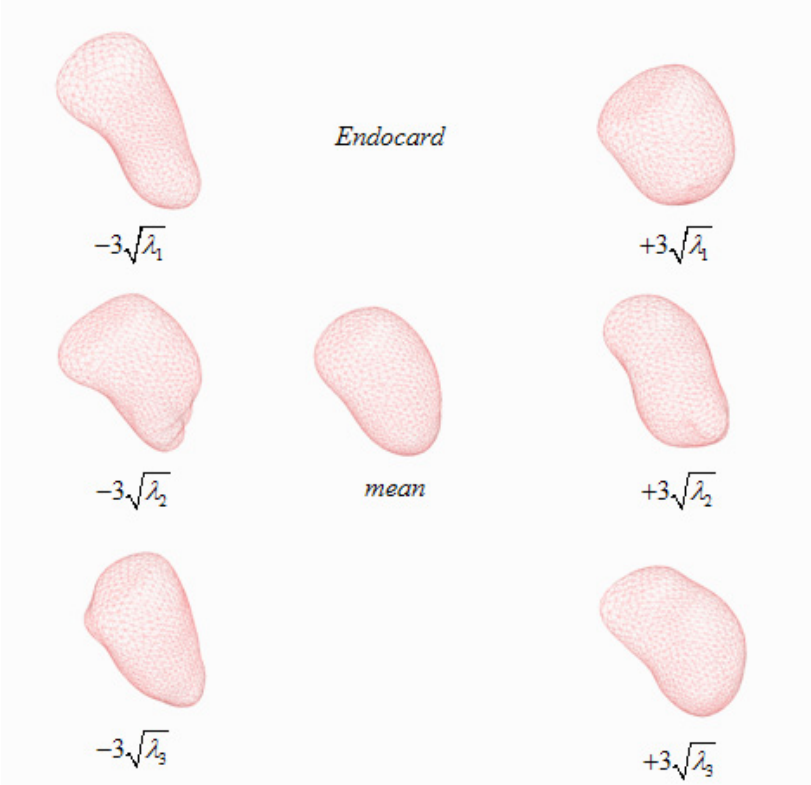

Fig. 5.6 Mean model and three strongest modes of variation of the endocardium

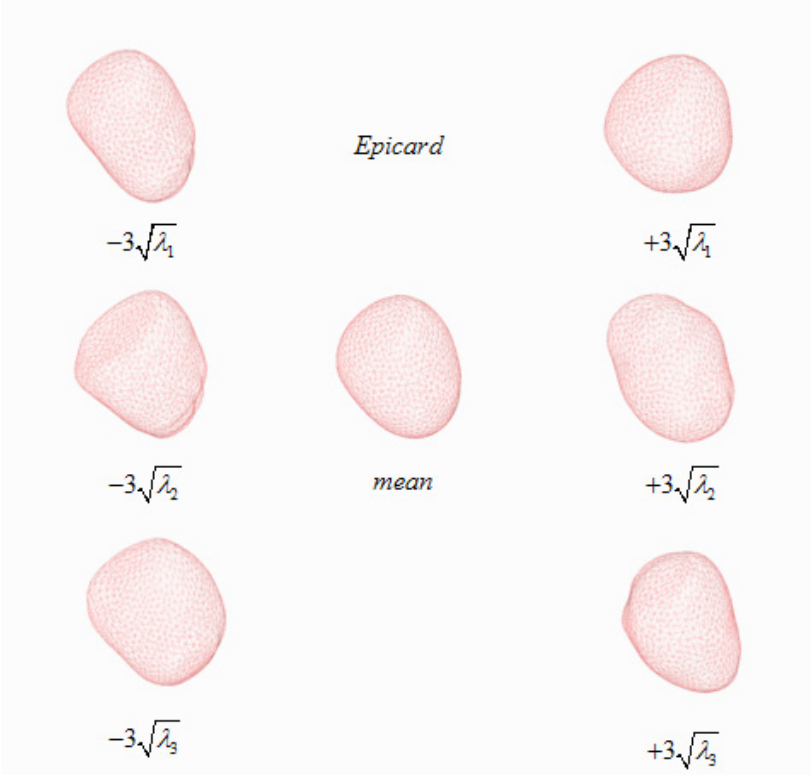

Fig. 5.7 Mean model and three strongest modes of variation of the epicardium

5.3.2 Results – Shape Space Coupling

The segmentation results for the different shape space correlation methods are shown in Table 5-4 and Table 5-5. Each number displays the error between the automated segmentation results and the manual gold standard segmentations, averaged over all testing data. Fig. 5.9 and Fig. 5.10 show example images in standard views for the results from the different methods.

Table 5-4 Mean and standard deviation of error for segmentation result of the endocardium using shape space coupling

Endocardium	D_{avg} [mm]	D_{rms} [mm]	V_D [%]
Standard	3.65±1.16	6.21±1.79	29.31±10.48
Joint - Relaxed	3.82±2.23	6.19±3.53	25.53±14.57
Joint - Strict	2.54±0.86	4.43±1.33	17.82±7.23
Unified - Relaxed	3.34±1.21	5.20±1.92	24.61±9.64
Unified - Strict	3.71±2.16	6.22±3.52	28.06±14.31

Table 5-5 Mean and standard deviation of error for segmentation result of the epicardium using shape space coupling

Epicardium	D_{avg} [mm]	D_{rms} [mm]	V_D [%]
Standard	3.80±1.28	6.61±2.02	18.72±6.43
Joint - Relaxed	2.34±0.58	4.15±0.91	9.86±2.42
Joint - Strict	2.14±0.57	4.02±1.00	8.58±2.33
Unified - Relaxed	4.41±0.63	6.10±0.59	20.66±3.74
Unified - Strict	2.35±0.64	4.34±0.96	10.27±3.84

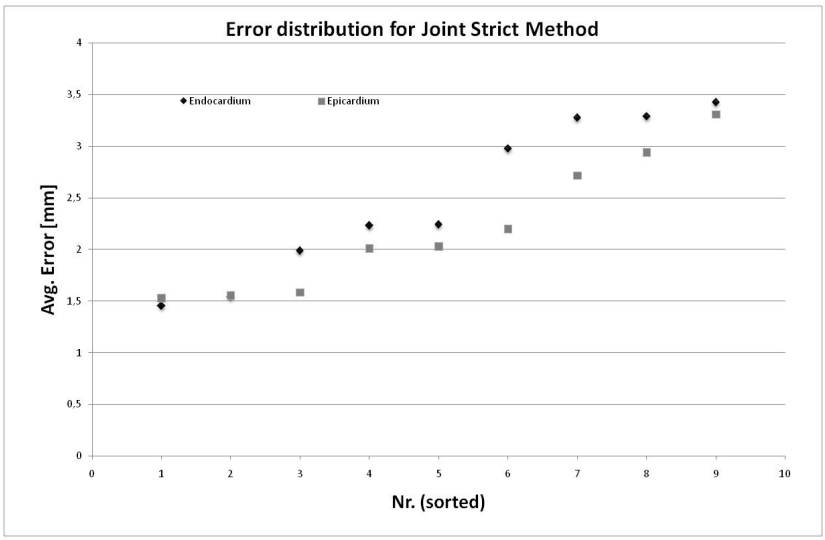

Fig. 5.8 Error distribution for the joint – strict method.

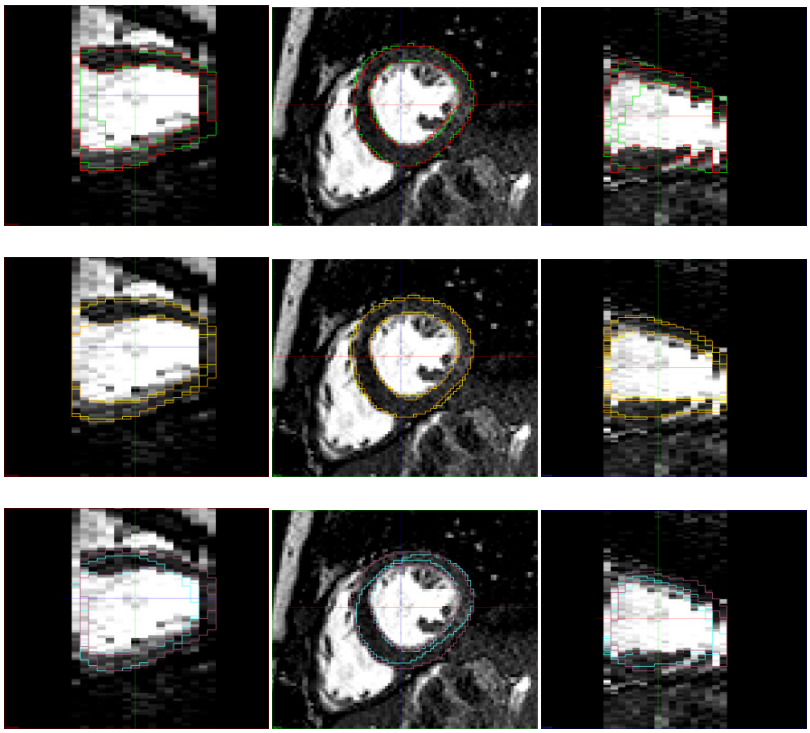

Fig. 5.9 Exemplary results for the proposed methods

Left to right: Transversal, sagittal and coronal view; Colors: Red: Manual segmentation. Green: Single SSM result. Yellow: Joint – Relaxed method. Orange: Joint – Strict method. Light blue: Unified – Relaxed method. Purple: Unified – Strict method.

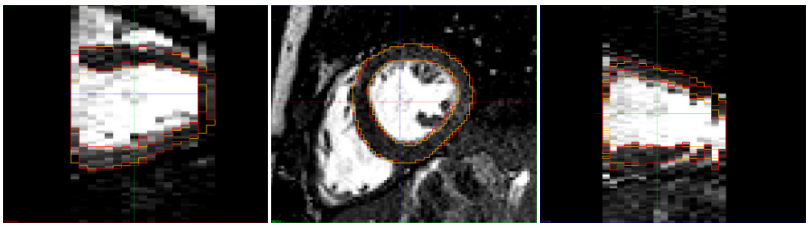

Fig. 5.10 Direct comparison of the best method and the manually segmented gold standard

Left to right: Transversal, sagittal and coronal view; Colors: Red: Manual segmentation. Orange: Joint – Strict method.

5.3.3 Results – Geometrical Coupling

The usability of a geometrical coupling was evaluated on the same image data as in the last section. The geometrical force term was applied alone (in addition to the deformable model force terms), and together with the joint-strict shape space coupling, which showed best results in the last section. Results are given in Table 5-6 and Table 5-7. Fig. 5.11 shows the error distribution for both endocardium and epicardium, and an example can be seen in Fig. 5.12.

Table 5-6 Mean and standard deviation of error for segmentation result of the endocardium using geometrical coupling

Endocardium	D_{avg} [mm]	D_{rms} [mm]	V_D [%]
Standard	3.65±1.16	6.21±1.79	29.31±10.48
Geometrical	3.57±1.19	5.86±1.74	25.29±10.46
Joint – Strict + Geometrical	2.49±0.77	4.35±1.19	17.10±6.29

Table 5-7 Mean and standard deviation of error for segmentation result of the epicardium using geometrical coupling

Epicardium	D_{avg} [mm]	D_{rms} [mm]	V_D [%]
Standard	3.80±1.28	6.61±2.02	18.72±6.43
Geometrical	2.23±0.50	4.22±0.82	8.62±2.26
Joint – Strict + Geometrical	2.21±0.65	4.08±1.11	8.58±2.88

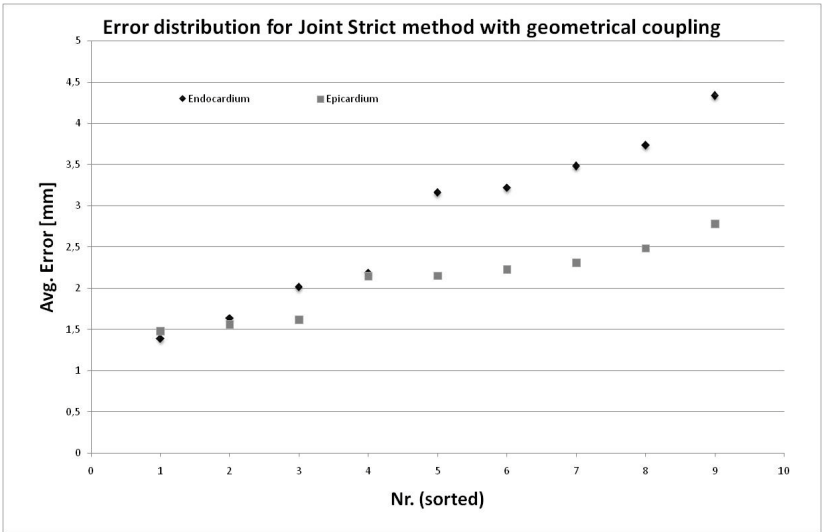

Fig. 5.11 Error distribution for the joint – strict and geometrical method

Fig. 5.12 Direct comparison of geometrical coupling with joint - strict shape space coupling against the manually segmented gold standard

Left to right: Transversal, sagittal and coronal view; Colors: Red: Manual segmentation. Brown: Joint – Strict + geometrical method.

5.4 Manual Correction

5.4.1 Experimental setup

To evaluate the deformation tool as described in section 4.5, two radiological experts were asked to manually correct erroneous segmentations of the left heart ventricle and the liver. Although this thesis focuses on heart and lung evaluation, in case of the lungs, segmentation was in general very good besides the lower tips of the lung, which were under-segmented in all cases. As this can be corrected in seconds and does not give much information on the usability of the manual correction possibility on more complicated segmentation errors, the liver was chosen as subject of evaluation because of the more complex segmentation problem and the resulting variety of mis-segmentations compared to the lungs.

For both test cases, a deformable model segmentation approach as described in section 4.1 and 4.2 was used without any further optimization, because typical segmentation problems appearing were wanted for the evaluation of manual correction. The time effort for the manual correction came to an average of 1-2 minutes for the heart ventricles, and about 4-5 minutes for the livers. Both the automated segmentation and the manual correction were compared against a given ground truth created by manual delineation of the organ by a medical expert, using different distance measures as stated in section 5.1.1.

Left Heart Ventricle (LV)

Image data and deformable model used for the left ventricle evaluation ware the same as described in section 5.2. On all 22 images, automated segmentations were created. Then, the images taken for manual correction were selected as the worst five of the automated segmentations compared to the ground truth out of the series of 22 volumes.

Liver

The Liver data consists of 32 CT volumes of the whole body, containing the complete liver. Again, manually slice-by-slice produced gold standard segmentations were given. Automated segmentations were created for all images, and the worst 5 out of the series of 32

volumes were picked for manual correction, without consideration of 3 segmentations which were regarded as failed in segmentation beyond manually correction. Image resolution differed between 512x512x41 and 512x512x146 voxel [96].

The shape model used for segmentation consisted of 2562 landmarks. For the segmentation of the liver, which is considerable more complex in shape, a moderated k-Nearest-Neighbors classifier [94] was used.

5.4.2 Results

The complete results before and after manually corrections are shown in Table 5-8 and Table 5-9.

Example images with overlaid result segmentations before and after manually corrections are shown in Fig. 5.13 for the left ventricle and in Fig. 5.14 for the liver.

Table 5-8 Results for the left ventricle

Upper: Before correction. Lower: After correction.

Heart Ventricle before Correction	D_{Avg} in mm	D_{RMS} in mm	V_D [%]
Mean	2.71	5.24	14.51
Std. Deviation	0.83	1.40	3.61
Heart Ventricle after Correction			
Mean	1.34	2.18	8.29
Std. Deviation	0.36	0.78	1.87

Table 5-9 Results for the liver

Upper: Before correction. Lower: After correction.

Liver before Correction	D_{Avg} in mm	D_{RMS} in mm	V_D [%]
Mean	2.43	4.48	7.25
Std. Deviation	0.90	1.75	1.74
Liver after Correction			
Mean	2.17	3.96	6.58
Std. Deviation	0.52	0.87	1.16

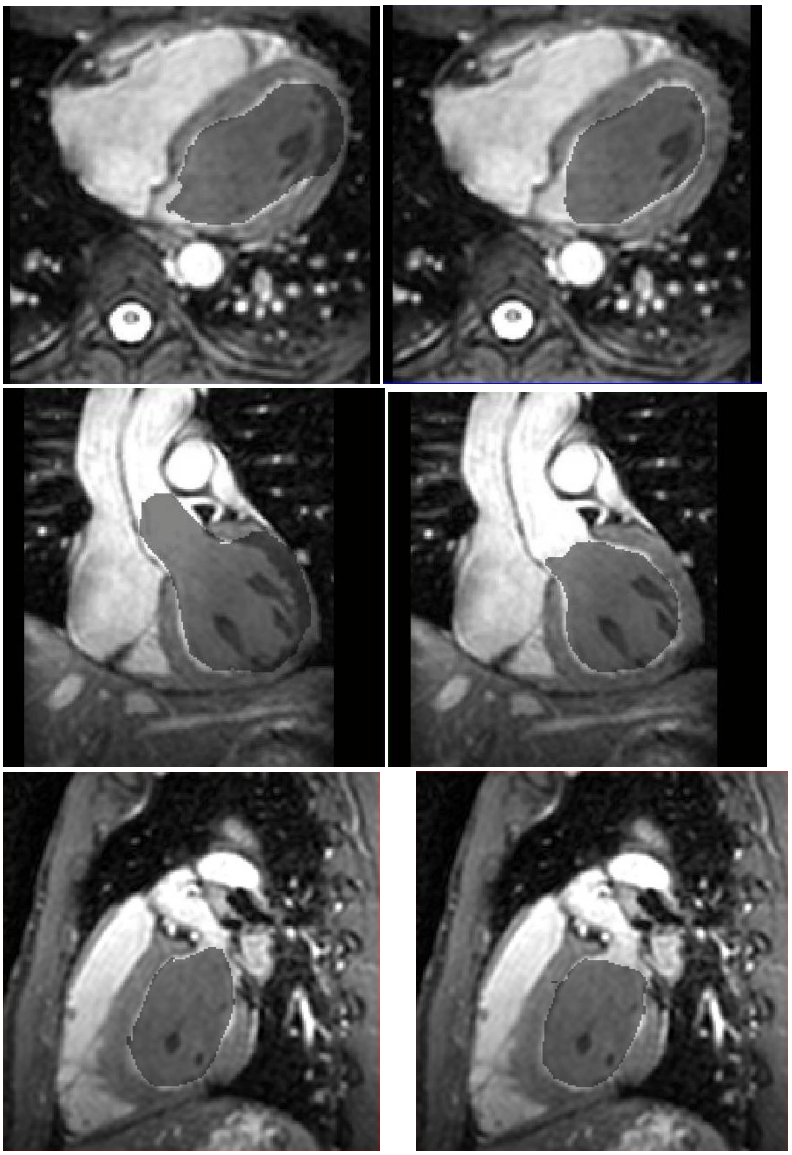

Fig. 5.13 Exemplary results before and after manual correction – left ventricle

Upper row: The transversal, frontal and sagittal view of the heart directly after the automated segmentation, before manual corrections. Lower row: The same view, after manual correction. The segmentation result is shown in opaque grey in all views.

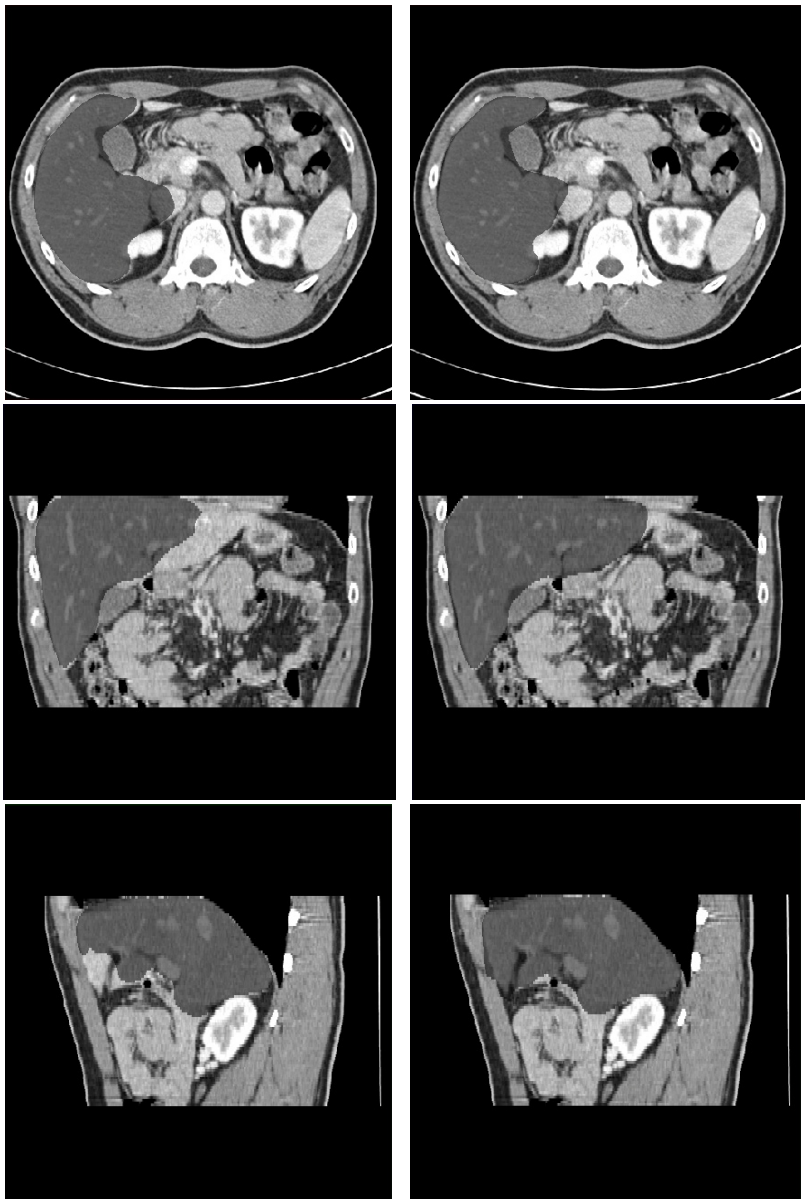

Fig. 5.14 Exemplary results before and after manual correction – liver

Upper row: The transversal, frontal and sagittal view of the liver directly after the automated segmentation, before manual corrections. Lower row: The same view, after manual correction. The segmentation result is shown in opaque grey in all views.

5.5 Evaluation of Cardiac Motion Analysis

This chapter presents the results obtained in the evaluation of the Bull's Eye projection and the calculation of the physiological parameters of the heart. The results were obtained both on synthetic data and on real patient image data. Aim of the evaluation is to show the accuracy of the calculated parameters, and to show that the mean calculation error is below the average segmentation error and therefore can be neglected.

5.5.1 Synthetic data

As synthetic data, open elliptic paraboloids of different radii, but equal height were used. These were chosen because they represent a mathematically simple geometric shape which is similar to a heart ventricle. To further approximate the shape of a ventricle, the lowest 5% height at the basal part of the paraboloid was not included for evaluation, as the ventricle apex is considered as immobile by the AHA standard and does not contribute to wall motion.

Evaluation of Bull's Eye Projection Error

For the evaluation of the projection to a Bull's Eye diagram, an elliptic paraboloid with a radius of 10mm and a height of 30mm was used, represented as a highly resolved triangle mesh. Each segment of the Bull's Eye diagram was assigned with a discrete value, from a scale of values that covered values occurring in heart physiology for wall motion. The range was chosen as 5-20mm per heart cycle. Table 5-10 shows the assigned values. According to this distribution, each point of the paraboloid was assigned a value depending on its height and angle. Fig. 5.15 shows how a projection from the paraboloid to the Bull's Eye should look in theory.

Table 5-10 Discrete values assigned for projection error calculation

Basal segments						
Segment Nr.	1	2	3	4	5	6
Assigned value	5	7	9	10	8	6

Mid segments						
Segment Nr.	7	8	9	10	11	12
Assigned value	15	17	19	20	18	16

Apical segments				
Segment Nr.	13	14	15	16
Assigned value	5	7	8	6

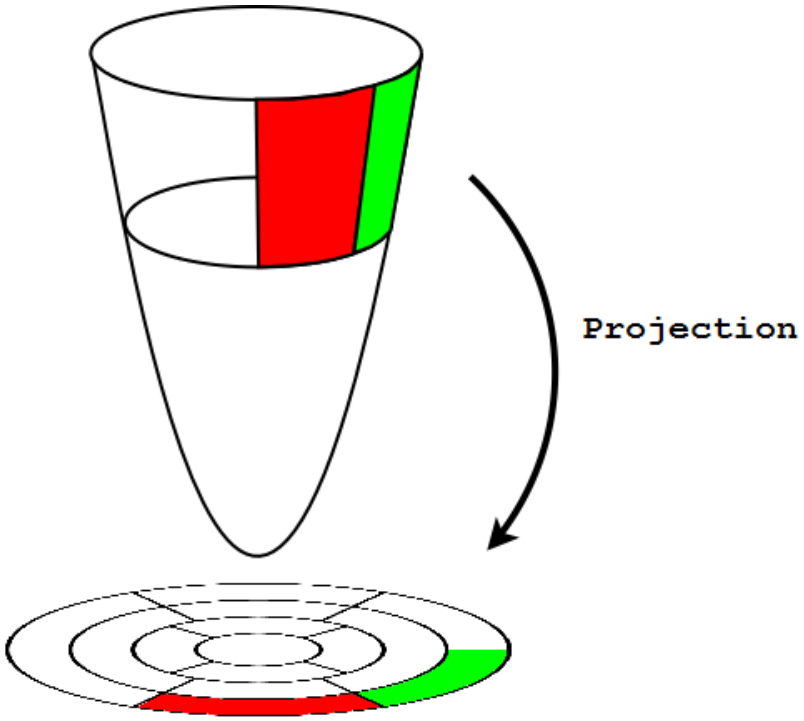

Fig. 5.15 Projection of a color coded surface to a Bull's Eye diagram.

A drawback of discrete values per segment is that they are problematic when interpolating in the projection. Therefore, as the surface is cut along the longitudinal axis, the values between the vertical areas (basal, mid-cavity, and apical) are interpolated. As discontinuities as created here between the segments by the use of discrete values normally not appear in cardiac images, the error calculation still gives an estimation of the worst case expected value.

Based on the possibility to evaluate the Bull's Eye diagram per segment as described in section 4.7.1, the projected and interpolated values can be compared to the theoretically expected values. The evaluation thereby gives the mean error of the projection, which is necessary to be known for the calculation of the other parameter errors and has to be compared against the segmentation error.

Evaluation of Wall Thickness Calculation Error

To evaluate the amount of error the calculation of wall thickness contributes due to the calculation of closest landmarks between epicardium and endocardium (which is faster to compute) instead of the mathematically correct smallest distances at each point (see section 4.7.3), two ellipsoids with same height and different radii have been created, featuring the same number of landmarks as the used models. For each section, the mean values of the closest-point calculation were generated and compared to the calculated expectation values generated from the ellipsoid equations.

5.5.2 Results on synthetic data

Fig. 5.16 shows a diagram created using the values given in Table 5-10. These are color coded according to their assigned value. The interpolation errors at discrete borders can be seen as color gradient. Table 5-11 shows the projected mean values per segment, the mean projection error for each segment, as well as for each segment group. Table 5-12 shows the result of the wall thickening calculation error.

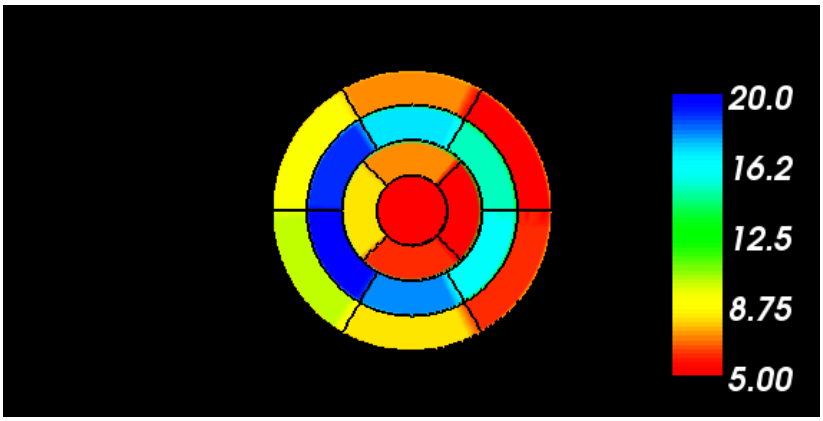

Fig. 5.16 Bull's Eye diagram of the projection error test values

Table 5-11 Projection error evaluation results

Basal segments						
Segment Nr.	1	2	3	4	5	6
Assigned value	5	7	9	10	8	6
Calculated value	5.22	7.02	8.87	9.76	7.94	6.12
Difference	0.22	0.02	0.13	0.24	0.06	0.12
Mean Group Error			0.13±0.08			

Mid segments						
Segment Nr.	7	8	9	10	11	12
Assigned value	15	17	19	20	18	16
Calculated value	14.77	16.72	18.75	19.72	17.74	15.75
Difference	0.23	0.28	0.25	0.28	0.26	0.25
Mean Group Error	0.26±0.02					

Apical segments				
Segment Nr.	13	14	15	16
Assigned value	5	7	8	6
Calculated value	7.66	8.76	6.81	5.69
Difference	2.66	1.76	1.19	0.31
Mean Group Error	1.48±0.99			

Table 5-12 Wall thickness calculation error

Difference betweeen expected and calcualted values

Segment group	Basal	Mid	Apical
Expected value (mm)	3.75	4.92	3.75
Mean calculated (mm)	3.61	4.92	3.61
Difference (mm)	0.14	0.0	0.14

5.5.3 Evaluation on Patient Data

For a quantitative validation of the presented methods on real patient image data, the minimal, maximal, and mean values of the wall thickness and wall thickening were calculated with the application on datasets of ten patients. These datasets consisted of MRI images with a spatial resolution of 1.84 x 1.84 x 5.0 mm and a temporal resolution of 25 time steps per heart cycle. The calculated values were evaluated against manually obtained distance measurements done by a cardiologic expert. The expert hereby referred to three segments of each data set in which he could obtain the best measurements to his opinion. Each segment was measured in two perpendicular image slices, corresponding to the standard described in [102]. To compare the measurement results, the expert performed two measurements of the minimal and maximal size of the heart wall in the plane he could do the best measurement, and one in the perpendicular plane. The mean of these three results was compared to the mean created by the automated methods (see section 4.7.3) and are presented in Table 5-13.

Fig. 5.17 gives an example of the used images. For the segmentation the parameter generation is based on, first the images were segmented with the deformable model approach as described in section 4.1, afterwards with the best performing coupled model (by using a joint shape space with strict parameter application, and an additional geometrical correlation term), as described in section 4.3. The single models used were the same as described in section 5.3.1. Both results were then compared as described above. Fig. 5.18 to Fig. 5.21 show exemplary results calculated for the patient from Fig. 5.17.

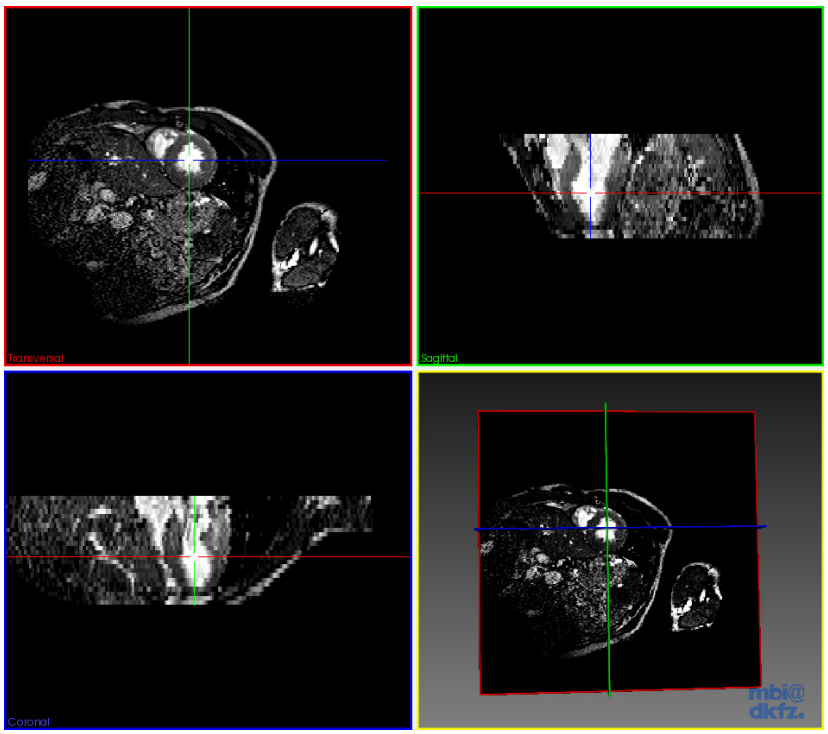

Fig. 5.17 Example image of an original heart data set

Top left: transversal view. Top right: sagittal view. Bottom left: Coronal view. Bottom right: 3D view.

Table 5-13 Results for dynamic parameter generation

The measurement error of the automatic methods is compared to a manually drawn measurement.

Parameter	Wall thick-ness	Wall thicken-ing
Mean error (deformable model) [mm]	2.12±1.89	2.78±2.38
Mean error (coupled model) [mm]	1.93±1.34	2.75±1.84
Max error (deformable model) [mm]	9.48	8.44
Max error (coupled model) [mm]	7.55	8.40

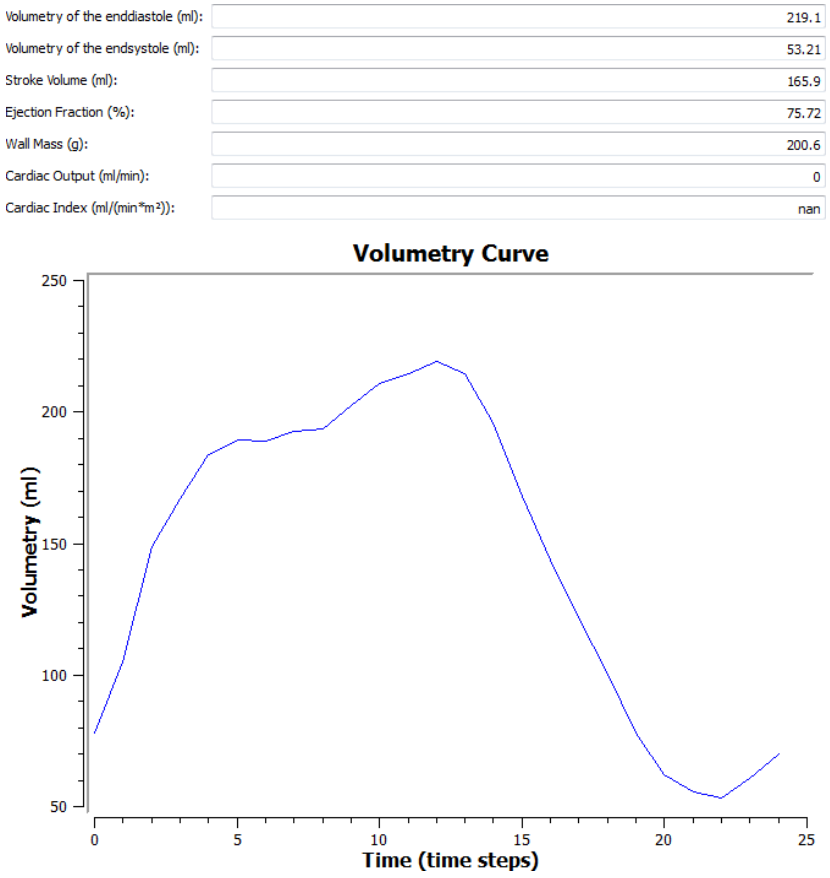

Fig. 5.18 Exemplary result of volumetric calculation on patient data

Cardiac output are omitteed as patient's body mass, height and heart rate were not given.

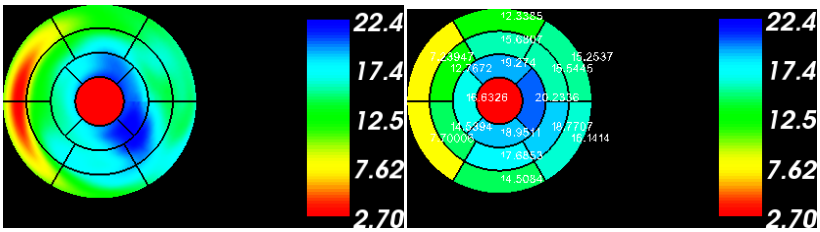

Fig. 5.19 Exemplary result of local (left) and regional (right) wall motion

Calculated between end-systole and end-diastole. Units are mm.

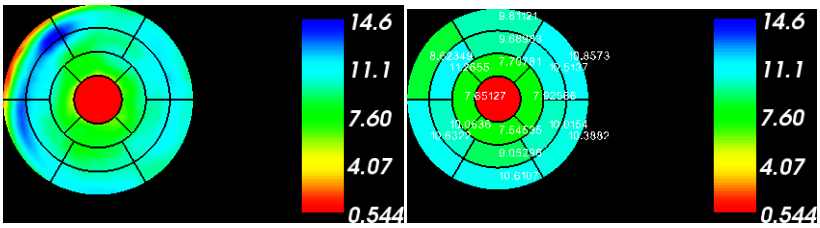

Fig. 5.20 Exemplary result of local (left) and regional (right) wall thickness

Calculated in end-diastole. Units are mm.

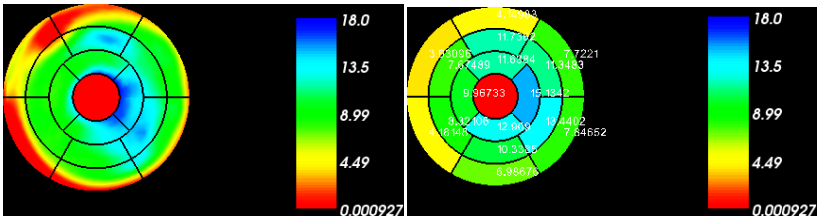

Fig. 5.21 Exemplary result of local (left) and regional (right) wall thickening

Calculated between end-systole and end-diastole. Units are mm.

5.6 Evaluation of Pulmonary Motion Analysis

In this chapter, the experimental setup and the results for the analysis of pulmonary motion are presented. First, the results of the 3D+t motion analysis using deformable and coupled models of shape (section 4.2 and 4.3) are compared against the gold standard, spirometry, and each other. Afterwards, the results of the plane simulation (section 4.9) are shown, and the results of 2D+t motion analysis (section 4.10) are compared against spirometry.

For both 3D+t and 2D+t evaluation, imaging was done with a 1.5 T Siemens Symphony MRI system. Volunteers were positioned on the MRI table and an eight-channel body coil was fixed over the thorax loose enough to not inhibit respiratory motion. For simultaneous spirometry, an MRI-compatible spirometer was used [111]. The volunteers held the handhold in whichever hand was more comfortable for them. They were asked to breathe through the spirometer only during acquisition of the dynamic sequences. To inhibit breathing through the nose, the patients had to wear a plastic nose clip throughout the MRI process.

5.6.1 3D+t Motion Analysis

Experimental setup

To analyze the respiratory function by means of volumetry statistical shape models were trained with datasets from 9 patients for both lungs, each consisting of 20 time steps over the complete breathing cycle to furthermore incorporate breathing motion information into the models. The image data was acquired using a breathing triggered FLASH3D MRI sequence and had a spatial resolution of 3.75x3.75x3.8 mm, and a temporal resolution of 1 second. As image data of all stages of the respiratory cycle is integrated in the model, the first mode of variation mostly represents the breathing motion.

The first 10 modes of variation were used for the models, representing more than 90% of shape variability. Each single model consisted of 1250 landmark. Fig. 5.22 and Fig. 5.23 show the mean models of the left and right lung as well as their strongest three modes of variation.

The evaluation data has been segmented with the deformable model approach as well as with the coupled model approach that showed best results (using a joint shape space with strict shape parameter application, see section 4.3). A geometrical coupling was not used, as the lungs are spatially and anatomically too far apart from each other to derive a meaningful spatial correlation.

Evaluation data consisted of TWIST4D sequences of three probands, featuring a spatial resolution of 3.52x3.52x8mm and a temporal resolution of 0.5 seconds. Each sequence featured 100 time steps, from which three time steps (55-57) were corrupted during image acquisition in each sequence and had to be omitted in the evaluation.

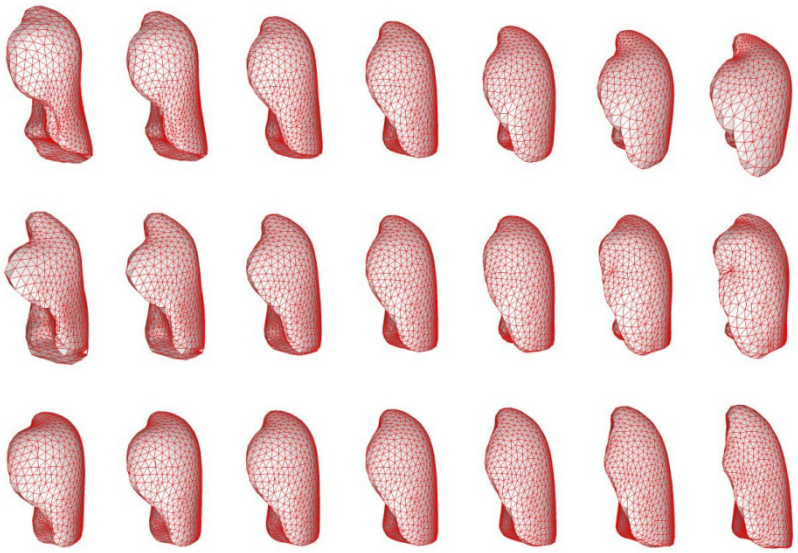

Fig. 5.22 Mean and strongest modes of variation of the left lung model.

The three strongest modes of variation are shown, top to bottom. Rows show the variation over three standard deviations.

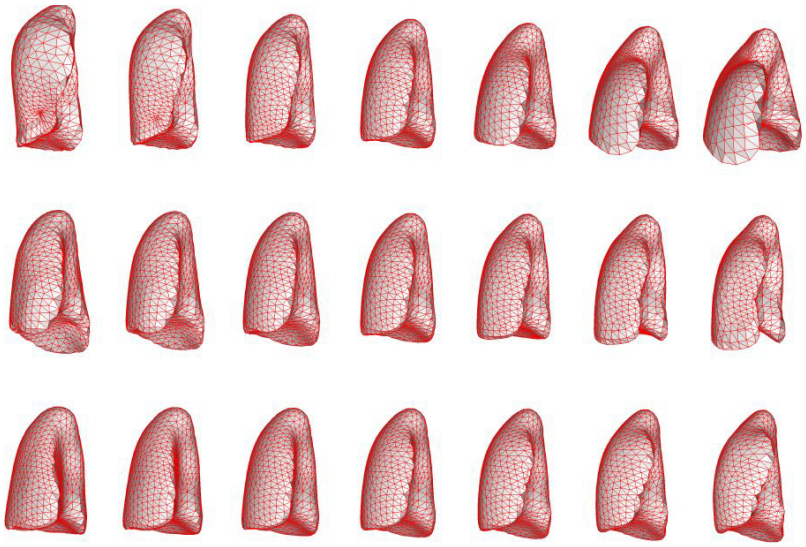

Fig. 5.23 Mean and strongest modes of variation of the right lung model.

The three strongest modes of variation are shown, top to bottom. Rows show the variation over three standard deviations.

Volumetry

For all time steps, the physical lung volume was calculated from the segmentation results as in equation (4.25). Segmentation quality and accuracy of the volumetry was evaluated against the simultaneously acquired spirometry data as gold standard. But, as the segmentation result incorporates a complete lung lobe in each case, thus also contains blood and tissue and not only the air volume, the calculated volume has to be calibrated to the actual breathing volume. However, calibration only has to be linearly, as the enclosed blood and tissue volume stays constant in first approximation over the breathing cycle, as it is additionally averaged over the acquisition time [112].

Therefore, the total segmented volume, which equals the sum of the single lung lobe volumes, was normalized against the spirometry data as follows:

$$V_{scaled} = \frac{(V_{measured} - V_{\min})}{(V_{\max} - V_{\min})}(V_{\max_{norm}} - V_{\min_{norm}}) + V_{\min_{norm}} \qquad (5.6)$$

Hereby, the indices *norm* apply to the target interval, *min* and *max* are the respectively smallest and largest volumes in the time series. It can be seen that the correctness of the assumption of a constant volume bias can be derived from the deviation of the linear correction factor $\frac{(V_{\max_{norm}} - V_{\min_{norm}})}{(V_{\max} - V_{\min})}$ from one.

Results

The volume curves calculated from MRI showed excellent agreement with the parallel obtained spirometric measurement for the coupled model approach, with a Pearson product-moment correlation coefficient of r=0.999 (one proband) and r=0.998 (two probands). The following two tables show the results of virtual spirometry for both tested approaches. The three figures afterwards show the volume-time curves of the probands.

Table 5-14 Experimental results of virtual spirometry using the deformable model approach

Proband / Deformable Model	Absolute volume error [ml]	Rel. volume error [%]	Correction factor
1	46.1±34.0	1.2±1.0	1.03
2	77.2±41.8	1.9±1.3	1.12
3	85.5±90.4	3.9±4.2	1.04
All (mean)	69.6	2.3	1.06

Table 5-15 Experimental results of virtual spirometry using the coupled model approach

Proband / Coupled Model	Absolute volume error [ml]	Rel. volume error [%]	Correction factor
1	34.8±27.2	1.0±0.8	1.04
2	89.5±73.1	2.2±1.9	1.13
3	74.1±80.9	3.5±4.1	1.04
All (mean)	66.1	2.2	1.07

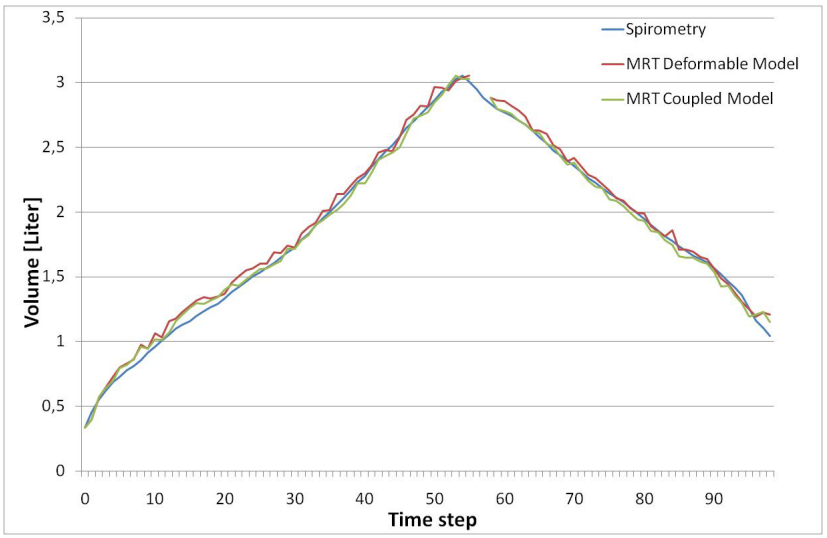

Fig. 5.24 Breathing curve for proband 1

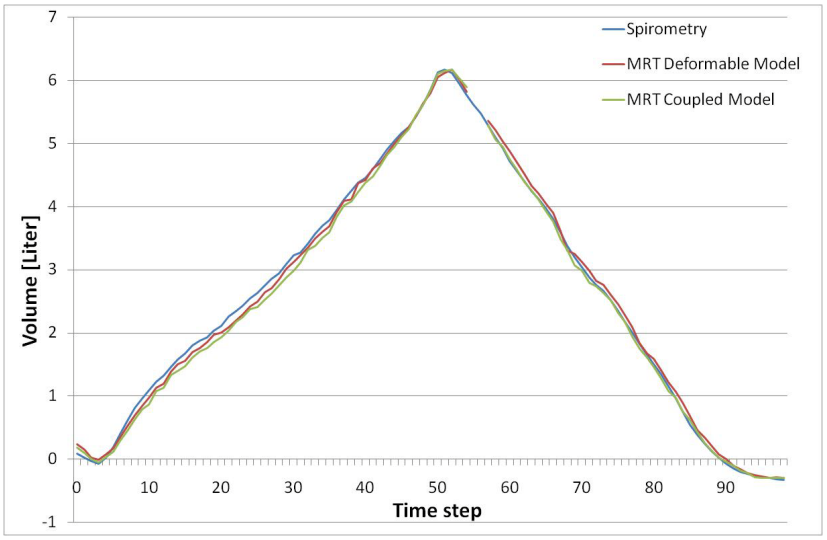

Fig. 5.25 Breathing curve for proband 2

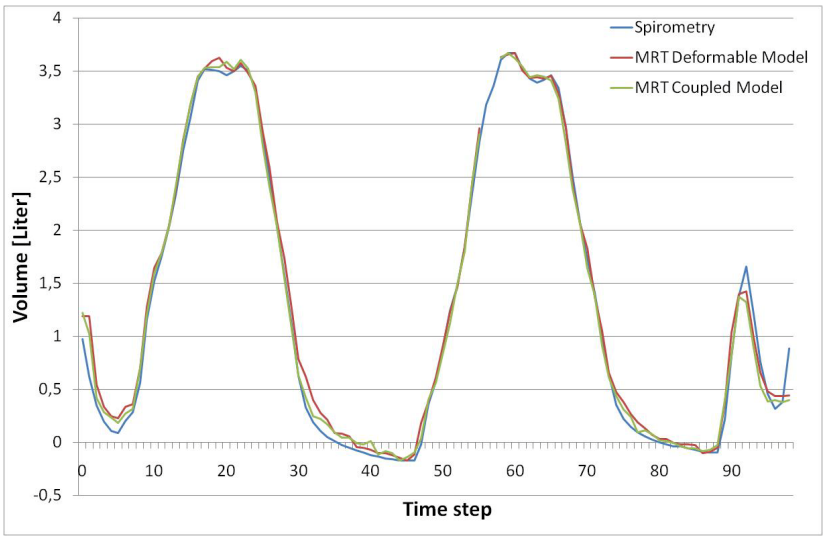

Fig. 5.26 Breathing curve for proband 3

5.7 Acquisition Plane Optimization

To evaluate the correspondence of 3D+t imaging (more exact) and 2D+t imaging (faster), the total error between volume calculation and area calculation depending on the acquisition plane angle of 2D+t imaging has been evaluated on six probands. The maps show the color coded error between volume and area over the complete time series, depending on the acquisition angle.

The calculated areas had to be calibrated for all time steps to allow a comparison to volumes as

$$A_{c,t} = \frac{(A_{measured,t} - A_{\min})}{(A_{\max} - A_{\min})}(V_{\max} - V_{\min}) + V_{\min} \qquad (5.7)$$

with $V_{\max}$ and $V_{\min}$ being the minimal and maximal volume over the time series. The total difference over a time series can then be calculated as

$$\Delta V(\theta, \Phi) = \sum_{t=0}^{t_{\max}} \left| A_{c,t}(\theta, \Phi) - V_t \right| \qquad (5.8)$$

The following graphs show the results displayed as color coded error maps depending on the acquisition angle. For better visibility, the inverted error is display, with red meaning low error, and blue

meaning high error (Fig. 5.27). Rotation around the y-axis (θ) means a rotation of the sagittal plane towards the transversal plane, around z-axis (Φ) means towards the coronal plane. In both directions, calculation has been done in steps of 1° each. Fig. 5.28 shows the mean error maps of the left and right lung, averaged over the six probands. For comparison, the errors have been normalized to a [0,1] interval for each proband. Table 5-16 gives the numbers for the error at worst corresponding, best corresponding, and sagittal plane.

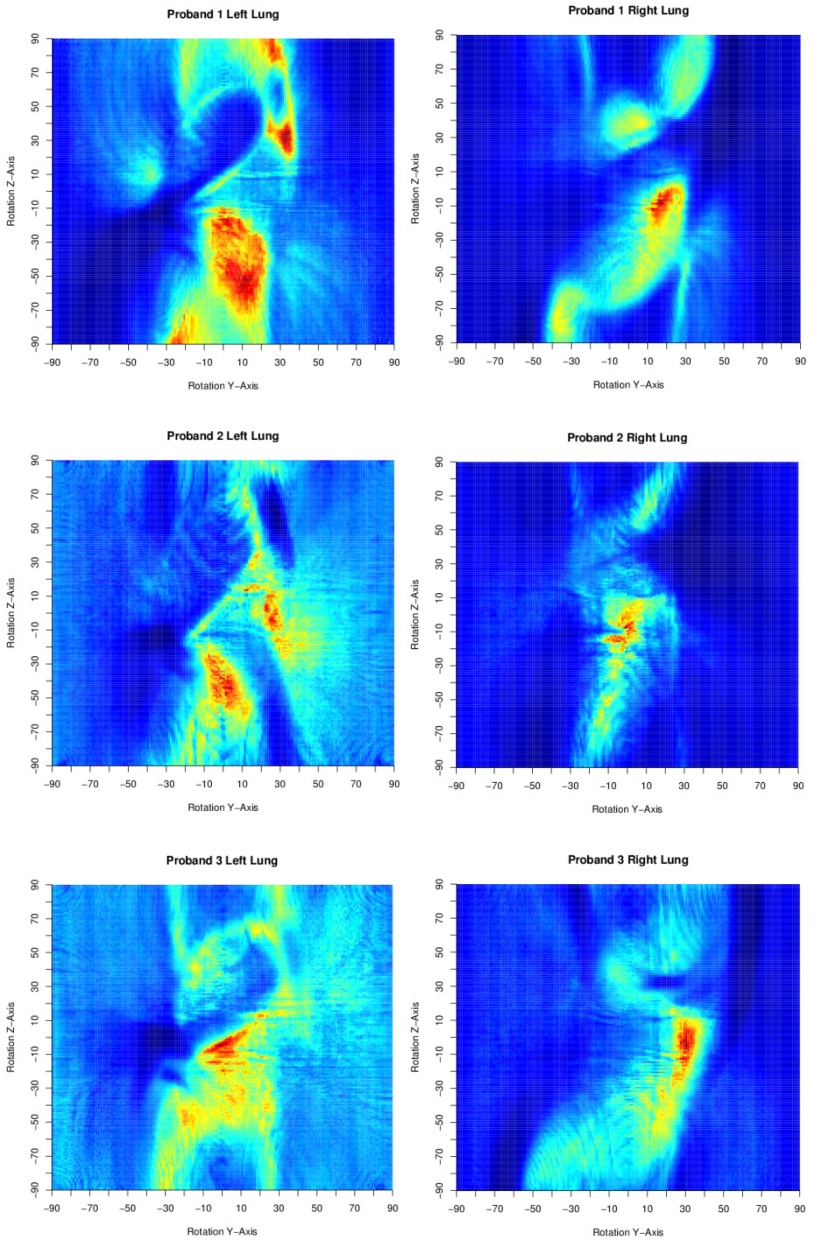

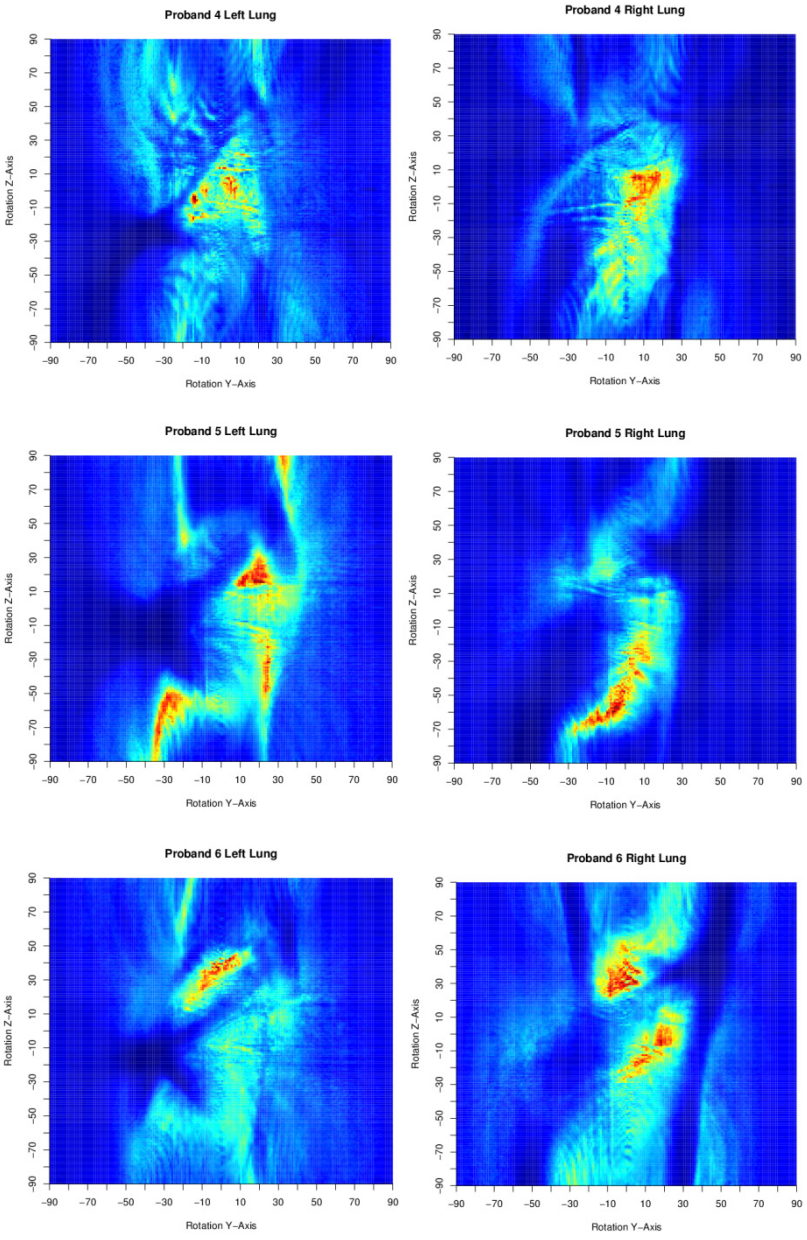

Fig. 5.27 Error maps of the six probands

The maps show the color-coded inverted error of lung volume between 3D volume measurement and 2D area measurement, depending on the orientation. Rotation is meant against the sagittal plane (see section 4.9). Red indicates lowest difference, blue indicates highest difference.

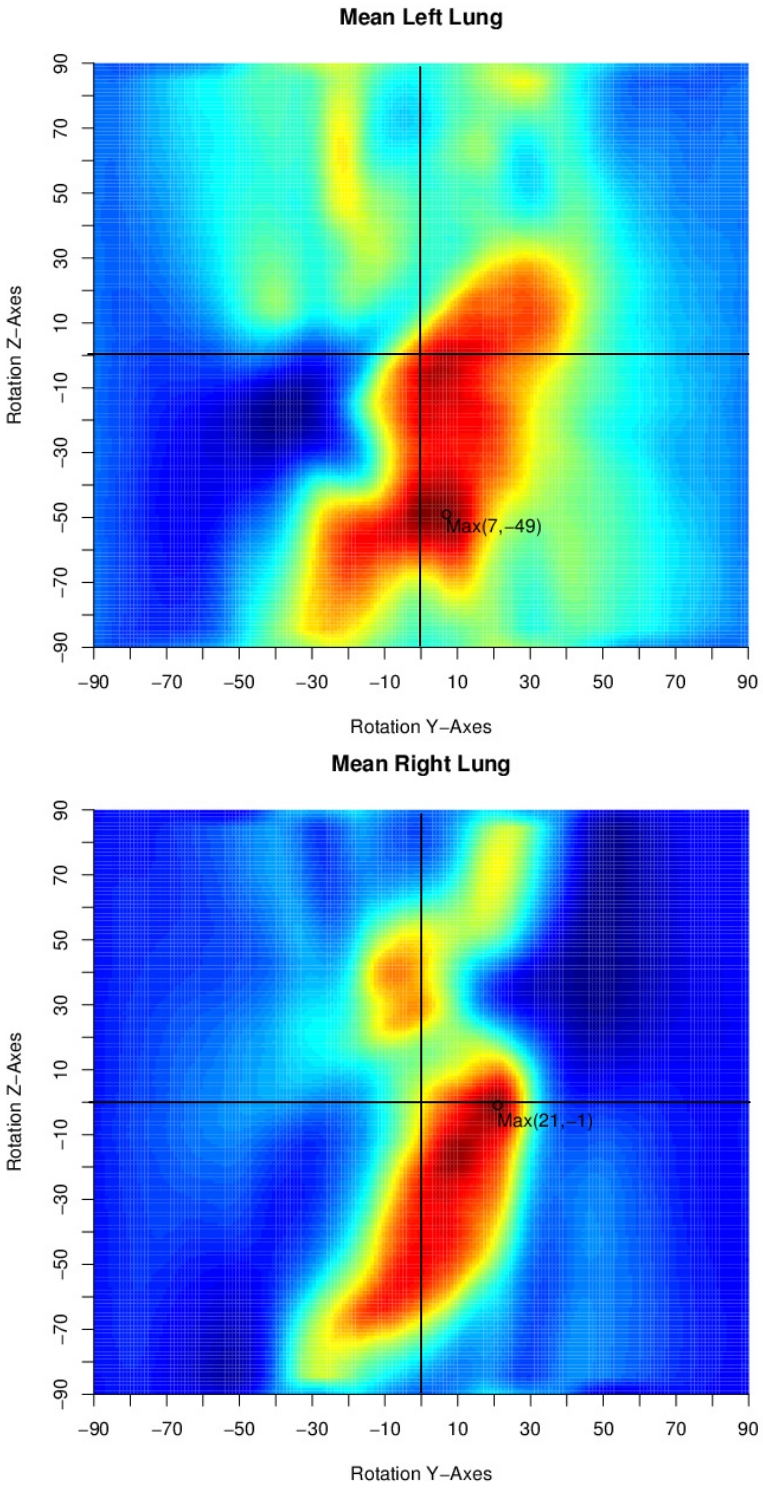

Fig. 5.28 Mean error maps of the left and right lung

See Fig. 5.27 for detailed description. Maps have been smoothed for better readibility.

Table 5-16 Correlation between 3D+t and 2D+t measurement

Mean deviation between volumetric and area measurement, in % of maximal volumetric interval. LL = Left lung; RL = Right lung; sag = sagittal image plane; min = worst correlation; max = best correlation.

Proband	min LL	max LL	sag LL	min RL	max RL	sag RL
1	15.90	1.63	4.05	24.45	1.28	5.09
2	13.25	1.21	2.96	18.69	0.78	1.10
3	14.43	2.31	4.14	21.19	1.38	5.57
4	25.32	1.29	2.69	18.94	1.25	1.88
5	18.73	1.47	3.86	32.15	0.98	3.04
6	24.75	1.32	3.46	28.90	1.33	3.73
Mean	18.73	1.54	3.52	24.05	1.17	3.41

5.8 2D+t Imaging Evaluation

5.8.1 Experimental setup

For imaging, a dynamic 2D fast low angle shot sequence was used (Flash 2D; repetition time/echo time: 2.47/1.03 ms; flip angle: 5°; parallel acquisition factor 2; field of view: 400 mm; matrix 128 x 128; slab thickness: 15 mm; temporal resolution: 8.5 images/second; imaging time: 47 seconds). Images were acquired from ten healthy volunteers in coronal orientation for simultaneous analysis of both lungs and in oblique sagittal orientation because previous results indicated that craniocaudal and anteroposterior thoracic diameter to be the most relevant determinants of lung volumes in two dimensions ([59, 113, 114]). The coronal images were acquired in true coronal orientation at the thoracic midline; the oblique sagittal images were planned on a line, reaching from the diaphragmatic dome to the thoracic apex while avoiding the mediastinum, resulting in a tilting of the image plane toward the midline. This tilting had to be more pronounced on the left because of the more prominent extension of the heart to the left (see last section).

Before acquisition of the dynamic 2D images, the spirometer was reset to baseline and the volunteers were asked to breathe through the spirometer mouthpiece. During imaging, the volunteers were guided to perform a FVC maneuver. The respiratory volume changes were recorded spirometrically with a temporal resolution of 10 ms.

5.8.2 Results

Images of all volunteers were of sufficient quality for semiautomatic segmentation. Mean time for the segmentation of one time series of a single lung was 191 seconds with a standard deviation (SD) of ±22. Spirometric data was successfully acquired during all measurements. Plotted as volume-time curves, a number of spirometric measurements showed seemingly linearly increasing deviations to lower volumes as can be seen in an extreme case in the bottom right curve in Fig. 5.29.

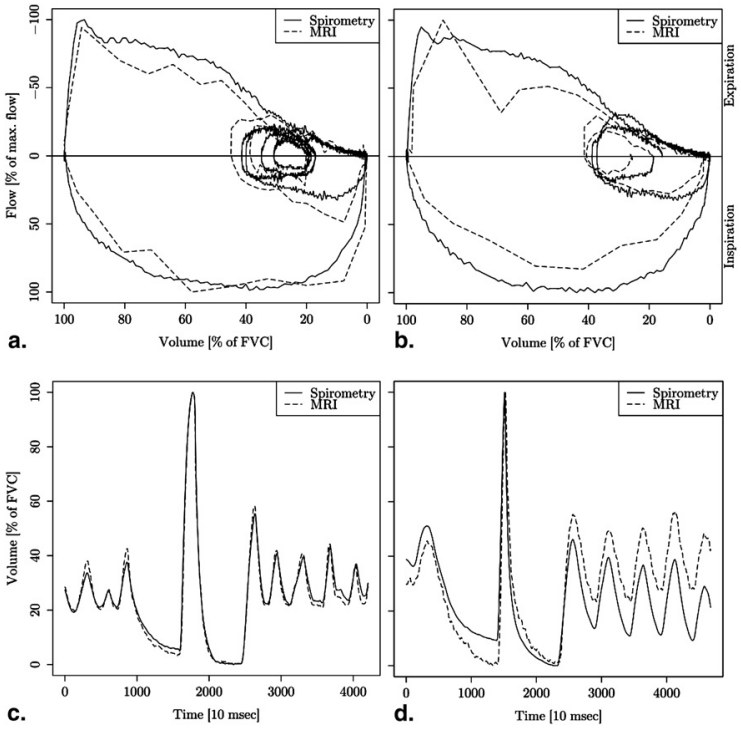

Fig. 5.29 Flow-volume and volume-time curves from spirometry and sagittal MRI

Results of four different measurements to illustrate differences of visual agreement. The left column (a, c) shows good visual agreement, the right column (b, d) worst visual agreement of all measurements with a concave shape of the expiratory loop that was not present in simultaneous spirometry. FVC = forced vital capacity.

The volume-time curves from MRI data were similar to the spirometric curves. The flow-volume curves from MRI showed similar characteristics to the spirometric curves with a sharp peak of the expiratory flow and a decrease of expiratory flow in parallel to the spirometric curve (top left of Fig. 5.29). In one case, the MRI derived flow-volume curve differed largely from the normal spirometric curve (Fig. 5.29b) and presented with a pronounced expiratory depression (expiratory coving) suggesting obstruction while spirometry was normal.

Pearson correlation of MRI area with spirometric volumes (Table 5-17) was very high with a mean correlation coefficient of 0.98 (SD 0.01) for the left lung in sagittal orientation, 0.99 (SD 0.01) for the right lung in sagittal orientation, 0.98 (SD 0.04) for the right lung in coronal orientation, and 0.97 (SD 0.05) for the left lung in coronal orientation. The only considerable lower correlation coefficients of 0.86 and 0.84 were found for the right and left of volunteer 6 in coronal orientation. Without this outlier (volunteer 6), the mean correlation coefficient for coronal measurements was 0.99 (SD 0.01) for the right and left lung and thus even higher than for the left sagittal measurement. A paired t-test found no significant differences of Pearson correlation coefficients between left and right lung or between measurements in sagittal and coronal orientation of the image plane (P value $\geq$ 0.14).

The Bland-Altman plots of the pooled data of all 10 volunteers showed more positive differences at lower respiratory volumes. Nevertheless, mean differences were below 1.1%. The 95% limits of agreement intervals extend below 8% to either side from the mean for right sagittal, below 10% for left sagittal, and below 11% for both coronal measurements. A one-sided t-test on the pooled data found significantly smaller absolute differences between spirometric and MRI-derived volumes for sagittal right measurement than for sagittal left measurement ($P < 10^{-15}$). Sagittal measurements were also significantly better than coronal measurements ($P < 10^{-15}$), whereas no difference was found between left and right coronal measurement (Table 5-18).

FEV1% calculated from MRI differed from spirometric FEV1% by a mean of 2.5% for sagittal right, 2.6% for sagittal left, 4.2% for coronal right, and 2.8% for coronal left images. The differences were be-

low 5% for all but one volunteer for both lungs in sagittal as well as coronal orientation. The largest differences in sagittal orientation of either lung were not reproduced in the coronal orientation and vice versa. As a measure of synchronicity between left and right lung motion, the time point when 20% of maximal expiratory flow was reached during the FVC maneuver on coronal images was calculated. It differed between left and right lung by a maximum of 50 ms on the interpolated MRI data.

Table 5-17 Product moment correlation coefficients

Product moment correlation coefficients of MRI area changes with spirometric volume changes for sagittal and coronal image orientation of the left and right lung. The large correlation coefficients show that the respiratory volume changes are well captured by measurement of the lung area on dynamic 2D MRI.

Volunteer	Right sagit-	Left sagit-	Right coron-	Left Coron-
01	0.99	1.00	0.97	0.98
02	1.00	1.00	1.00	0.99
03	0.98	0.99	0.99	0.98
04	0.99	0.99	0.99	0.98
05	0.99	0.99	0.98	0.98
06	0.97	0.96	0.86	0.84
07	0.99	0.98	1.00	1.00
08	0.99	0.99	0.98	0.99
09	0.99	0.98	0.99	0.99
10	0.97	0.97	1.00	0.99
Mean	0.99 (0.01)	0.98 (0.01)	0.98 (0.04)	0.97 (0.05)

Table 5-18 FEV1% calculated from spirometric and MRI measurement for sagittal and coronal imaging of both lungs

Abbreviations: FEV1% = first second of forced expiration; Vol. = volunteer; Spir = spirometric FEV1%; MRI = FEV1% as determined from magnetic resonance imaging; Diff = Spir – MRI; R and L = left and right lung the Values for Spir and MRI are Rounded, the Values for Diff are Calculated from the Original Data and are Rounded to the First Decimal

	Sagittal Right			Sagittal Left			Coronal				
Vol.	Spir	MRI	Diff	Spir	MRI	Diff	Spir	MRI R	Diff R	MRI L	Diff L
01	79	78	1.3	81	77	3.1	78	72	6.4	70	8.6
02	82	79	2.6	82	83	0.3	80	83	3.2	80	0.3
03	86	89	2.8	82	81	0.8	84	85	0.5	84	0.2
04	76	73	2.5	75	74	1.5	74	76	1.1	75	0.1
05	73	72	0.8	73	73	0.4	73	78	4.7	77	3.4
06	75	71	4.7	75	68	7.7	74	74	0	67	6.3
07	80	79	0.7	77	81	3.4	80	76	4.4	82	2
08	69	70	0.2	69	65	3.7	69	84	14.4	69	1
09	73	65	8.4	73	73	0.4	71	75	4.4	73	2.1
10	68	68	0.6	68	72	4.6	68	65	3.1	64	4.5
Mean (SD)			2.45 (2.5)			2.59 (2.39)			4.2 (4.1)		2.84 (2.88)

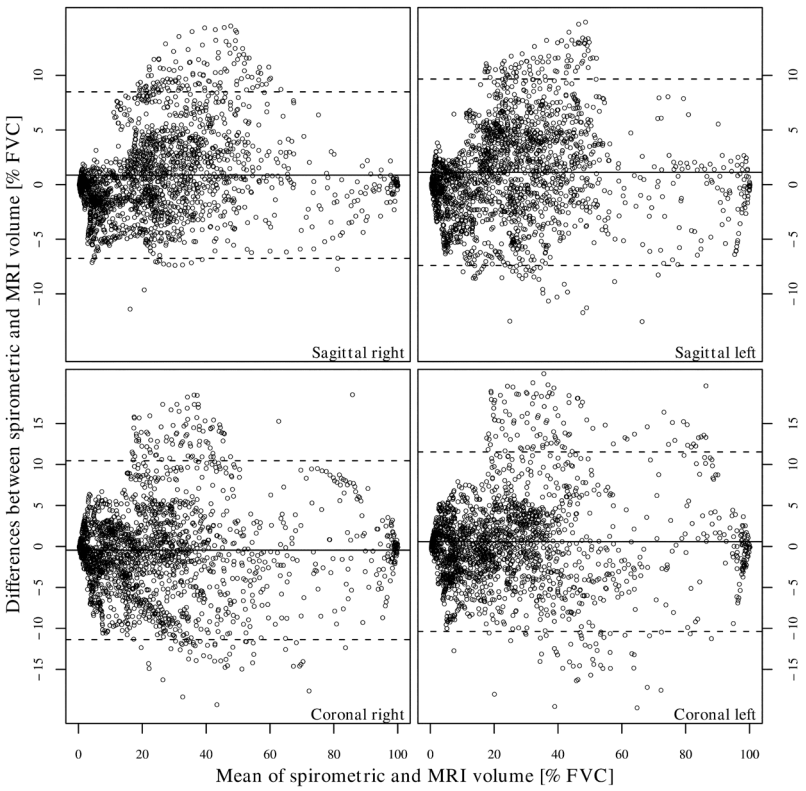

Fig. 5.30 Bland Altman plots of both lungs for sagittal (upper row) and coronal (lower row) measurements

The solid line indicates the mean difference between spirometric and magnetic resonance imaging (MRI)-derived volumes. The dashed lines show the 95% limits of agreement interval (mean ± 1.96 *SD [differences]). The figure shows that there is no large systematic difference between the two methods and that agreement is better for sagittal than for coronal measurement (width of the 95% limits of agreement interval. The larger differences for smaller lung volumes are probably from an artifact (see Discussion). For purpose of clarity, only every 20th data point was plotted. FVC = forced vital capacity.

6 Discussion

This chapter presents an in detail discussion of the experimental results shown in the last chapter. In the first part, the results in segmentation of heart and lung as well as the increase of segmentation accuracy by coupling multiple models are discussed. The second and third part deal with the generation of medical diagnostic parameters from the segmentation results for the computer aided detection of motion restriction of the heart and lung, respectively.

6.1 Segmentation

First of all, the single deformable shape model was tested for its applicability for segmentation of the left ventricular endocardium in 3D images of the hearts end-systole and end-diastole. These images show relatively good contrast and clear borders of the endocardium. The model thereby showed the capability to rapidly and robustly detect and segment the left heart ventricle, with a segmentation time of less than a minute for each image. Volumetric parameters like stroke volume and ejection fraction can be directly generated from the results, the model is therefore applicable in a wide range of clinical applications in diagnosis and therapy aid. The free deformation terms used in the approach help to better adapt the shape model to the given data than a model strictly constricted to trained shapes. Given a mean segmentation error of 0.95 mm for end-diastole and 1.69 mm regarding average surface distance, this is already sub-voxel accuracy. The error distribution diagrams (Fig. 5.1 and Fig. 5.4) also show that in some cases outliers in segmentation quality show up, three in the case of end-diastole, and two in the case of end-systole, always originating from a leaking of the model into the aorta due to mis-segmentation of the valvular plane. With the possibility of a fast manual correction as evaluated in section 5.4, the results can quickly be increased to a much lower average error. A relative volumetric error of 12.4 % seems fairly high, but compared to the error of 8.4 percent between two different gold

standards, manual segmentation and direct measurement, used for the same evaluation, it can be considered as acceptable because of the largely reduced time effort using the automated method.

According to experience, it is difficult to compare results of shape model segmentation using different test data, as the models are almost always specialized for a certain purpose derived from the data, and developed techniques aim to fulfill this purpose. The model introduced by van Asses et al. [110], for example, is particularly suitable for sparse volume data.

Nevertheless, the segmentation results achieved by the model perform better in terms of average surface distance error than prior approaches.

Segmentation of the lung from 3D MRI has been already evaluated earlier by [82], resulting in an average surface distance error of 2.3 mm and a relative volume error of 2.3 %.

When applying the deformable model to dynamic 3D+t MRI data, anyhow, the segmentation quality drops severely. Because of the high temporal resolution given in these images which is necessary to capture organ motion, the data suffers from a reduced spatial resolution, lower signal-to-noise ratio, and recurring image artifacts. For the left ventricular endocardium, this results in an increase of average surface distance error to 3.7 mm, and 3.8 mm for the epicardium. Therefore, several methods of model correlation presented in section 4.3 have been evaluated to show that a model coupling can increase segmentation results.

In all methods, with deformable as well as coupled models, the endocardial model tends to misleadingly converge to the papillary muscles instead of the ventricle wall in images of a systolic heart phase or close to it. This is especially true for the deformable model, where two segmentations almost completely failed, leading to a very high segmentation error of over 5 mm average surface distance. This gets better for the common shape space methods, as the epicardial model “pulls” the endocardial one further to the true ventricle wall. Overall, both common shape space methods generate better segmentation results than the single models in terms of average error of both endocardial and epicardial results. For the epicardium, the severe drop in terms of standard deviation also indicates a

more robust and reproducible result for all coupled shape space methods. The methods with relaxed parameter application, anyhow, only show an improvement in one of both cases, and generate even worse results than the deformable model in the other case. The joint shape space approach with relaxed parameters shows a good segmentation result for the epicardium, but a slightly worse result for the endocardium. The unified relaxed approach only shows a good result of the endocardium, but the worst result of all methods for the epicardium. This mis-segmentation problem shows in all datasets and seems to be a systematic error which has to be further investigated.

The approaches with strict common shape parameter application are clearly superior for the used data. Here, the average segmentation error is far below one image voxel diagonal (5.5 mm). This can also be seen in Fig. 5.9: Both approaches with strict coupled parameters show a good segmentation result compared to the manual generated gold standard. What can be seen in Fig. 5.9, too, is a common problem of the single models: The segmentation of the endocardium does not correctly detect the mitral valve plane and hence under-segments the ventricle. Large portions of the segmentation error comes from misdetection of the mitral valve plane because of the z-spacing of 5 mm compared to 1.6 mm in the other directions, so a displacement in z-direction leads to a much larger error. In the coupled methods, the endocardial segmentation is pulled to a more correct position by the epicardial model.

The joint shape space methods show overall better results than the corresponding unified shape space methods, so it seems to produce better segmentation results when all objects are treated as a single entity, instead of applying a correlation force term to the single models. The best method, using a joint shape space with strict parameter application, reduces the average surface distance error by 37 % in average compared to the single deformable models, showing an error of 2.54 mm for the endocardium, and 2.14 mm for the epicardium.

It could also be shown that a geometrical correlation of the heart walls improves the segmentation results compared to the single deformable models. The geometrical coupling alone generates results between the single models and the best method of coupled

shape models. Using the geometrical and joint strict force terms together, although the segmentation error is with 2.49 mm for the endocardium and 2.21 mm for the epicardium comparable to using the joint strict method alone, the slight drop in volumetric overlap error from 13.2 % to 12.8 % can be observed. As both coupling methods tend to increase segmentation quality in the same problematic areas, at the valvular plane, the apex, and on local imaging artifacts, it is assumed that both methods produce comparatively coinciding results for landmark positions when used together.

The possibility of a manual correction of segmentation errors can further support a good result. For the heart, as can be seen from Table 5-8 and Fig. 5.13, the tool allowed for correction of the leaking out of the segmentation at the mitral valve, which could be corrected in fewer than two minutes.

In the case of the liver, the segmentation was only improved to a limited extent (Table 5-9 and Fig. 5.14). But, the standard deviation of the error is significantly decreasing, as it is in the heart case. This is due to the reduction of statistical errors, leaving only behind a mostly systematical error. This error results in the liver case from the exclusion of the major vessels in the liver in the manual segmentation, which are included in the automated case and for whose exclusion the interaction tool is neither intended nor useful.

Compared to the image resolutions normally present in dynamic data, the remaining error with the presented methods is considerably lower than a voxel diagonal and in the magnitude of inter-observer variability (the variability when two different experts make the same measurement). The error distributions of the best evaluated methods, given in Fig. 5.8 and Fig. 5.11, show that two third of the results have an average surface distance error of below 2.5 mm, which is half of the image's z-spacing, and is thereby low enough to allow computer aided diagnosis of motion restriction.

6.2 Cardiac Motion Analysis

It was shown that segmentation with coupled models can achieve sufficient accuracy of segmentation even on noisy and low-resolved cardiac images. Due to the improved segmentation quality using coupled models, as presented in the last section, it was possible to improve the cardiac volumetric parameter generation. The parameters stroke volume, ejection fraction, cardiac output, cardiac index, and wall mass directly depend on the endocardial and epicardial volumes as listed in section 2.4, the volumetric error as shown in section 5.3.2 is a direct measure for the error of cardiac diagnosis for these parameters. Due to the improved segmentation quality, it could be dropped from 29.3 % average to 17.1 % for the endocardium, and from 18.7 % average to 8.6 % for the epicardium, compared to the single deformable models.

As the segmentation result are two surfaces, endocardium and epicardium, with inherent landmark correspondences, the important cardiac parameters wall motion, wall thickness and wall thickening could be easily calculated and projected to the developed Bull's Eye diagram. As the Bull's Eye diagram is temporally resolved, it also allows a more detailed analysis and visualization of these parameters over the heart cycle, which can intensively help in cardiac diagnosis. It might as well be also used to calculate more advanced parameters like asynchrony [11].

The error coming from the interpolation steps when projecting from a surface to a 2D plane is with an average of 0.51 mm small compared to the remaining segmentation error (see last section). One must note that this error is a worst case estimate, as it is calculated by projecting discrete values, which do not occur in real cardiac image data, but lead to a high interpolation error at borders, and can therefore be neglected in most clinical questions. The error from wall thickness and thereby wall thickening calculation between surface landmarks was evaluated and showed to be very low, with 0.08 mm in average for wall thickness, and can therefore be neglected, too.

The evaluation of wall thickness and wall thickening calculation against a manual obtained measure from a medical expert on patient data showed that the use of coupled models can decrease the

error somewhat, but it is still quite high with an average of 1.93 mm for wall thickness calculation and 2.75 mm for wall thickening calculation, which is still quite large compared to a range of wall thicknesses between 5 and 20 mm as they usually appear in anatomy over the heart cycle. The problem here is the comparison of measures obtained in different frames of reference. The medical expert only measures in two orthogonal planes which are aligned by definition relative to the heart axis, and only obtains three measures in 2D space which are averaged. The average measures calculated from the surface resulting from segmentation is calculated in 3D and is averaged over a large number of values from a region. A measurement of thickness in 2D is only absolutely correct when the heart wall is perfectly perpendicular to the plane in which is measured, which will almost never be the case in patient data. Therefore, although the manual delineation is regarded as gold standard, the measurements calculated from the segmentation results are presumably closer to real anatomic conditions and a large portion of the remaining error results from the measurement in 2D. Wall motion could not be evaluated as it is very difficult to observe without segmentation and can thereby not easily be measured manually. Even with a manual segmentation, it is very hard even for a medical expert to identify corresponding anatomical points in different time steps.

Overall, the evaluation showed that the developed methods show sufficient accuracy to support computer aided diagnosis of the heart function. It is assumed that the methods generate better results than a manual measurement in 2D, which can be further improved by continuing developments.

6.3 Respiratory Motion Analysis

6.3.1 3D+t Respiratory Motion Analysis

The methods developed in the scope of this thesis for the quantification of lung volume over the breathing cycle showed the potential to measure the respiratory function individually for each lung in a non-invasive manner. The most commonly used methods of thoracic image acquisition, thorax CT and MRI, are applied static, and it has been shown in previous works that these are able to generate static measures of lung volumes (see e.g. [115]). In contrast, the proposed methods are able to also generate dynamic quantification of lung function under normal breathing and breathing maneuvers that are not too fast. The benefit of this, together with the possibility to measure both lungs individually, is that even minor changes in respiratory dynamic can be monitored at an early stage. Surface rendering of the segmented images with visualization of temporally resolved deformation fields also enables a detailed qualitative assessment of free-breathing 3D+t lung motion, which could never have been achieved with either free-breathing dynamic two-dimensional images or breath-hold 3D images acquired at multiple respiratory phases.

Due to the technical development in MRI allowing for image acquisition within 0.5 seconds, it could be shown that from 3D+t image segmentation a breathing curve with significant correlation to conventional spirometry can be generated under normal breathing and slow breathing maneuvers from inspiration to expiration. The utility of a temporal resolved model approach reduces user interaction to a minimum and actually initially allows for a qualitatively high 4D analysis with high temporal resolution, as a manual delineation of a time series is not practicable because of the time effort, and low level segmentation methods can in general not achieve a sufficient segmentation quality at the given spatial resolutions and signal-to-noise levels.

Surprisingly, the coupling of both lungs using the joint shape space method with strict parameter application, which greatly increased the segmentation quality in case of the heart ventricle, did not lead to a significant increase of the correlation of the volume curve with spirometry. Although for two probands the correlation was some-

what increased, for one proband the results were inferior, so only a slightly average decrease in error was found, from an absolute mean error of 69.6 ml to 66.1 ml deviation. This is most likely due to systematic errors that both methods share, namely the undersegmentation of the lung's tips, which leads to a volume bias depending on the breathing state. These errors originate in the smoothness restrictions both methods share, which do not allow for the creation of spikes into the lung tips, but are essential for an anatomically valid result in most image areas.

Anyhow, the correlation of virtual spirometry to conventional spirometry has been shown to be very strong. With a relative volumetric error of only 2.2 %, this shows that the method is suitable for diagnostic purposes. It could also been shown that the influence of tissue and blood when comparing calculated lung volumes and measured flows is very small. Assuming a linear correlation, a constant volume bias would lead to a linear correction factor (slope) of 1.0. It could have been shown that the factor only marginally deviated from 1.0, so a constant volume bias can be assumed in good conformance.

The quantification of forced breathing maneuvers and thereby many dynamic parameters with the developed methods have shown to be not possible due to the temporal resolution of image acquisition. For these, methods for faster 2D+t imaging have been developed as discussed in the next section. Anyhow, independent from these the developed 3D+t measurements can generate valuable information for quantification in diagnosis and therapy monitoring, and this at an early stage of progress where conventional spirometry cannot measure restrictions or therapy response, because local impairments tend to be compensated by the other lung. Due to the calculation of surface motion at each point and the interpolation of inner motion from the surface motion, it was made possible to also get information about local motion restrictions. The calculation of a compliance map allows for an early stage local assessment of lung function. Given the diagnosis of a motion restriction, it can be further quantified by 2D+t imaging.

6.3.2 2D+t Respiratory Motion Analysis

By measuring lung area changes on dynamic 2D MRI, it was shown that it is possible to assess lung function of single lungs with good agreement to spirometry. Apart from the post-processing software, the technique does not require special hardware and can be easily adapted to different MRI machines. With about 3.5 minutes, the post-processing time is short in comparison to standard techniques. The previous evaluations by semiautomatically measuring thoracic diameters took at least 10 minutes for one lung [61], another group used manual segmentation without indicating their post-processing time [55]. With the newly developed approach based on graph cut segmentation, the post-processing time could easily be further reduced. Apart from the last step of user interaction, the visual control and manual correction of the segmentation result, the area measurement can be automated. This would cut the post-processing time down to less than 1 minute per lung. The volume changes were plotted as volume-time and flow-volume curves (see section 2.7.3) as these are the standard graphical representations of spirometry. In most cases, the curves from MRI and spirometry were almost identical, even the most deviating curves from MRI preserved most of the characteristics of the corresponding spirometric curves, especially the sharp expiratory peak in the flow-volume curves (Fig. 5.29). Spirometric volume-time curves often showed a progressive linear downward deviation that suggested a constant drift in spirometric measurement (Fig. 5.29d). The systematic larger positive differences between MRI and spirometry visible in the Bland-Altman plots also point in this direction, as data from cyclic breathing at smaller volumes was acquired mostly after the FVC maneuver. A spirometric downward drift would thus have led to larger positive differences at these lower volumes. For this reason, a linear correction could be considered. But most spirometric measurements also included breath holds before or after the MRI measurement and spirometric volumes remained constant during these time periods. This excluded a technical cause for a spirometric drift. A possible explanation for this progressive and seemingly systematic deviation is that the volunteers did not tightly seal their lips around the mouth piece, drawing in some air from the side during inspiration. The larger difference between MRI and spirometry in the flow-volume curve of the sagittal measurement of volunteer 9 (Fig. 5.29b) oc-

curred only in a single volunteer. It was reproduced by repeating the segmentation and seemed to be a real feature of the image series. The normal spirometric curve and FEV1% suggest that this is an artifact introduced by the limitation of a 2D measurement. An explanation could be that during this measurement the volunteer emphasized the contraction of the abdominal muscles at the beginning of forced expiration. This would have caused an overestimation of the expired volume because the diaphragmatic action is overweighed in the 2D measurement relative to the thoracic diameter (Fig. 5.).

The quantitative evaluation of differences between spirometry and MRI asserted the good agreement indicated by the visual representations. Pearson product moment correlation was extremely high with mean correlation coefficients above 0.97 and thus even higher than found in previous publications by Plathow ($r = 0.93$), and Kondo (r approx. 0.93) [59, 113] and previous evaluation on thoracic diameters ($r = 0.93$) [61].

Surprisingly, when evaluating previously published data on chest wall diameters [61] with the automatic synchronization by cross correlation, no advantage could be found for the measurement of lung area as was the original hypothesis, indicating that the improvement of correlation results from more precise temporal synchronization. However, it has to be noted that the present evaluation only included healthy subjects with homogeneous movement of thoracic wall and diaphragm. In patients with thoracic deformities or changes of diaphragmatic mobility, the area measurement should still have advantages over assessment of thoracic diameters. The automatic synchronization by cross correlation could itself influence the results because any systematic offset between the data measured by spirometry and MRI will be eliminated. If such an offset were introduced by the measurement equipment, this would be a desirable effect because the offset would not have any physiological meaning. If an offset were caused by disease, the synchronization would indeed suppress interesting information, the comparison of the volume movements would nevertheless remain valid and differences in volume changes would still be visible in the evaluation.

In any case, for measurement of one-sided delay of respiratory motion, evaluation of coronary imaging would be most appropriate because it provides intrinsically synchronized measurements of both

lungs. By automatically calculating FEV1% from the measurements, we wanted to avoid bias from a human observer defining the beginning of expiration. The choice of starting at 20% of maximum expiratory flow was chosen somewhat arbitrarily, but no description of automatic calculation of FEV1% exists in published literature, so the lowest flow value that found similar starting points in MRI and spirometry was chosen. With most differences between MRI and spirometry below 5%, the mean difference for sagittal imaging of about 2.5% and a standard deviation of about 2.5%, the two measurements methods give comparable results. The largest differences of 14.4% for right coronal measurement was checked several times and corresponded to a markedly steeper MRI derived expiratory volume-time curve for this lung, which was not obvious from visual inspection of the image series. The only apparent possible cause was an asymmetric motion of the heart, which moved faster into the imaging plane on the right side than on the left and probably caused the faster decline in segmented lung area on this side.

The latter fact points to the big influence of the choice of the imaging plane for correct measurement of lung function through 2D MRI. Which orientation to choose for measuring function of individual lungs has not been thoroughly investigated yet. Previous studies on respiratory changes of thoracic diameters found the craniocaudal diameter to correlate best with spirometry with the anteroposterior diameter second best and the lateral diameter least important [113, 114, 116]. This led to a primarily consideration of the sagittal plane for lung function measurement. The results of the measurements here confirm the superiority of the sagittal plane over the coronal measurement. This is especially true for the right lung, where it is easy to choose a plane without in and out of plane motion of the heart. But the differences between the other imaging planes are not large and, on the other hand, the coronal plane allows imaging of both lungs at the same time. This simultaneous measurement of both lungs eliminates variation between consecutive respiratory maneuvers and should make detection of differences between left and right lung easier. Certainly, at the present state of development, the large side-differences found in some volunteers could still lead to a false diagnosis of one-sided lung disease. But errors in one evaluation (e.g., on coronal images) are not likely to be reproduced in a second measurement with a different image orientation. There-

fore, a combination of the measurement in two orientations could be used to limit false-positive results.

The measurement in the coronal plane can additionally give information about the synchronicity of the respiratory motion of the two lungs. This can be useful for quantification of diaphragmatic paresis or of functional diaphragmatic insufficiency in patients with scoliosis or thoracic deformation. The maximal difference of 50 ms found in this study that was calculated on the temporal interpolated MRI data is well below the temporal resolution (117 ms per image) and thus shows synchronous respiratory action in all volunteers, which agrees with the results published by Kiryu et al [117].

The developed method still has several limitations. Most important, because fast dynamic MRI only provides 2D data, the measurements had to be transformed to percentages of FVC for comparison with volumetric spirometry. To allow for real volume measurements at full temporal resolution with the developed method, an area-volume mapping function would be necessary, which most likely would have to be patient specific. Another limitation is the comparison of single-sided MRI measurement with global spirometry. In the study population of healthy volunteers, this is not considered to be a major limitation because lung motion can be expected to be synchronous, but would be a more serious limitation when trying to validate measurements in patients with pulmonary disease. Here, again an agreement with global and lung individual volumetry from 3D+t measurement would have to be found.

Overall it can be said that measurement of lung area changes on 2D MRI allows for spirometric measurement of single lungs with good agreement to conventional spirometric measurement. With the short postprocessing time of semiautomatic segmentation, it is easily applicable in a clinical context and thus provides a possibility to increase sensitivity of functional measurement in cases of inhomogeneous distribution of lung disease and of one-sided diaphragmatic weakness.

6.3.3 Acquisition Plane Optimization

As stated in the last section, the choice of the image acquisition plane has a large influence on the correlation of conventional spirometry and area measurement. First of all, the chosen plane must

show all aspects of the breathing motion as good as possible, which is comprised of diaphragmatic and thoracic movement. Secondly, the influence of the heart must be respected, which moves in and out of the imaging plane during the heart cycle.

Also, as mentioned previously, it has not yet been evaluated whether the sagittal plane is optimal for functional measurement, although it is commonly used in imaging.

Examining the simulated image acquisition planes under the aspect of correlation between area measurement and volume calculation over the complete time series for each of the six probands and the mean result, several observations can be made.

In general, the error depending on plane orientation shows considerable local differences on the individual probands, but show a similar global pattern for both lungs. Both lungs show a band of low error between sagittal and coronal orientation within about ± 30° orientation against transversal. This is in good accordance with theory, as in transversal orientation, diaphragmatic movement cannot be monitored, which contributes most to breathing motion. It also shows from the mean motion map that the sagittal plane gives good results with an error of approximately 3.5% on both lungs, but is not the best choice. For both lungs, this error can be reduced by 60% and more with the choice of the best corresponding plane.

Anyhow, to make a universally valid proposal for a best applicable acquisition plane, an evaluation on six probands does not give enough data basis. Especially, it must be researched how plane orientation influences area calculation and volumetry correspondence on patient collectives showing typical motion restriction patterns. The results from this evaluation give a good basis and motivation for investing more research in this topic.

7 Summary

In the course of this thesis, various methods for an automated analysis of motion restrictions of the heart and lungs were developed. A high priority in the development of these new or improved techniques was in the clinical applicability of the approaches. This makes high demands on the developed algorithms. The reproduction of examined anatomic structures must be as high as possible, generated quantitative parameters must be as exact as possible, and the algorithms must produce results fast and with low user input necessary.

For both the analysis of heart and lung motion behavior, the extraction of relevant structures is a premise. The results of the analysis are thereby directly affected by the segmentation quality. Also, segmentation can be a major bottleneck in computer aided diagnosis. In case of the temporally resolved image data treated in this thesis, a manual segmentation approach is nearly inapplicable due to the vast amount of data and the hence resulting time effort. Therefore, an automated approach based on coupled shape models was developed in this thesis, with which several structures of interest can be segmented simultaneously. The approach utilizes mutual information between correlated structures to cope with the problems typically arising in 3D+t image data, namely low spatial resolution, low signal-to-noise ratio, and recurring image artifacts. Correlation methods aiding the segmentation have been developed to automatically initialize models from each other, and to exploit mutual information of geometry and shape during the segmentation search to support and correct the particular structure's segmentation in difficult image areas.

The best of several tested methods leads to a decrease of segmentation error of approximately 40% for the endocardium and epicardium, and leaves a remaining volumetric error of below 13%, which is in the magnitude of inter-observer variability. The developed cardiac dynamic analysis based on the segmentation technique using a

temporally resolved Bull's Eye diagram offers a much more detailed analysis of cardiac mobility over the whole heart cycle than standard methods only regarding end-systole and end-diastole and is unique in literature. The incorporation of temporal information is an intuitive extension of standard analytic methods and thereby easy to integrate into clinical routine.

For the lungs, only very few methods for the local characterization of lung function and mobility can be found in clinical practice. Given a volumetric calculation accuracy of below 70ml mean error that could be achieved in volumetric calculation from segmentation of dynamic 3D+t MRI, which showed excellent correlation with conventional spirometry (Pearson correlation coefficient r=0.998) in normal breathing and slow breathing maneuvers, the information obtained from the images can be a valuable support in computer aided diagnosis. Contrary to spirometry, which only delivers global breathing volumes, the developed method is also able to quantify breathing volumes for each lung individually. Also, as spirometry is not very sensitive to single sided changes in lung function, the developed methods can deliver support in the detection of early stage diseases and in therapy monitoring, and can additionally provide information on medically problematic areas via the calculation of local deformation vector fields.

For the calculation of dynamic lung volumes like e.g. forced vital capacity or forced expiratory volume in one second under standard forced breathing maneuvers, a method for the quantification of respiratory function based on graph cut segmentation of 2D+t MRI data was developed. It could be shown that measurement of lung area changes for spirometric measurement of single lungs is in good agreement with conventional spirometry (Pearson correlation coefficient r=0.98). It was further evaluated which acquisition plane is best to be used for local spirometry, resulting in the commonly used sagittal plane showing good results for the task, but the plane orientation might be improvable. Further research with patient collectives showing common restrictive pattern could presumably give a universally valid proposal of a most suitable acquisition plane orientation.

In conclusion, the essential contributions of this work are:

- Novel methods to utilize mutual shape information to improve model based segmentation of multiple correlated objects
- A novel method to utilize mutual geometric information to improve model based segmentation of multiple adjoining objects
- A fast correction possibility for erroneous segmentations
- Implementation of a comprehensive temporally resolved analysis method for the local dynamics and volumetry of the left heart ventricle
- Development of a method to individually analyze both lungs and to characterize regional lung motion behavior from 3D+t MRI, and new visualization methods for this purpose
- Development of a graph cut segmentation scheme that allows highly temporal resolved analysis of breathing behavior from 2D+t MRI
- Analysis of the impact of acquisition plane orientation in 2D+t MRI on the correlation with breathing motion

8 Outlook

A thesis can only follow a limited amount of ideas and directions, and even those can sometimes not be explored until the last detail. Below is a list of future work, arising from the observations in this thesis:

- The developed coupling methods could be further evaluated on other structures of interest in the body, and on images of different modalities
- The developed coupling methods showed different behavior on different local image conditions. A hybrid approach of the methods using a weighting scheme to determine the influence of each method based on local condition could be of interest
- The combination of the used methods with information obtained from other imaging modalities could be of great value
- The dependency of 2D+t virtual spirometry on acquisition plane orientation should be further evaluated on patients showing common breathing motion restriction patterns

References

[1] WHO. The top 10 causes of death. In: World Health Organization; 2004, updated 2008.
[2] Huch R, Fessel D. Mensch, Körper, Krankheit. München; Jena: Elsevier, Urban & Fischer; 2007.
[3] Gray H. Anatomy of the human body: Lea & Febiger; 1918.
[4] Heart with coronary arteries. Available at http://info.med.yale.edu/intmed/cardio/imaging/anatomy/ant_heart_2/index.html; Last seen online: 11/20/2010
[5] Rietdorf U. Computergestützte Operationsplanung zur chirurgischen Korrektur angeborener Herzfehler. In: Faculty of Medicine. Heidelberg: University of Heidelberg; 2010.
[6] Heart blood flow diagram. Available at http://en.wikipedia.org/wiki/File:Heart_diagram_blood_flow_en.svg ; Last seen online: 11/20/2010
[7] Dorland. Dorland's Medical Dictionary: Saunders; 2007.
[8] Fozzard HA. The Heart and cardiovascular system: scientific foundations: Raven Press; 1986.
[9] Sauer A, Schwarz T, Engel N, Seitel M, Kenngott H, Mohrhardt C, Loßnitzer D, Giannitsis E, Katus HA, Meinzer HP. Quantitative Analyse und Visualisierung der Herzfunktionen. BVM l2009.
[10] Beers MH. The Merck Manual of Diagnosis and Therapy. 18th edition ed: Merck; 2006.
[11] Wesarg S. Automatisierte Analyse und Visualisierung der Koronararterien und großen Kavitäten des Herzens für die klinische Anwendung. In: TU Darmstadt, Fachbereich Informatik; 2007.
[12] Termeer M, Bescós JO, Breeuwer M, Vilanova A, Gerritsen F, Gröller ME. CoViCAD: Comprehensive Visualization of Coronary Artery Disease. IEEE Transactions on Visualization and Computer Graphics (accepted for publication) l2007;13.
[13] ASNC. ASNC Imaging Guidelines for Nuclear Cardiology Procedures. J Nucl Cardiol l2006;13.
[14] Cerqueira MD, Weissmann NJ, Dilsizian V, Jacobs AK, Kaul S, Laskey WK, Pennell DJ, Rumberger JA, Ryan T, Verani MS. Standardized Myocardial Segmentation and Nomenclature for Tomographic Imaging of the Heart: A Statement for Healthcare Professionals from the Cardiac Imaging Committee of the Council on Clinical Cardiology of the American Heart Association. Circulation l2002;105: 539-542.

[15] Mintz ML, Person A. Anatomy and Physiology of the Respiratory Tract. In: Skolnik NS, editor. Disorders of the Respiratory Tract: Humana Press; 2006, p. 11-15.
[16] The complete respiratory system. Available at http://en.wikipedia.org/wiki/File:Respiratory_system_complete_en.svg; Last seen online: 11/20/2010
[17] Breathing muscles. Available at http://people.eku.edu/ritchisong/301notes6.htm; Last seen online: 10/20/2010
[18] Bullock J, Boyle J, Wang MB. Physiology. 4 ed: Lippincott Williams & Wilkins; 2001.
[19] Lung volumes. Available at http://en.wikipedia.org/wiki/File:LungVolume.jpg; Last seen online: 11/20/2010
[20] Brambilla E, Travis WD, Colby TV, Corrin B, Shimosato Y. The new World Health Organization classification of lung tumours. European Respiratory Journal l2001;18: 1059-1068.
[21] Bryant A, Cerfolio RJ. Differences in Epidemiology, Histology, and Survival Between Cigarette Smokers and Never-Smokers Who Develop Non-small Cell Lung Cancer*. Chest l2007;132: 185-192.
[22] Schöbinger M. Konzeption und Realisierung neuer Verfahren zur Diagnoseunterstützung bei thorakalen Erkrankungen. In: Faculty of Medicine. Heidelberg: University of Heidelberg; 2008.
[23] Cotes JE, Chinn DJ, Miller MR. Lung function: physiology, measurement and application in medicine: Wiley-Blackwell; 2006.
[24] Andreoli TE, al. e. Cecil essentials of medicine. 5 ed: WB Saunders; 2001.
[25] Heimann T, Meinzer H-P. Statistical shape models for 3D medical image segmentation: A review. Medical Image Analysis l2009;13: 543-563.
[26] Yao J, Summers R. Statistical Location Model for Abdominal Organ Localization. In: Medical Image Computing and Computer-Assisted Intervention – MICCAI 2009; 2009, p. 9-17.
[27] Shen T, Huang X. 3D Medical Image Segmentation by Multiple-Surface Active Volume Models. In: al. G-ZZe, editor. MICCAI: Springer Verlag Berlin Heidelberg 2009. p. 1059-1066.
[28] Kainmüller D, Lamecker H, Zachow S, Heller M, Hege H-C. Multi-object Segmentation with Coupled Deformable Models. In: Proc. Medical Image Understanding and Analysis; 2008. p. 34-38.
[29] Frangi AF, Rueckert D, Schnabel JA, Niessen WJ. Automatic construction of multiple-object three-dimensional statistical shape models: application to cardiac modeling. Medical Imaging, IEEE Transactions on l2002;21: 1151-1166.
[30] Tsai A, Wells W, Tempany C, Grimson E, Willsky A. Coupled Multi-shape Model and Mutual Information for Medical Image Seg-

mentation. In: Information Processing in Medical Imaging; 2003, p. 185-197.
[31] Tsai A, Wells W, Tempany C, Grimson E, Willsky A. Mutual information in coupled multi-shape model for medical image segmentation. Medical Image Analysis l2004;8: 429-445.
[32] Babalola KO, Petrovic V, Cootes TF, Taylor CJ, Twining CJ, Mills A. Automatic Segmentation of the Caudate Nuclei using Active Appearance Models. In; 2010.
[33] Okada T, Yokota K, Hori M, Nakamoto M, Nakamura H, Sato Y. Construction of Hierarchical Multi-Organ Statistical Atlases and Their Application to Multi-Organ Segmentation from CT Images. In: Medical Image Computing and Computer-Assisted Intervention – MICCAI 2008; 2008, p. 502-509.
[34] Lu C, Pizer S, Joshi S, Jeong J-Y. Statistical Multi-Object Shape Models. International Journal of Computer Vision l2007;75: 387-404.
[35] Cates J, Fletcher P, Styner M, Hazlett H, Whitaker R. Particle-Based Shape Analysis of Multi-object Complexes. In: Medical Image Computing and Computer-Assisted Intervention – MICCAI 2008; 2008, p. 477-485.
[36] Relan J, Säring D, Groth M, Müllerleile K, Handels H. 3D Segmentation of the Left Ventricle combining Long- and Shortaxis Views. In: Bildverarbeitung für die Medizin; 2008.
[37] Säring D, Barmeyer A, Stork A, Handels H. Segmentierung des linken Ventrikels in 4D-MR-Bildfolgen unter Verwendung nichtlinearer Registrierung. In: 41. Jahrestagung der Deutschen Gesellschaft für Biomedizinische Technik; 2007.
[38] Thirion JP. Fast non-rigid matching of 3D medical images. In: INRIA; 1995.
[39] Säring D, Ehrhardt J, Stork A, Bansmann PM, Lund G, Handels H. Computer-Assisted Analysis of 4D Cardiac MR Image Sequences after Myocardial Infarction. Methods of Information in Medicine l2006.
[40] Corsi C, Lamberti C, Catalano O, MacEneaney P, Bardo D, Lang RM, Caiani EG, Mor-Avi V. Improved quantification of left ventricular volumes and mass based on endocardial and epicardial surface detection from cardiac MR images using level set models. J Cardiovasc Magn Reson l2005;7: 595--602.
[41] Spreeuwers L, Breeuwer M. Detection of Left Ventricular Epi- and Endocardial Borders using Coupled Active Contours. In: Proceedings CARS. London, United Kingdom; 2003.
[42] Fritz D, Rinck D, Dillmann R, Scheuering M. Segmentation of the left and right cardiac ventricle using a combined bi-temporal statistical model. In; 2006.
[43] Lorenz C, Berg Jv. A comprehensive shape model of the heart. Medical Image Analysis l2006;10: 657-670.

[44] Andreopoulos A, Tsotsos JK. Efficient and generalizable statistical models of shape and appearance for analysis of cardiac MRI. Medical Image Analysis l2008;12: 335-357.
[45] van Assen HC, Danilouchkine MG, Frangi AF, Ordás S, Westenberga JJM, Johan H.C. Reibera, Corresponding Author Contact Information, E-mail The Corresponding Author and Boudewijn P.F. Lelieveldt. SPASM: a 3D-ASM for Segmentation of Sparse and Arbitrarily Oriented Cardiac MRI Data. Medical Image Analysis l2006;10: 286-303.
[46] Rabe KF, Hurd S, Anzueto A, Barnes PJ, Buist SA, Calverley P, Fukuchi Y, Jenkins C, Rodriguez-Roisin R, van Weel C, Zielinski J. Global strategy for the diagnosis, management, and prevention of chronic obstructive pulmonary disease: GOLD executive summary. Am J Respir Crit Care Med l2007;176: 532-55.
[47] Global Strategy for Asthma Management and Prevention: Revised 2007. Available at http://www.ginasthma.org; Last seen online:
[48] Ouwens JP, van der Bij W, van der Mark TW, Geertsma A, Piers DA, de Boer WJ, Koeter GH. The value of ventilation scintigraphy after single lung transplantation. J Heart Lung Transplant l2004;23: 115-21.
[49] Al-Githmi I, Batawil N, Shigemura N, Hsin M, Lee TW, He GW, Yim A. Bronchiolitis obliterans following lung transplantation. Eur J Cardiothorac Surg l2006;30: 846-51.
[50] Eichinger M, Tetzlaff R, Puderbach M, Woodhouse N, Kauczor HU. Proton magnetic resonance imaging for assessment of lung function and respiratory dynamics. European journal of radiology l2007;64: 329-334.
[51] Gamsu G, Shames DM, McMahon J, Greenspan RH. Radiographically determined lung volumes at full inspiration and during dynamic forced expiration in normal subjects. Invest Radiol l1975;10: 100-8.
[52] Cohen E, Mier A, Heywood P, Murphy K, Boultbee J, Guz A. Diaphragmatic movement in hemiplegic patients measured by ultrasonography. Thorax l1994;49: 890-5.
[53] Houston JG, Fleet M, Cowan MD, McMillan NC. Comparison of ultrasound with fluoroscopy in the assessment of suspected hemidiaphragmatic movement abnormality. Clin Radiol l1995;50: 95-8.
[54] Qanadli SD, Orvoen-Frija E, Lacombe P, Paola RD, Bittoun J, Frija G. Estimation of Gas and Tissue Volumes by MRI: Functional Approach of Lung Imaging. Journal of Computer Assisted Tomography l1999;23: 743-748.
[55] Swift AJ, Woodhouse N, Fichele S, Siedel J, Mills GH, Beek EJRv, Wild JM. Rapid Lung Volumetry Using Ultrafast Dynamic Magnetic Resonance Imaging During Forced Vital Capacity Maneuver - Correlation With Spirometry. Invest Radiol l2007;42: 37-41.

[56] Keall PJ, Mageras GS, Balter JM, Emery RS, Forster KM, Jiang SB, Kapatoes JM, Low DA, Murphy MJ, Murray BR, Ramsey CR, Van Herk MB, Vedam SS, Wong JW, Yorke E. The management of respiratory motion in radiation oncology report of AAPM Task Group 76. Medical Physics l2006;33: 3874-3900.
[57] Mori S, Endo M, Nishizawa K, Murase K, Fujiwara H, Tanada S. Comparison of patient doses in 256-slice CT and 16-slice CT scanners. Br J Radiol l2006;79: 56-61.
[58] Plathow C, Schoebinger M, Fink C, Ley S, Puderbach M, Eichinger M, Bock M, Meinzer HP, Kauczor HU. Evaluation of lung volumetry using dynamic three-dimensional magnetic resonance imaging. Invest Radiol l2005;40: 173-9.
[59] Plathow C, Ley S, Fink C, Puderbach M, Heilmann M, Zuna I, Kauczor HU. Evaluation of chest motion and volumetry during the breathing cycle by dynamic MRI in healthy subjects: comparison with pulmonary function tests. Invest Radiol l2004;39: 202-9.
[60] Fink C LSRFEMZJBRPMPC, Kauczor HU. Effect on inspiratory and expiratory breathold on pulmonary perfusion. l2005;40: 72.
[61] Tetzlaff R, Eichinger M, Schobinger M, Puderbach M, Meinzer HP, Kauczor HU. Semiautomatic assessment of respiratory motion in dynamic MRI--comparison with simultaneously acquired spirometry. Rofo l2008;180: 961-7.
[62] Chen Q, Mai VM, Bankier AA, Napadow VJ, Gilbert RJ, Edelman RR. Ultrafast MR grid-tagging sequence for assessment of local mechanical properties of the lungs. Magnetic Resonance in Medicine l2001;45: 24-28.
[63] Napadow VJ, Mai V, Bankier A, Gilbert RJ, Edelman R, Chen Q. Determination of regional pulmonary parenchymal strain during normal respiration using spin inversion tagged magnetization MRI. Journal of Magnetic Resonance Imaging l2001;13: 467-474.
[64] Jing C, Ke S, Stanley HB, Paul WR, James ML, John PM, Eduard EdL, Gordon DC, Miller GW. Dynamic MRI of Grid-Tagged Hyperpolarized Helium-3 for the Assessment of Lung Motion During Breathing. International journal of radiation oncology, biology, physics l2009;75: 276-284.
[65] Tustison NJ, Awate SP, Cai J, Altes TA, Miller GW, de Lange EE, Mugler JP, Gee JC. Pulmonary kinematics from tagged hyperpolarized helium-3 MRI. Journal of Magnetic Resonance Imaging l2010;31: 1236-1241.
[66] Gee J, Sundaram T, Hasegawa I, Uematsu H, Hatabu H. Characterization of Regional Pulmonary Mechanics from Serial MRI Data. In: Medical Image Computing and Computer-Assisted Intervention — MICCAI 2002: Springer Berlin / Heidelberg; 2002, p. 762-769.
[67] Gee J, Sundaram T, Hasegawa I, Uematsu H, Hatabu H. Characterization of regional pulmonary mechanics from serial magnetic resonance imaging data1. Academic radiology l2003;10: 1147-1152.

[68] Sundaram TA, Avants BB, Gee JC. Towards a Dynamic Model of Pulmonary Parenchymal Deformation: Evaluation of Methods for Temporal Reparameterization of Lung Data. In: Medical Image Computing and Computer-Assisted Intervention – MICCAI 2005: Springer Berlin / Heidelberg; 2005, p. 328-335.
[69] Zapke M, Topf H-G, Zenker M, Kuth R, Deimling M, Kreisler P, Rauh M, Chefd'hotel C, Geiger B, Rupprecht T. Magnetic resonance lung function - a breakthrough for lung imaging and functional assessment? A phantom study and clinical trial. Respiratory Research l2006;7: 106.
[70] Böttger T, et al. Implementation and evaluation of a new workflow for registration and segmentation of pulmonary MRI data for regional lung perfusion assessment. Physics in Medicine and Biology l2007;52: 1261.
[71] Böttger T, Kunert T, Meinzer HP, Wolf I. Application of a New Segmentation Tool Based on Interactive Simplex Meshes to Cardiac Images and Pulmonary MRI Data. Academic radiology l2007;14: 319-329.
[72] Zaporozhan J, Ley S, Gast KK, Schmiedeskamp J, Biedermann A, Eberle B, Kauczor H-U. Functional Analysis in Single-Lung Transplant Recipients. Chest l2004;125: 173-181.
[73] Gierada DS, Hakimian S, Slone RM, Yusen RD. MR analysis of lung volume and thoracic dimensions in patients with emphysema before and after lung volume reduction surgery. Am. J. Roentgenol. l1998;170: 707-714.
[74] Chu W, Ng B, Li A, Lam T-p, Lam W, Cheng J. Dynamic magnetic resonance imaging in assessing lung function in adolescent idiopathic scoliosis: a pilot study of comparison before and after posterior spinal fusion. Journal of Orthopaedic Surgery and Research l2007;2: 20.
[75] Tokuda J, Schmitt M, Sun Y, Patz S, Tang Y, Mountford CE, Hata N, Wald LL, Hatabu H. Lung Motion and Volume Measurement by Dynamic 3D MRI Using a 128-Channel Receiver Coil. Academic radiology l2009;16: 22-27.
[76] Ray N ASTATdLEE, Brookeman JR. Merging parametric active contours within homogeneous image regions for MRI-based lung segmentation. l2003;22: 189.
[77] Osareh A, Shadgar B. Automatic Segmentation of Lung Areas in Magnetic Resonance Images. World Academy of Science, Engineering and Technology l2009;56.
[78] Olabarriaga SD, Smeulders AWM. Interaction in the segmentation of medical images: A survey. Medical Image Analysis l2001;5: 127-142.
[79] Foo JL. A survey of user interaction and automation in medical image segmentation methods. In: Human Computer Interaction Technical Report: Iowa State University; 2006.

[80] van Ginneken B, de Bruijne M, Loog M, Viergever MA. Interactive Shape Models. In: Sonka M, Fitzpatrick JM, editors. SPIE Medical Imaging; 2003. p. 1206-1216.
[81] Timinger H, Pekar V, von Berg J, Dietmayer K, Kaus M. Integration of Interactive Corrections to Model-Based Segmentation Algorithms. In: Bildverarbeitung für die Medizin 2003; 2003. p. 171-175.
[82] Heimann T. Statistical Shape Models for 3D Medical Image Segmentation. Saarbruecken: Vdm Verlag Dr. Müller; 2009.
[83] Cootes TF, Taylor CJ, Cooper DH, Graham J. Active shape models; their training and application. Comput Vis Image Underst l1995;61: 38-59.
[84] Lorensen WE, Cline HE. Marching cubes: A high resolution 3D surface construction algorithm. SIGGRAPH Comput. Graph. l1987;21: 163-169.
[85] Cootes TF, Taylor CJ. Statistical Models of Appearance for Computer Vision. In; 2004.
[86] Dryden IL, Mardia KV. Statistical Shape Analysis: John Wiley & Sons; 1998.
[87] Cootes TF, Taylor CJ. Statistical Models of Appearance for Medical Image Analysis and Computer Vision. In: SPIE Medical Imaging; 2001.
[88] Gower J. Generalized procrustes analysis. Psychometrika l1975;40: 33-51.
[89] Goodall C. Procrustes methods in the statistical analysis of shape. J. Roy. Stat. Soc. B l1991;53: 285-339.
[90] Heimann T, Wolf I, Williams T, Meinzer H-P. 3D Active Shape Models Using Gradient Descent Optimization of Description Length. In: Christensen GE, Sonka M, editors. Information Processing in Medical Imaging: Springer Berlin / Heidelberg; 2005, p. 566-577.
[91] Jolliff IT. Principle Component Analysis: Springer; 2002.
[92] Kalman D. A Singularly Valuable Decomposition: The SVD of a Matrix. The College Mathematics Journal l1996;27: 2-23.
[93] de Bruijne M, van Ginneken B, Viergever MA, Niessen WJ. Adapting Active Shape Models for 3D segmentation of tubular structures in medical images. Inf Process Med Imaging l2003;18: 136-47.
[94] Kittler J, Alkoot FM. Moderating k-NN Classifiers. Pattern Analysis & Applications l2002;5: 326-332.
[95] Bacher M, Pekar V, Kaus M. Model-Based Segmentation of Anatomical Structures in MR Images of the Head and Neck Area. In: Meinzer H-P, Handels H, Horsch A, Tolxdorff T, editors. Bildverarbeitung für die Medizin 2005: Springer Berlin Heidelberg; 2005, p. 113-117.
[96] Heimann T, Münzing S, Meinzer H-P, Wolf I. A Shape-Guided Deformable Model with Evolutionary Algorithm Initialization for 3D

Soft Tissue Segmentation. In: Information Processing in Medical Imaging: Springer Berlin/Heidelberg; 2007, p. 1-12.
[97] Lekadir K, Yang GZ. Optimal feature point selection and automatic initialization in active shape model search. Med Image Comput Comput Assist Interv l2008;11: 434-41.
[98] Cosío FA. Automatic initialization of an active shape model of the prostate. Medical Image Analysis l2008;12: 469-483.
[99] Li B, Acton ST. Automatic active model initialization via Poisson inverse gradient. IEEE Trans Image Process l2008;17: 1406-20.
[100] Wolf I, Vetter M, Wegner I, Böttger T, Nolden M, Schöbinger M, Hastenteufel M, Kunert T, Meinzer HP. The medical imaging interaction toolkit. Med Image Analysis l2005;9: 594--604.
[101] Engelmann U, Schröter A, Evers H, Gundel S, Schwab M, Meinzer H-P. CHILI: Eine Integrationsplattform für Bildverarbeitungsmethoden. In; 1999.
[102] Schulte B, Bolt A, Beyer D. MRT des Herzens und der Gefasse: Springer Berlin Heidelberg; 2005.
[103] Davis MH, Khotanzad A, Flamig DP, Harms SE. Elastic Body Splines: A Physics Based Approach to Coordinate Transformation in Medical Image Matching. In: IEEE Symposium on Computer-Based Medical Systems. Los Alamitos, CA, USA: IEEE Computer Society; 1995. p. 81-88.
[104] Greig DM, Porteous BT, Seheult AH. Exact Maximum A Posteriori Estimation for Binary Images.
[105] Linkenheil M. Graph-Cut-Segmentierung für die medizinische Bildverarbeitung. In. Heidelberg: Heidelberg; 2005.
[106] Warfield SK, Zou KH, Wells WM. Validation of image segmentation and expert quality with an expectation-maximization algorithm. In: MICCAI: Springer; 2002. p. 298-306.
[107] Heidenreich PA, Steffens J, Fujita N, al. e. Evaluation of mitral stenosis with velocity-encoded cine-magnetic resonance imaging. Am J Cardiol l1995;75: 365-9.
[108] Lötjönen J, Kivistö S, Koikkalainen J, Smutek D, Lauerma K. Statistical shape model of atria, ventricles and epicardium from short- and long-axis MR images. Medical Image Analysis l2004;8: 371-386.
[109] Kaus MR, Berg Jv, Weese J, Niessen W, Pekar V. Automated segmentation of the left ventricle in cardiac MRI. Medical Image Analysis l2004;8: 245-254.
[110] van Assen HC, Danilouchkine MG, Frangi AF, Ordás S, Westenberg JJM, Reiber JHC, Lelieveldt BPF. SPASM: A 3D-ASM for segmentation of sparse and arbitrarily oriented cardiac MRI data. Medical Image Analysis l2006;10: 286-303.
[111] Eichinger M, Puderbach M, Smith HJ, Tetzlaff R, Kopp-Schneider A, Bock M, Biederer J, Kauczor HU. Magnetic resonance-

compatible-spirometry: principle, technical evaluation and application. Eur Respir J l2007;30: 972-9.
[112] Markstaller K, Kauczor HU, Puderbach M, Mayer E, Viallon M, Gast K, Weiler N, Thelen M, Eberle B. 3He-MRI-based vs. conventional determination of lung volumes in patients after unilateral lung transplantation: a new approach to regional spirometry. Acta Anaesthesiologica Scandinavica l2002;46: 845-852.
[113] Kondo T, Kobayashi I, Taguchi Y, Hayama N, Tajiri S, Yanagimachi N. An analysis of the chest wall motions using the dynamic MRI in healthy elder subjects. Tokai J Exp Clin Med l2005;30: 15-20.
[114] Kondo T, Kobayashi I, Taguchi Y, Ohta Y, Yanagimachi N. A dynamic analysis of chest wall motions with MRI in healthy young subjects. Respirology l2000;5: 19-25.
[115] Ley S, Kreitner K-F, Fink C, Heussel CP, Borst MM, Kauczor H-U. Assessment of pulmonary hypertension by CT and MR imaging. European Radiology l2004;14: 359-368.
[116] Plathow C, Fink C, Sandner A, Ley S, Puderbach M, Eichinger M, Schmahl A, Kauczor HU. Comparison of relative forced expiratory volume of one second with dynamic magnetic resonance imaging parameters in healthy subjects and patients with lung cancer. J Magn Reson Imaging l2005;21: 212-8.
[117] Kiryu S, Loring SH, Mori Y, Rofsky NM, Hatabu H, Takahashi M. Quantitative analysis of the velocity and synchronicity of diaphragmantic motion: dynamic MRI in different postures. Magnetic Resonance Imaging l2006;24.

Acknowledgements

I would like to thank the following people for their help and support in all kinds of aspects during this thesis:

Prof Dr. Bernd Jähne and Prof. Dr. Hans-Peter Meinzer, for the supervision and appraisal of this thesis at the physics faculty of University of Heidelberg.

Dr. Tobias Heimann, for the mentoring and fast proof reading of this thesis, and his many good ideas regarding the work done in this thesis.

My colleagues and friends at the group of Medical and Biological Informatics (MBI) at German Cancer Research Center, for the great time I had during my thesis.

Dr. Ralf Tetzlaff, for the close cooperation and the many good ideas regarding the work done in this thesis.

My medical partners Dr. Eichinger, Dr. Loßnitzer, Dr. Mohrhardt and Dr. Steen, for the friendly cooperation.

Dr. Karl Wunderle, for the last-minute proof reading.

Again, my boss and head of department MBI Pitt Meinzer, for the opportunity to carry out this thesis, and the friendly atmosphere in the group.

Last, but not least, my parents, for supporting me all the time: Thank you!

Who finds spelling mistakes is allowed to keep them.

Erklärungen gemäß § 8 (3) b) und c) der Promotionsordnung:

a) Ich erkläre hiermit, dass ich die vorgelegte Dissertation selbst verfasst und mich keiner anderen als der von mir ausdrücklich bezeichneten Quellen und Hilfen bedient habe.

b) Ich erkläre hiermit, dass ich an keiner anderen Stelle ein Prüfungsverfahren beantragt bzw. die Dissertation in dieser oder anderer Form bereits anderweitig als Prüfungsarbeit verwendet oder einer anderen Fakultät als Dissertation vorgelegt habe.

Heidelberg, den 06.12.2010 .....